

Numerical Study of Head-on Binary Droplet Collisions: Towards Predicting the Collision Outcomes


Vom Fachbereich Maschinenbau an der Technischen Universität Darmstadt
zur Erlangung des akademischen Grades Doktor-Ingenieur (Dr.-Ing.)
genehmigte Dissertation von Muyuan Liu M.Sc. aus Hebei, China
Tag der Einreichung: 31.05.2017, Tag der Prüfung: 17.10.2017
Darmstadt 2017 — D 17

1. Gutachten: Prof. Dr. rer. nat. Dieter Bothe
2. Gutachten: Prof. Dr.-Ing. Cameron Tropea



TECHNISCHE
UNIVERSITÄT
DARMSTADT



 Mathematical
Modeling and Analysis

Numerical Study of Head-on Binary Droplet Collisions: Towards Predicting the Collision Outcomes

Genehmigte Dissertation von Muyuan Liu M.Sc. aus Hebei, China

1. Gutachten: Prof. Dr. rer. nat. Dieter Bothe
2. Gutachten: Prof. Dr.-Ing. Cameron Tropea

Tag der Einreichung: 31.05.2017

Tag der Prüfung: 17.10.2017

Darmstadt – D 17

Bitte zitieren Sie dieses Dokument als:

URN: urn:nbn:de:tuda-tuprints-70187

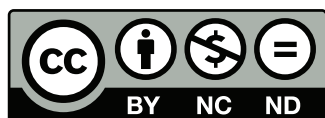
<http://tuprints.ulb.tu-darmstadt.de/id/user/7018>

Dieses Dokument wird bereitgestellt von tuprints,

E-Publishing-Service der TU Darmstadt

<http://tuprints.ulb.tu-darmstadt.de>

tuprints@ulb.tu-darmstadt.de



Die Veröffentlichung steht unter folgender Creative Commons Lizenz:

Namensnennung – Keine kommerzielle Nutzung – Keine Bearbeitung 4.0 International

<http://creativecommons.org/licenses/by-nc-nd/4.0/>

Acknowledgment

First of all, I would like to express my sincere gratitude to my supervisor, Prof. Dr. Dieter Bothe, for introducing me to the world of science, for providing me with useful guidance throughout my research and for the encouragement while I was hesitating. His kindness and friendly way of mentoring have made life during my doctoral research more meaningful than research alone would have. All the things I have learned from him, which are much more than I could have ever expected at the start, are incredible assets.

I am grateful to Prof. Dr. Cameron Tropea for being my second supervisor and for correcting my dissertation. His extensive teachings on fluid dynamics are the foundation of my research.

I owe all the former and present colleagues at Mathematical Modeling and Analysis my gratitude for their kind help which eased my boarding. We shared interesting and inspiring discussions, many of which turned out to be important for the success of my research. I appreciate the computational hours provided by the Hochschulrechenzentrum of the Darmstadt University of Technology and the financial support provided by the German Research Foundation.

Finally, I want to thank my friends for their support and my parents for their love.

Darmstadt, May 2017

Muyuan Liu

Publications during the doctoral research

M. Liu, D. Bothe: *Numerical study of head-on droplet collisions at high Weber numbers*. Journal of Fluid Mechanics, 289: 785-805, 2016.

C. Planchette, H. Hinterbichler, M. Liu, D. Bothe and G. Brenn: *Colliding drops as coalescing and fragmenting liquid springs*. Journal of Fluid Mechanics, 814: 277-300, 2017.

L. Reitter, M. Liu, J. Breitenbach, K. L. Huang, D. Bothe, G. Brenn, K. L. Pan, I. V. Roisman and C. Tropea: *Experimental and computational investigation of binary drop collisions under elevated pressure*. In 28th Annual Conference on Liquid Atomization and Spray Systems, Valencia, Spain, 2017.

M. Liu, D. Bothe: *Numerical study of binary droplet collisions at high Weber numbers*. Presentation in ProcessNet Annual Conference, Bingen, Germany, 2016.

M. Liu, D. Bothe: *Numerical study of head-on collisions of water droplets at high Weber numbers*. Poster for International Conference on Multiphase Flows, Florence, Italy, 2016.

Kurzfassung

Binäre Tropfenkollisionen spielen eine wichtige Rolle in der Natur und in vielen technischen Sprayanwendungen. Die Modellierung der Kollisionsausgänge, nämlich Bouncing, Coalescence, Tropfenzerfall nach vorläufiger Verschmelzung und Spatter (auch „Shattering“ und „Splashing“ genannt), bildet die Grundlage für die Untersuchung der Zerstäubungsprozesse auf größeren Skalen. Das Ziel dieser Arbeit richtet sich auf die Entwicklung von numerischen Methoden, welche für die Prädiktion der Kollisionsausgänge eingesetzt werden, sowie die numerische Untersuchung derjenigen Phänomene in binären Tropfenkollisionen, welche die Kollisionsausgänge entscheidend beeinflussen. Für die numerischen Simulationen wird der Inhouse-Code Free Surface 3D (FS3D), der auf der Volume-of-Fluid (VOF) Methode basiert, eingesetzt. Die numerischen Untersuchungen beschränken sich auf zentrale Kollisionen.

Spatter tritt bei Tropfenkollisionen mit hoher Kollisionsenergie auf, wobei eine dünne Pralllamelle entsteht und in standardmäßigen Simulationen unphysikalisch zerfällt. Um Spatter simulieren zu können, wird ein verbesserter Lamellenstabilisierungsalgorithmus entwickelt und ausführlich validiert. Mit einem geeignet eingebrachten Verrauschen des Anfangsgeschwindigkeitsfeldes wird die Instabilität am Rand des Stoßkomplexes ausgelöst und Spatter in der Simulation erfolgreich reproduziert. Die Simulationsergebnisse stimmen sehr gut mit den Experimenten überein. Basierend auf den Simulationsergebnissen wird die Entwicklung der Randinstabilität als eine Verstärkung eines Signals durch ein Signalverstärkungssystem, das in drei seriell verbundene Subsysteme unterteilt wird, betrachtet. Dabei wird festgestellt, dass die Entwicklung der Randinstabilität in der linearen Phase der Randinstabilität durch die Rayleigh-Plateau Instabilitätstheorie vorhergesagt werden kann. Der Einfluss der Tropfenviskosität wird numerisch untersucht und es wird gezeigt, dass der Kollisionsausgang zu Spatter neigt, wenn die Tropfenviskosität verkleinert wird. Diese Abhängigkeit nimmt während der Abnahme der Tropfenviskosität ab. Die Tropfenviskosität beeinflusst die Entwicklung der Randinstabilität vor allem, indem die Basisgeometrie des Randes verändert wird. Eine erfolgreiche Aufklärung des Mechanismus der Randinstabilität bildet den Grundstein für die Vorhersage des Eintritts von Spatter und die Vorhersage des Größenspektrums der sekundären Tropfen, die bei Spatter entstehen. Die Untersuchung des Mechanismus der Randinstabilität im Kontext von binärer Tropfenkollisionen hat eine generelle Bedeutung, weil der Ausstoß von Sekundärtropfen von einem instabilen Rand beim Aufprall eines Tropfens auf eine feste Wand oder auf einen Flüssigkeitsfilm ebenfalls auftritt.

Binäre Tropfenkollisionen führen bei relativ kleinen Weberzahlen entweder zu Bouncing oder zu Coalescence als Kollisionsausgang. Die Simulationen von Bouncing und Coalescence werden durch die Umschaltung der Randbedingungen an der Aufprallwand erfolgreich durchgeführt. Die Simulationsergebnisse stimmen mit den Experimenten gut überein. Allerdings sind diese Simulationen nicht prädiktiv, weil der Kollisionsausgang vorgegeben werden muss. Die

Schwierigkeit der Prädiktion des Kollisionsausgangs Bouncing vs. Coalescence liegt darin, dass der dünne Gasfilm zwischen den kollidierenden Tropfen nicht aufgelöst werden kann und ein physikalisch sinnvolles Koaleszenzkriterium in der numerischen Methode fehlt. Um die prädiktive Simulation zu ermöglichen, wird ein Multiskalen-Simulationskonzept erarbeitet. Neben dem Hauptlöser FS3D, der die Strömung auf der makroskopischen Skala löst, besteht das Multiskalen-Simulationskonzept aus drei Anteilen: (1) Ein Subgridskalen(SGS)-Modell wird integriert in den Hauptlöser FS3D. (2) Coalescence wird numerisch unterdrückt, bevor ein geeignetes Koaleszenzkriterium möglicherweise erfüllt ist. (3) Ein numerisches Koaleszenzkriterium wird angewandt.

Basierend auf der Lubrikationstheorie wird das SGS-Modell hergeleitet, wobei der Effekt verdünnter Strömung mit berücksichtigt wird. Das SGS-Modell wird in FS3D implementiert und ausführlich validiert. Zur Kopplung des SGS-Modells wird der Druck im Gasfilm, der durch das SGS-Modell gelöst wird, als Druckrandbedingung auf der Aufprallebene aufgeprägt. Wird die erste Schneidung der PLIC-Flächen mit der Kollisionsebene als Koaleszenzkriterium angewendet, können die Simulationsergebnisse sowohl Bouncing als auch Coalescence sein. Allerdings ist der Kollisionsausgang abhängig von der Gitterauflösung. Wird als Koaleszenzkriterium eine Gasfilmdicke von null im Rahmen der im Algorithmus verwendeten Toleranzen angewendet, führen die Simulationen ausschließlich zu Bouncing. Es wird gezeigt, dass auch weitere mögliche Korrekturen der Geschwindigkeiten, die für den Transport der Flüssigkeitsphase eingesetzt werden, nicht ausreichen, den Übergang zwischen Bouncing und Coalescence vorherzusagen. Als Ausblick wird angedeutet, wie in zukünftigen Forschungsarbeiten z.B. mit Hilfe der volumengemittelten Volume-of-Fluid (VA-VOF) Methode, die den Geschwindigkeitsunterschied innerhalb einer Rechenzelle berücksichtigt, die Genauigkeit des Transports der Flüssigkeitsphase erhöht werden kann.

Mit Hilfe der Multiskalen-Simulation wird qualitativ gezeigt, dass der Kollisionsausgang bei hoher Verdünnung in der Gasphase zu Coalescence neigt.

Abstract

Binary droplet collision plays an important role in nature and in many technical processes involving sprays. The modeling of the collision outcomes, namely bouncing, coalescence, separation after temporary coalescence, and spatter (also called ‘shattering’ and ‘splashing’), establishes the basis for the investigation of the atomization processes on larger length scales. The aim of this thesis is to develop numerical methods that are employed in the prediction of the collision outcomes and the numerical investigation of the phenomena in binary droplet collisions which affect the collision outcomes. The in-house code Free Surface 3D (FS3D), which is based on the Volume of Fluid (VOF) method, is employed for the numerical simulations. The numerical investigations are restricted to head-on collisions.

Spatter occurs at high energetic collisions, resulting in a thin liquid lamella that ruptures artificially in standard numerical simulations. In order to simulate spatter, an improved lamella stabilization algorithm has been developed and extensively validated. By means of properly chosen white noise disturbances of the initial velocity field, the instability of the rim of the collision complex is triggered and the spatter is successfully reproduced in the simulations. Very good agreements between the simulation results and the experiments are achieved. Based on the simulation results, the development of the rim instability is considered as an amplification of disturbances via a signal amplification system that is subdivided into three sequential connected subsystems. It is confirmed that the development of the rim instability in the linear phase of the instability can be predicted by the Rayleigh-Plateau instability theory. The influence of the droplet viscosity is studied numerically and it is shown that the collision outcome tends to be spatter when the droplet viscosity is reduced. This dependency decreases with the decrease of the droplet viscosity. The droplet viscosity influences the development of the rim instability mainly through varying the geometrical evolution of the rim. A successful elucidation of the mechanism of rim instability builds the foundation for the prediction of the occurrence of spatter and the prediction of the size distribution of the secondary droplets arising in spatter. The investigation of the mechanism of the rim instability in the context of binary droplet collisions is of general importance because the ejection of secondary droplets from an unstable rim also emerges in collisions of a droplet on a solid substrate or on a liquid film.

Binary droplet collisions result in bouncing or coalescence at relatively small Weber numbers. The simulations of bouncing and coalescence have been successfully conducted by switching the boundary conditions on the collision plane. The simulation results are in good agreement with corresponding experiments. However, the simulations are not predictive because the collision outcome must be specified in advance. The difficulty of the prediction of bouncing versus coalescence lies in the fact that the thin gas film between the colliding droplets cannot be resolved in feasible simulations and that a physically meaningful coalescence criterion is missing in the numerical method. In order to facilitate the predictive simulation, a multi-scale simulation con-

cept has been developed. In addition to the main solver FS3D, which solves the flow on the macroscopic scale, the multi-scale simulation concept consists of three parts: (1) A sub-grid-scale (SGS) model is integrated within the main solver FS3D. (2) Coalescence is numerically suppressed before a suitable coalescence criterion is contingently satisfied. (3) A numerical coalescence criterion is applied.

Based on the lubrication theory, the SGS model is derived which accounts for the rarefied flow effect. The SGS model is implemented in FS3D and extensively validated. For the integration of the SGS model, the pressure in the gas film, which is solved by the SGS model, applies as a pressure boundary condition on the collision plane. Employing the first intersection of PLIC-surfaces with the collision plane as coalescence criterion, the collision outcome in the simulation can be both bouncing and coalescence. The predicted collision outcome, however, depends on the grid resolution. Employing zero gas film thickness (in algorithm tolerance) as coalescence criterion, the simulations result only in bouncing. It is shown that various possible corrections of the velocity field, which decides the transport of the liquid phase, have not led to a meaningful prediction of the transition between coalescence and bouncing. Further developments, e.g. the volume-averaged Volume of Fluid (VA-VOF) method, which takes into account the velocity difference within a computational cell, shall be implemented in future work to increase the accuracy of the transport of the fluid phase.

By means of the multi-scale simulation it is qualitatively shown that the collision outcome tends to be coalescence at higher rarefaction in the gas phase.

Contents

1. Introduction	1
1.1. Motivation	1
1.2. Fundamentals of binary droplet collisions	2
1.2.1. Phenomenological description and literature review	5
1.3. Organization of the thesis	9
2. Mathematical Modeling of Two-Phase Fluid Systems	11
2.1. Governing equations in incompressible two-phase fluid systems	11
2.1.1. Mass conservation	12
2.1.2. Transport equation of the phase indicator	13
2.1.3. Momentum conservation	13
2.1.4. Differential equations governing the flow in two-phase fluid systems	14
2.2. Interfacial instabilities	14
2.2.1. Plateau-Rayleigh instability	14
2.2.2. Rayleigh-Taylor instability	16
2.3. Continuum mechanics and rarefied gas flow regimes	17
3. Numerical Methods	19
3.1. Finite Volume discretization	19
3.2. Volume of Fluid method	20
3.3. Modeling of the surface tension force	22
3.4. Time discretization	25
3.5. Typical setup for head-on collisions of two identical droplets	27
3.6. Computation of the energy contributions	27
4. Lamella Stabilization	31
4.1. Stabilization of a liquid lamella	31
4.1.1. Validation	33
4.1.2. Lamella stabilization in terms of the balanced-CSF model	34
4.1.3. Correction of the computation of the surface energy	35
4.2. Stabilization of a gas lamella	36
4.2.1. Dependence on the grid resolution	38
4.2.2. Correction of the computation of the surface energy with a present under-resolved gas lamella	41

5. Numerical Simulations of Spatter Phenomenon and the Mechanism of the Rim Instability	45
5.1. Domain adjustment	45
5.2. Numerical setups for water droplet collisions	46
5.2.1. Role of imposed disturbances	47
5.3. Simulation results for water droplet collisions and quantification of the rim development	48
5.3.1. Comparison with experiments	48
5.3.2. Quantification of the rim development	51
5.4. Division of the collision process	55
5.5. The rim instability	57
5.5.1. Initial unstable phase: RT instability?	58
5.5.2. Linear unstable phase: PR instability?	59
5.5.3. The nonlinear unstable phase	60
5.6. Influence of liquid viscosity	61
5.6.1. Evolution of the rim geometry depending on viscosity	61
5.6.2. Input signals and output signals in the linear unstable phase	65
5.6.3. Growing rim as a signal amplification system	66
5.6.4. Conclusion on the viscosity effect	69
6. Flow in the Gas Layer between the Colliding Droplets	71
7. Multi-Scale Simulations aiming at Predictions of the Transition between Bouncing and Coalescence	77
7.1. Derivation of the SGS model starting from the lubrication theory	77
7.1.1. Analytical solutions of two idealized cases	81
7.1.2. Rarefied lubrication equation	83
7.1.3. Calibration of the slip coefficients	86
7.2. Implementation of the SGS model	87
7.2.1. Approximation of the quantities related to the interface	87
7.2.2. Equation system	88
7.3. Validation of the SGS model	89
7.3.1. Validation through the scenario of two approaching solid spheres	89
7.3.2. Validation through a virtual scenario based on a retracing ellipsoid	90
7.4. Integration of the SGS model into the main solver FS3D	93
7.5. Prediction of the collision outcome in terms of coalescence versus bouncing	94
7.5.1. Preliminary results of predictions	95
7.5.2. Modified f -transport	96
7.6. Rarefaction effect	98
7.7. Role of the compressibility	100

8. Summary and Outlook	101
8.1. Summary	101
8.2. Outlook	103
A. Simulations of Spatter Conducted at ITLR of the University of Stuttgart	105
B. Lubrication Equation in Cylindrical Coordinates	107
B.1. Transformation between Cartesian coordinates and polar coordinates	107
B.2. Lubrication equation in cylindrical coordinates	107
B.3. Pressure in the gas layer between two approaching parallel plates in cylindrical form	108
C. Setups	109
Bibliography	113



Nomenclature

Latin symbols		Unit
\mathbf{n}	normal vector	m
\mathbf{u}	velocity	m/s
\mathbf{T}	stress tensor	kg/(ms ²)
\mathbf{g}	gravitation	m/(s ²)
t	time	s
x, y, z	Cartesian coordinates	m
f	volume fraction	-
r	radius /radius coordinate	m
R	radius	-
p	pressure	Pa
A	area	m ²
V	volume	m ³
L, l, b, h	length	m
B	offset of a collision	m
E	energy	J
m	mass	kg
X	impact parameter	-
C	Courant number	-
m	instability mode	-
a	amplitude	-
k	wave number	-
Greek symbols		Unit
λ	mean free path	m
ρ	density	kg/m ³
κ	curvature	m ⁻¹
η	dynamic viscosity	Pa·s
σ	surface tension	N/m
Γ	interface	-

Δ	difference	-
Φ	extensive quantity	-
ϕ	density of an extensive quantity	-
Ω	domain	-
δ	Dirac operator	-
φ	density ratio	-
ψ	viscosity ratio	-
χ	phase indicator	-
ω	growth rate	-

Indexes

0	initial value
a	value on interface
l	liquid phase
g	gas phase
\pm	phase
b	ambient

Abbreviations

Re	Reynolds number
We	Weber number
Oh	Ohnesorge number
Kn	Knudsen number
DNS	Direct Numerical Simulation
FV	Finite Volume
CV	Control Volume
CFL	Courant-Friedrichs-Lewy
VOF	Volume of Fluid
FS3D	Free Surface 3D
SGS	Sub-Grid-Scale
VdW	Van der Waals force
DFG	German research foundation
TRR	Transregio
ITLR	Institut für Thermodynamik der Luft- und Raumfahrt
MMA	Mathematical Modeling and Analysis

1 Introduction

1.1 Motivation

Droplet collisions are very common phenomena observed in nature: some people even enjoy staring at the splash of droplets resulting from heavy rains hitting the ground, lost in thought. The earliest study of droplet collisions dates back to Lord Rayleigh [48] who noted that small rain droplets bounce upon collision with a pool of water rather than dive into it directly. The majority of early works on the collision of two droplets dating from the 1960's focused on water droplets essentially due to droplet growth relating to precipitation. Gunn [21] pointed out that binary collisions of water droplets result in four typical types of outcome: (I) bouncing, (II) coalescence, (III) drop disruption after coalescence, (IV) drop spatter; see Figure 1.1 for a first impression. He also noted that approximately seven collisions occur for every kilometer of free fall in typical heavy rain, which is frequent enough to influence the size of rain droplets.

In technical applications, droplet collision is an elementary process in the liquid atomization processes that convert bulk fluid into a spray composed of a dispersion of small droplets. An example of a spray is shown in Figure 1.2. Fluid atomization processes and sprays are of importance in many industrial processes, for example in fuel injection in internal combustions, spray painting, food processing, pharmaceuticals, environmental protection, and many others. The main purpose of the atomization process is to increase the contact area between the gas phase and the liquid phase. An increase in the gas-liquid contact area in a spray augments momentum, heat, and mass-transfer between the gas phase and the liquid phase as well as the related chemical processes like the combustion of fuel droplets. Apart from the primary atomization, in which the supplied liquid is demolished into a cloud of droplets, the collision of the disinte-

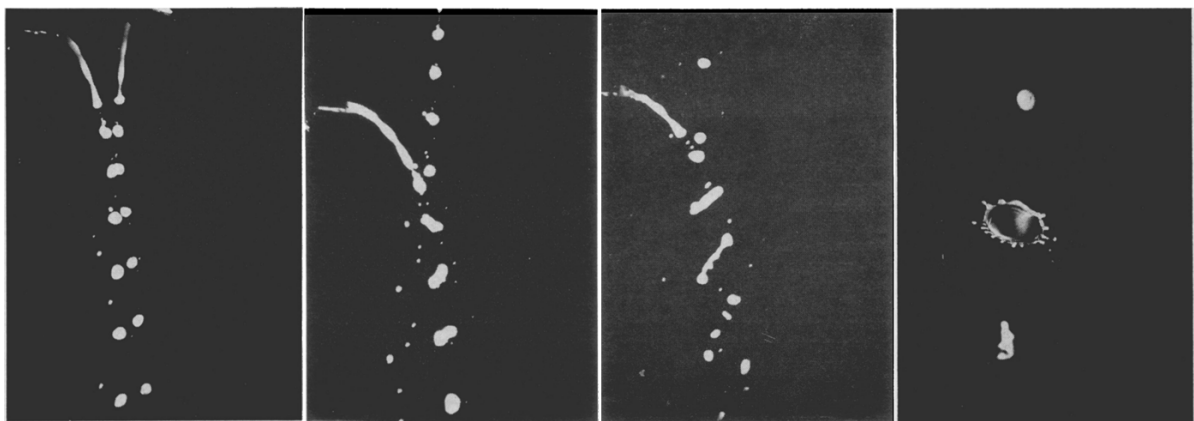


Figure 1.1.: Water droplet collisions imaged by Gunn [21]. From left to right: bouncing, coalescence, disruption after coalescence and drop spatter.



Figure 1.2.: Diesel spray imaged by Wang et al. [67]

grated droplets also affects the droplet size spectrum in a spray through the different collision outcomes.

It is difficult to investigate the whole spray process by means of Direct Numerical Simulations (DNS), which resolve all the relevant length scales and time scales of a physical problem, due to the large span of the length scale: for example in typical diesel combustion engines, the droplet size is in the region of $1 - 10 \mu\text{m}$ while the length of the injected fuel spray is $2 - 3 \text{ cm}$ [4]. Generally, computational models for simulating sprays are based on Sub-Grid-Scale (SGS) models which include the averaged effect of the unsolved scales. The large-scale behavior of the spray is then described by reduced mathematical models, rather than detailed solution of the Navier-Stokes equations [44]. An accurate prediction of the characteristics of a spray requires that the SGS model accounts for the effect of droplet collisions in terms of the collision outcomes due to the collective effect on the flow property. The derivation of models for determining the collision outcomes is usually based on experimental observations and measurements, which are restricted by the spatial and temporal resolutions of the obtained photographs recording the collision process of two droplets. In principle, Direct Numerical Simulations of the collision process can provide information that is not accessible by experimental measurements, for example the detailed local flow properties within a droplet, which facilitates the modeling of the collision rules. As long as the numerical simulation is able to reproduce the collision process, more strictly saying predictively, spectacular phenomena like the spatter of droplets can be studied by means of numerical ‘experiments’.

1.2 Fundamentals of binary droplet collisions

The collision of two droplets, say, the binary droplet collision, is a very complex phenomenon in practice. The participating droplets may have different sizes and/or different materials which are miscible or immiscible. The possible complex rheological behavior of the liquid material makes the study of the collision process even more difficult. In real systems far away from thermodynamic equilibrium like within diesel combustion chambers, the Marangoni-effect, i.e. the variation of the surface tension along the droplet surface, the evaporation and burning of the droplets would also affect the collision process significantly. Looking beyond all of these complexities, the study in this work is restricted to the collision of two Newtonian droplets of the same size and the same material under isothermal conditions without chemical reactions.

In the simplified collision system consisting of two identical droplets and environmental gas, which is schematically described in Figure 1.3, the dimensional analysis yields that the collision process is determined by the following five dimensionless parameters [38]:

- **Weber number**

$$\text{We} = \frac{\rho_l U_r^2 D_0}{\sigma} \quad (1.1)$$

- **Reynolds number**

$$\text{Re} = \frac{\rho_l U_r D_0}{\eta_l} \quad (1.2)$$

- **Density ratio**

$$\psi = \frac{\rho_l}{\rho_g} \quad (1.3)$$

- **Viscosity ratio**

$$\varphi = \frac{\eta_l}{\eta_g} \quad (1.4)$$

- **Impact parameter**

$$X = \frac{B}{D_0} \quad (1.5)$$

with the parameters in the collision system listed as follows:

ρ_l	density of the liquid phase, $\text{kg} \cdot \text{m}^3$
ρ_g	density of the gas phase, $\text{kg} \cdot \text{m}^3$
η_l	dynamic viscosity of the liquid phase, $\text{Pa} \cdot \text{s}$
η_g	dynamic viscosity of the gas phase, $\text{Pa} \cdot \text{s}$
U_0	relative velocity of the droplets, m/s
D_0	initial diameter of the droplets, m
σ	surface tension, $\text{N} \cdot \text{m}$
B	offset of the collision, m

The Weber number describes the relative importance of the droplets' inertia compared to the surface tension and the Reynolds number describes the relative importance of the droplets' inertia compared to the viscous effect. The impact parameter is a measure of the offset of a collision. A collision is called a head-on collision if the impact parameter is zero.

Depending on the system parameters, several different collision outcomes can occur. The typical collision processes are illustrated in Figure 1.4. Following the convention in previous studies [45] [16], the collision outcomes are summarized in the collision diagram, see Figure 1.5. Note that the collision diagram in Figure 1.5 is a qualitative description and will differ with

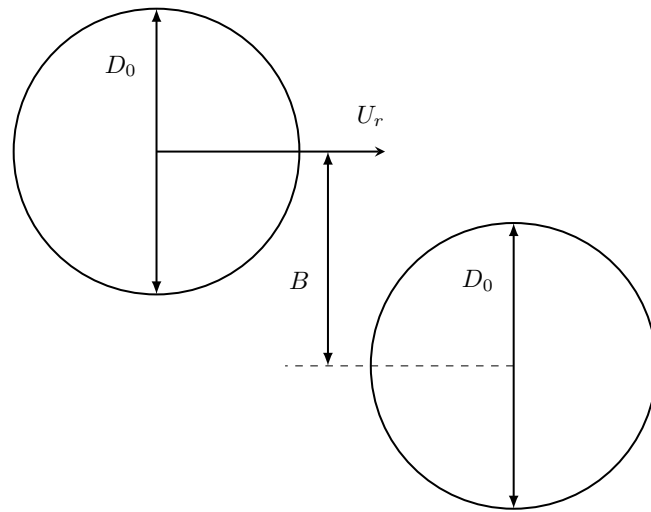


Figure 1.3.: Collision of two identical droplets.

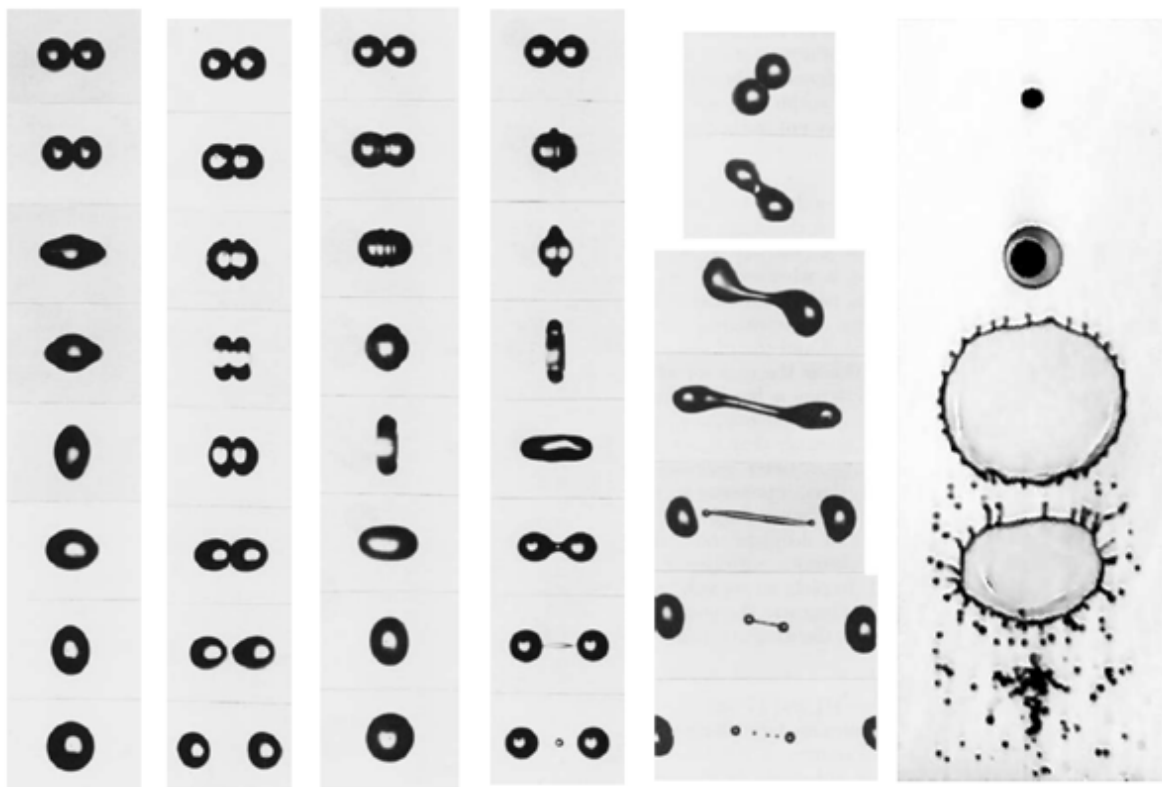


Figure 1.4.: Typical collision processes imaged by Jiang et al. [25] (first to fifth column) and by Roth et al. [56] (sixth column). From left to right: coalescence (sector I), bouncing (sector II), coalescence (sector III), near head-on separation (sector IV), off-center separation (sector V) and spatter (sector VI).

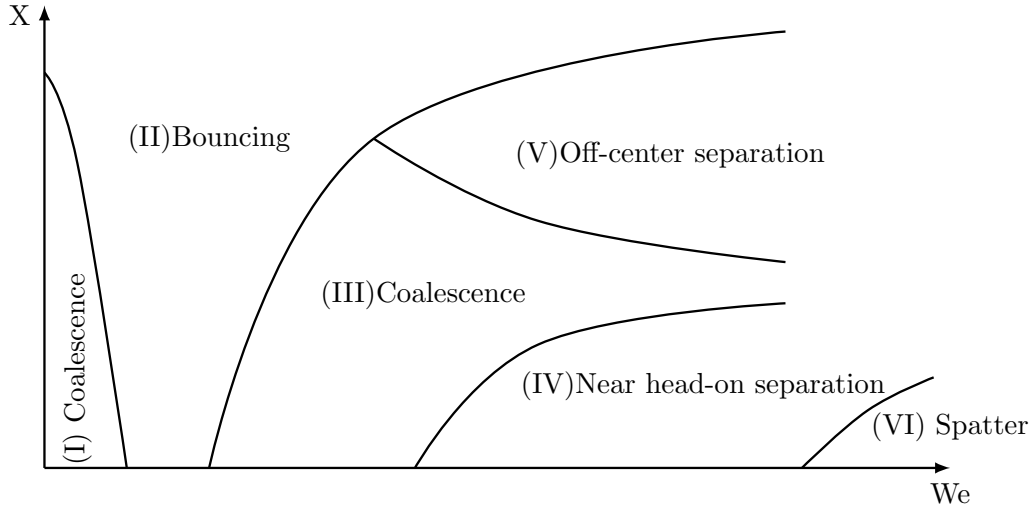


Figure 1.5.: Collision diagram.

different Re , ψ and φ , since each boundary curve between two sectors of different collision outcomes, without considering other effects, is described as

$$X = X(We, Re, \psi, \varphi). \quad (1.6)$$

The Reynolds number in equation (1.6) can be substituted by the Ohnesorge number defined as

$$Oh = \frac{\eta_l}{\sqrt{D_0 \cdot \rho_l \cdot \sigma}} = \frac{\sqrt{We}}{Re}. \quad (1.7)$$

The advantage of using the Ohnesorge number instead of Reynolds number is that the collision outcome is then only dependent on We and X , as long as the materials in the collision system and the droplet size are fixed. Another dimensionless parameter used for the description of the temporal evolution of a collision process is the dimensionless time defined as

$$t^* = t \cdot U_r / D_0. \quad (1.8)$$

The time instant when the distance between the sphere center of the droplets is D_0 , i.e. when the droplets are just touching each other, is defined as $t^* = 0$.

1.2.1 Phenomenological description and literature review

Most studies of binary droplet collisions have been driven by the prediction of the collision outcome due to its important applications in the study of systems on larger length scales. The literature review is subdivided according to the transitions between the collision outcomes, along with the description of the significant phenomena related to the collision process in each sector in the collision diagram. Sectors I to VI refer to the sectors I to VI in the collision diagram in the present thesis.

Transition between coalescence and bouncing

In relatively low Weber number regime (sector I, II and III), the collision outcome undergoes a non-monotonic coalescence-bouncing-coalescence transition. In sector I, the droplets approach each other with very small inertia and coalesce into a single larger droplet. The droplets move so slowly that the gas phase hardly resists the approach of the droplets and the coalescence will occur as long as the distance between the colliding surfaces gets so small that the force of attraction between the molecules of the two droplets, i.e. the Van der Waals force, becomes dominant. The critical distance for the onset of the Van der Waals force is in the order of 10 nm [32]. In sector II, the droplets collide with higher inertia resulting in a high pressure in the gas phase between the colliding droplets due to the viscous resistance against the drainage of the gas film. The high pressure in the gas phase prevents a further approach of the droplets. As a result, the liquid in the droplets flows outward near the collision plane and the colliding surfaces are enlarged, forming a gas layer in-between. In the next stage, the droplets recede due to the surface tension force and bounce apart from each other without material exchange. If the inertia is further elevated, the colliding surfaces will approach each other more closely. When the local gas layer thickness is small enough for the Van der Waals force to become effective, the droplets coalesce (in sector III). For a simplification of the discussion, the gas phase between the colliding droplets at very low Weber number regime (in sector I) is also called a gas layer, though its resisting effect is almost nil. Based on this phenomenological description, it is the competition between the resisting effect of the gas layer and the intermolecular forces that ultimately determines whether the droplets merge into a single droplet or bounce apart. This phenomenological description is partly based on the work of Zhang and Law [71].

Zhang and Law [71] pointed out that before the possible coalescence of the droplets, the distance of the colliding surfaces must necessarily pass through a region where it is comparable with the mean free path of the gas molecules. Aiming at the prediction of the non-monotonic coalescence-bouncing-coalescence transition for head-on collisions and assuming Poiseuille flow between two expanding flattened interfaces in the gas film, Zhang et al. [71] established an analytical model that accounts for the motion and deformation of the droplets and the interaction between the droplets and gas. The resisting effect of the gas layer acts in the form of a pressure force acting on the droplet's surface. The pressure in the gas layer is derived based on the gas drainage, the rarefaction effect and the Van der Waals force. This model is able to predict the non-monotonic coalescence-bouncing-coalescence transition, though the accuracy of the prediction of the critical Weber numbers especially between the sector II and III needs to be further improved. Estrade and Biscos [15] conducted an experimental investigation of binary collision of ethanol droplets and developed a theoretical model for predicting the critical Weber number between sector II and III which derivation is based on the energy conservation. However, the influence of the gas phase is not included in their model, although it plays an important role in the transition between coalescence and bouncing: Qian and Law [45] observed that the sector II (bouncing) expands with increasing ambient pressure.

Numerical simulation results concerning the transition between coalescence and bouncing are rare. Most numerical studies focused on the reproduction of the collision process with prescribed collision outcome and/or detailed description of the flow field, see [38, 36, 37, 41, 40]. The difficulty for a predictive simulation in terms of the collision outcome is that the gas layer becomes so thin that it cannot be resolved by feasible simulations. Trying to tackle this problem, Mason et al. [33] conducted a multi-scale simulation: the macro-scale simulation is conducted by means of the Volume of Fluid (VOF) method, while the flow in the gas layer is modeled by means of the classical lubrication theory. A critical gas layer thickness of 40 nm is used as a coalescence criterion. The simulation can reproduce the coalescence process well, while the transition between coalescence and bouncing is not mentioned. Murad and Law [35] conducted molecular simulations yielding both bouncing and coalescence predictively. The droplet diameter in the simulation is restricted to a few nanometers which is much too small compared to the typical droplet sizes in technical applications. Resolving the droplet collision process with molecular simulations in technical applications is not realistic, since within one cubic centimeter air under standard conditions there are already roughly 10^{19} molecules, the solution of which is far beyond the capability of modern high-performance computing technology.

Transition between coalescence and separation

In near head-on collisions in sector III and IV, the coalesced collision complex expands first outwards after the onset of the coalescence and then retracts due to the surface tension force temporarily forming a cigar-like shape. The cigar-like shape collision complex breaks into two main droplets with contingent secondary droplets at relatively high inertia of the colliding droplets (sector IV). At relatively smaller Weber numbers in sector III, the collision complex stays as a single droplet after an oscillation, through which a part of the kinetic energy is dissipated. At relatively high inertia and high impact parameter in sector V, the collision complex falls apart after the collision complex is elongated due to the inertia and centrifugal force.

Many previous studies have been devoted to modeling the boundary curves between sector III and IV and between III and V. Ashgriz and Poo [5] developed correlations for the boundary curves III-IV and III-V based on the inviscid assumption. Qian and Law [45] showed that the critical Weber number between the sector III and IV is linearly dependent on the Ohnesorge number in case of head-on collisions. Jiang et al. [25] proposed a model for the boundary curve III-V which accounts for the viscous effect. Sommerfeld et al. [62] developed a composite universal model which is an extension and combination of the model of Ashgriz and Poo [5] and the model of Jiang et al. [25]. This model is able to predict the boundary curves III-IV and III-V in a large span of viscosity variation. Planchette et al. [42] deduced the critical velocity distinguishing coalescence and separation in head-on collisions based on an energy balance of the expansion phase and the retracting phase of the collision process combined with a Rayleigh-like fragmentation criterion.

The numerical studies have been able to reproduce the boundary curves between coalescence and separation. Rieber and Frohn [52] predict the boundary curves by means of a Volume of Fluid (VOF) code called Free Surface 3D, which is also applied in the numerical studies in this

work. These curves are in good agreement with corresponding experiments of Brenn and Frohn [11] and Ashgriz and Poo [5]. Pan and Suga [41] reproduced the collision outcomes in section III, IV and V by means of the Level-Set method, which locates the interfacial position by means of transporting a signed distance function, without giving the collision outcome in advance. Saroka et al. [57], using the VOF method, found that the boundary between sector III and IV in case of head-on collision depends on Reynolds number and the dependence decreases with increasing Reynolds number. One issue arising in the simulation is that the liquid lamella of the collision complex, which emerges in the middle of the collision complex in the expanding phase after coalescence of the colliding droplets at relatively high Weber numbers, ruptures in the numerical simulations [41, 37, 17, 18]. The rupture of the liquid lamella deteriorates the accuracy while predicting the collision outcomes. Focke and Bothe [17] and Focke and Bothe [18] dealt with this problem by correcting the computation of the surface tension force in the lamella region. The advantage of using numerical methods in order to study the transition between coalescence and separation is that it is very easy to separately modify each of the parameters in the collision system, which facilitates a comprehensive and systematic study of the dependency of the boundary curves on the system parameters and the validation of the above mentioned theoretical models predicting the boundary curves III-IV and III-V.

Spatter in sector VI

Spatter is a significantly different phenomenon emerging at collisions with large kinetic energy. Roth et al. [56] conducted experimental studies on head-on binary collisions of iso-propanol droplets at Weber numbers ranging from 1030 to 2876. Their results show that with increasing Weber number, the rim of the collision complex becomes increasingly unstable. If the Weber number is high enough, secondary droplets are spattered out from the rim of the collision complex. They also conducted numerical simulations but only qualitatively and at relatively low Weber numbers due to the high requirement on the computational effort resulting from high collision energies. Despite the lower Weber number in their numerical simulations, the instability of the rim is too strong compared to the experimental results. Pan et al. [39] conducted an experimental study of head-on binary droplet collisions at Weber numbers up to about 5000. They presented clear images for the deformation history of water collision complexes. Their results show that the instability of the rim of the water collision complex emerges at much smaller Weber numbers compared to iso-propanol droplets. Kuan et al. [27] conducted a numerical study of head-on collisions of water droplets at high Weber numbers, employing a parallel, adaptive interface tracking method, and compared their results with the experimental work of Pan et al. [39]. Their simulations capture the unstable rim of the collision complex and show good agreement with corresponding experimental results of Pan et al. [39] up to $We = 442$. However, their comparisons of the collision complex shapes for $We > 442$ are either incomplete regarding the length of the physical simulation time or do not show a good agreement.

Understanding the spatter phenomenon, especially the mechanism of the rim instability of the collision complex, is not only a scientific desire but also a precondition for predicting the bound-

ary curve between the section V and VI. It is even more desirable to predict the size spectrum of secondary droplets ejected from the unstable rim due to its important role in determining the characteristics of a spray. Moreover, the study of the mechanism of the rim instability is of more general importance, since a similar phenomenon of spattering of secondary droplets from an unstable rim emerges also in collisions of a droplet on a solid substrate or on a liquid film.

1.3 Organization of the thesis

The present thesis originates within the framework of the Transregio-75 (TRR-75) of the German Research Foundation (DFG) “Droplet Dynamics Under Extreme Ambient Conditions”. The driving force of this thesis is the realization of the prediction of the collision outcome in terms of bouncing versus coalescence and in terms of the onset of spatter as well as the prediction of the size spectrum of the secondary droplets resulting from the spatter phenomenon.

In order to seek the final goal, namely the prediction of the collision outcomes, the following sub-goals have been set:

- Explanation of the rim instability that is present on the spatter phenomenon due to its importance in the onset of spatter and in the size spectrum of the secondary droplets.
- Development of numerical methods that enable the reproduction of the spatter phenomenon.
- Development of numerical methods that enable the reproduction of the bouncing and coalescence phenomena, at first with prescribed collision outcome.
- Acquisition of the flow properties in the gas flow between the colliding droplets before possible coalescence.
- Development of a SGS model that solves the flow in the gas layer and that is integrated into the main solver FS3D.
- Numerical simulation by means of the integrated SGS model and the corresponding assessment in terms of the capability of predicting bouncing versus coalescence.

The developments and the numerical investigations are restricted to the head-on collisions. The structure of this work is as follows. In Chapter 2, the governing equations of two-phase incompressible flows are presented. Two most important interfacial instabilities and the continuum hypothesis as well as its transition to the rarefaction effect are addressed. The basic numerical methods used in this work are introduced in Chapter 3. The models for the computation of the surface tension force are discussed in terms of their advantages and limitations. Chapter 4 describes the problem of the artificial interaction while computing the surface tension force of a thin lamella, which can be either a liquid lamella in high energetic collisions or a gas film at lower collision energy, and delivers numerical methods that deal with this problem. In Chapter 5, the spatter phenomenon is in depth investigated based on the numerical results. One highlight is the rigorous theoretical/computational confirmation of the mechanism

of the rim instability in the context of binary droplet collisions. In Chapter 6, the results of a 2D simulation with very high grid resolution focusing on the flow in the gas layer between the colliding droplets are presented. The derivation, implementation and validation of a SGS model, which solves the flow in the gas layer, are presented in Chapter 7. Preliminary results on predictive simulations by means of multi-scale simulations are discussed. At the end of this thesis, a summary and an outlook are given.

2 Mathematical Modeling of Two-Phase Fluid Systems

In continuum mechanics, a two-phase fluid system is characterized by an interface separating two immiscible substances. Due to the jump of material properties over the interface, the differential equations describing the two-phase fluid system differ from those for a single phase flow. These equations are given first in this chapter. Then, two kinds of interfacial instabilities are introduced, which serve as a basis for further investigation of the instabilities occurring in the context of binary droplet collisions. At the end of this chapter, the continuum hypothesis and its transition to the rarefaction effect are addressed.

2.1 Governing equations in incompressible two-phase fluid systems

We consider a material control volume $V(t)$ moving with the flow, see Figure 2.1. The control volume possesses a normal vector \mathbf{n} pointing outwards and contains two phases separated by a free interface $\Gamma(t)$. The two phases are denoted by $\Omega^+(t)$ and $\Omega^-(t)$ and the normal vector of the interface \mathbf{n}_Γ points to $\Omega^+(t)$. Furthermore, the intersection of $\Gamma(t)$ with the surface of $V(t)$ is bounded by a curve $C(t)$ with a normal vector \mathbf{N} pointing outwards and lying tangential to $\Gamma(t)$.

Assuming no-slip condition between the tangential velocity components at the interface, i.e.

$$u_{\text{tan}}^+ = u_{\text{tan}}^- = u_{\Gamma\text{tan}}, \quad (2.1)$$

the conservation equation for an extensive quantity Φ with density ϕ is given as [9]:

$$\begin{aligned} \frac{d}{dt} \int_{V(t)} \phi dV = & - \int_{\partial V(t)} \mathbf{j}_{\text{mol}} \cdot \mathbf{n} dA + \int_{V(t)} P dV \\ & - \int_{C(t)} \mathbf{j}_\Gamma^{\text{mol}} \cdot \mathbf{N} ds + \int_{V(t) \cap \Gamma(t)} P_\Gamma dA. \end{aligned} \quad (2.2)$$

The density ϕ can be either a scalar or a vector. The first term on the right-hand side of equation (2.2) describes the change of ϕ through transport. Since $V(t)$ is a material control volume, only diffusive (molecular) transport comes into play. The third term describes the change of ϕ by surface diffusion through the curve $C(t)$. The second and the fourth terms are volume-specific and surface-specific source terms, respectively. Given ϕ , P , P_Γ , \mathbf{j}_{mol} and $\mathbf{j}_\Gamma^{\text{mol}}$ properly, the conservation equations for mass and momentum can be derived.

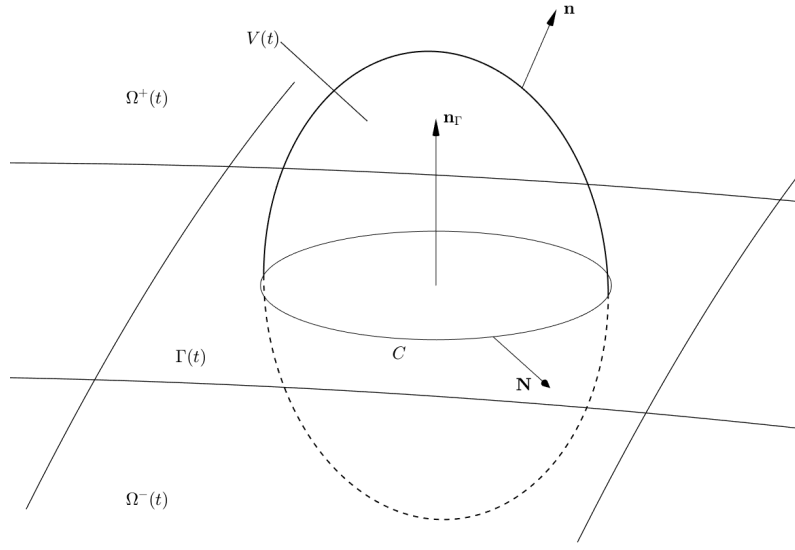


Figure 2.1.: Description of a two-phase fluid system.

2.1.1 Mass conservation

Mass is an extensive quantity with ρ denoting its density. We assume that the interface does not carry mass, hence $\mathbf{j}_\Gamma^{\text{mol}} = 0$. With $\phi = \rho$, $\mathbf{j}_{\text{mol}} = 0$, $P = 0$ and $P_\Gamma = 0$, the mass conservation equations are given as

$$\frac{\partial \rho}{\partial t} + \nabla \cdot (\rho \mathbf{u}) = 0 \quad \text{in } \Omega^+ \cup \Omega^-, \quad (2.3)$$

$$[[\rho(\mathbf{u} - \mathbf{u}_\Gamma)]] \cdot \mathbf{n}_\Gamma = 0 \quad \text{at } \Gamma(t), \quad (2.4)$$

where \mathbf{u}_Γ denotes the interface velocity and \mathbf{u} the velocity in the bulk. The notation $[[\cdot]]$ denotes the jump of a quantity across the interface, which is defined as

$$[[\Psi]](\mathbf{x}) = \lim_{h \rightarrow 0^+} (\Psi(\mathbf{x} + h\mathbf{n}_\Gamma(\mathbf{x})) - \Psi(\mathbf{x} - h\mathbf{n}_\Gamma(\mathbf{x}))). \quad (2.5)$$

For incompressible fluids of constant density without phase change, equations (2.3) and (2.4) can be further reduced to

$$\nabla \cdot \mathbf{u} = 0 \quad \text{in } \Omega^+ \cup \Omega^-, \quad (2.6)$$

$$\mathbf{u}^+ \cdot \mathbf{n}_\Gamma = \mathbf{u}_\Gamma \cdot \mathbf{n}_\Gamma = \mathbf{u}^- \cdot \mathbf{n}_\Gamma \quad \text{at } \Gamma(t). \quad (2.7)$$

The equation (2.6) is the corresponding volume conservation equation for incompressible flow. The equation (2.7) describes that the velocity component perpendicular to the interface is continuous. With the assumption (2.1), the jump condition of the velocity field is summarized as

$$[[\mathbf{u}]] = 0 \quad \text{at } \Gamma(t). \quad (2.8)$$

2.1.2 Transport equation of the phase indicator

We define a phase indicator χ with value 1 in Ω^+ and 0 in Ω^- . Then the local density and dynamic viscosity are given as

$$\rho = \chi\rho^+ + (1 - \chi)\rho^-, \quad (2.9)$$

$$\eta = \chi\eta^+ + (1 - \chi)\eta^-. \quad (2.10)$$

For incompressible fluids of constant density without phase change, the transport equation of the phase indicator is given as

$$\frac{\partial \chi}{\partial t} + \nabla \cdot (\chi \mathbf{u}) = 0 \quad \text{in } \Omega^+ \cup \Omega^-. \quad (2.11)$$

The transport equation (2.11) is the central equation solved in the VOF method, which details are described in Chapter 3.

2.1.3 Momentum conservation

Given $\phi = \rho \mathbf{u}$, $\mathbf{j}_{\text{mol}} = \mathbf{S} - p\mathbf{I}$, $\mathbf{j}_{\Gamma}^{\text{mol}} = \sigma(\mathbf{I} - \mathbf{n}_{\Gamma} \otimes \mathbf{n}_{\Gamma})$, $P = \rho \mathbf{f}$, $P_{\Gamma} = 0$ for incompressible flows without phase change [51], the momentum conservation equations are written as

$$\frac{\partial}{\partial t}(\rho \mathbf{u}) + \nabla \cdot (\rho \mathbf{u} \otimes \mathbf{u}) = \nabla \cdot \mathbf{T} + \rho \mathbf{f} \quad \text{in } \Omega^+ \cup \Omega^-, \quad (2.12)$$

$$[[-\mathbf{T}]] \cdot \mathbf{n}_{\Gamma} = \sigma \kappa \mathbf{n}_{\Gamma} \quad \text{at } \Gamma(t), \quad (2.13)$$

where σ is the surface tension assumed to be constant, κ is the interface curvature, and \mathbf{f} denotes the body force. For Newtonian fluids, the stress tensor \mathbf{T} is given as

$$\mathbf{T} = -p\mathbf{I} + \mathbf{S}, \quad (2.14)$$

with $\mathbf{S} = \eta(\nabla \mathbf{u} + (\nabla \mathbf{u})^T)$ in incompressible flow. The momentum equations (2.12) for Newtonian fluids are called the Navier-Stokes equations, which are valid in both phases.

For a two-phase fluid system at rest, i.e. a static droplet or bubble in a surrounding fluid, the momentum jump condition can be further reduced to the Young-Laplace equation, giving the Laplace pressure jump across the interface:

$$\Delta p = \sigma \left(\frac{1}{R_1} + \frac{1}{R_2} \right), \quad (2.15)$$

where R_1 and R_2 are the curvature radii of the interface.

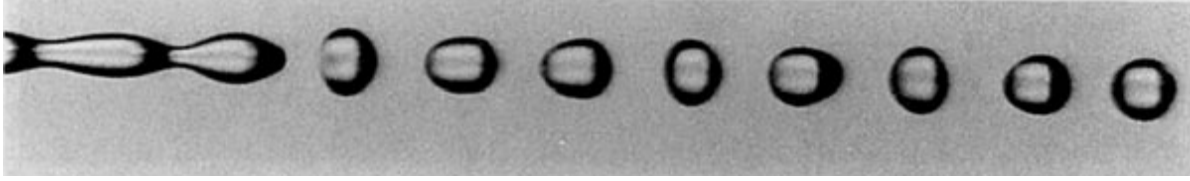


Figure 2.2.: Breakup of a water jet due to the capillary effect [66].

2.1.4 Differential equations governing the flow in two-phase fluid systems

Since the surface tension force only acts at the interface, the momentum jump condition can be added to the momentum conservation equation as a singular interface term by using a δ -function yielding the one-field formulation of the Navier-Stokes equations. The differential equations governing the hydrodynamics of incompressible two-phase flows, including the one-field formulation of the Navier-Stokes equations, are summarized below:

$$\nabla \cdot \mathbf{u} = 0, \quad (2.16)$$

$$\frac{\partial \rho}{\partial t} + \nabla \cdot (\rho \mathbf{u}) = 0, \quad (2.17)$$

$$\frac{\partial}{\partial t}(\rho \mathbf{u}) + \nabla \cdot (\rho \mathbf{u} \otimes \mathbf{u}) = -\nabla p + \nabla \cdot \mathbf{S} + \rho \mathbf{f} + \sigma \kappa \mathbf{n}_\Gamma \delta. \quad (2.18)$$

2.2 Interfacial instabilities

In two-phase incompressible flows, the interface between the two phases is unstable in certain conditions, meaning that a small disturbance on the interface will be magnified by the fluid system. Two kinds of interfacial instabilities are addressed in this section, namely the Plateau-Rayleigh (PR) instability and the Rayleigh-Taylor (RT) instability, which are the candidate theories for the explanation of the rim instability emerging in spatter phenomenon that will be discussed in Chapter 5.

2.2.1 Plateau-Rayleigh instability

A straight free liquid jet in a gaseous surrounding is unstable due to the capillary effect and breaks into a chain of small droplets; see Figure 2.2 for an example. This kind of instability is referred to as the Plateau-Rayleigh (PR) instability.

This phenomenon has been explained analytically by Lord Rayleigh [46], assuming an inviscid liquid. The instability of the jet begins with a tiny perturbation that is in form of, e.g., surface displacement, pressure or velocity fluctuations in the fluid system. The disturbances in the axial direction of the jet are magnified with wave numbers less than a cut-off wave number k_c , and are decaying otherwise. The wave number with the maximum growth rate decides the number and the size of the resultant droplets. In order to go into more detail, we consider a harmonic axial

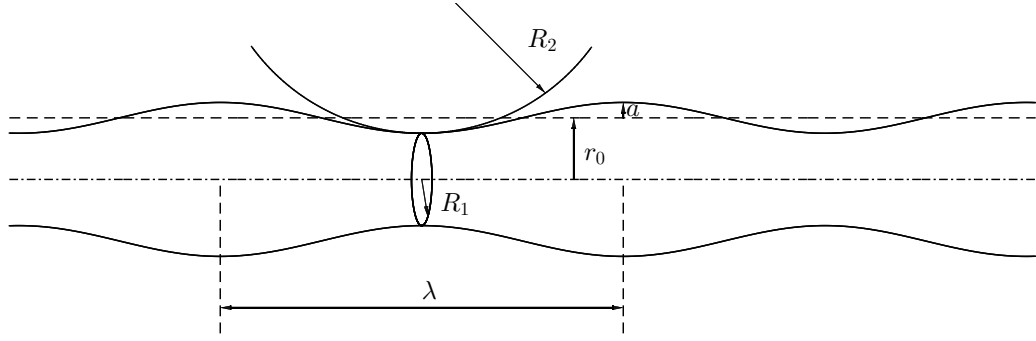


Figure 2.3.: Schematic representation of an unstable jet.

disturbance on a straight fluid jet with initial radius r_0 and an infinite length (see Figure 2.3) and conduct a dimensional analysis of the Navier-Stokes equations. The disturbance is described by wavelength λ , frequency $\bar{\omega}$, and amplitude a . According to Ashgriz and Nasser [4], the characteristic length and the characteristic time of the problem are λ and $1/\bar{\omega}$, respectively. The characteristic fluid velocity due to the interface motion is estimated as $U \approx a\bar{\omega}$. Therefore, the time derivative term, the convective term and the Laplacian term of the Navier-Stokes equations are estimated as $\rho \partial \mathbf{u} / \partial t \sim \rho U \bar{\omega} \sim \rho a \bar{\omega}^2$, $\nabla \cdot (\rho \mathbf{u} \otimes \mathbf{u}) \sim \rho U^2 / \lambda \sim \rho a^2 \bar{\omega}^2 / \lambda$, $\eta \Delta \mathbf{u} \sim \eta U / \lambda^2 \sim \eta a \bar{\omega} / \lambda^2$, accordingly. Comparing the time derivative and the convective term shows that the non-linear convective term can be neglected if $a \ll \lambda$. The Reynolds number is given as $Re = \rho U \lambda / \eta \approx \rho a \lambda \bar{\omega} / \eta$. Comparing the time derivative and the viscous term shows that the viscous term can be neglected when $\rho \lambda^2 \bar{\omega} / \eta = Re \lambda / a \gg 1$.

Neglecting the viscous effect and linearizing the Navier-Stokes equations written in cylindrical coordinates, the growth rate of a small-amplitude harmonic disturbance is given as (for detailed derivation see [4] or the original work [46])

$$\omega^2 = \frac{\sigma k}{\rho r_0^2} (1 - k^2 r_0^2) \frac{I_1(k r_0)}{I_0(k r_0)}, \quad (2.19)$$

where $\omega = \omega_r + i\omega_i$ is the growth rate, k is the wave number, I_n are modified Bessel functions of the first kind. If the real part of the growth rate ω_r is positive, the disturbance grows exponentially in time. In the parentheses in equation (2.19), $k^2 r_0^2$ comes from the jet axial curvature and '1' from the jet sectional curvature which represents the capillary pinching. Since the ratio of the modified Bessel functions I_1/I_0 is positive for all conditions, the jet is unstable if the capillary pinching is dominant:

$$1 > k^2 r_0^2, \quad (2.20)$$

or equivalently:

$$\lambda > 2\pi r_0. \quad (2.21)$$

The cut-off wave number for the instability is therefore given as $k_c = 1/r_0$. The spectrum of the growth rate for an inviscid jet is plotted in Figure 2.4. The fastest growing perturbation dominating the jet evolution occurs at $kr_0 = 0.697$, which can be used to estimate the break length of the fluid jet and, furthermore, the size of the generated droplets.

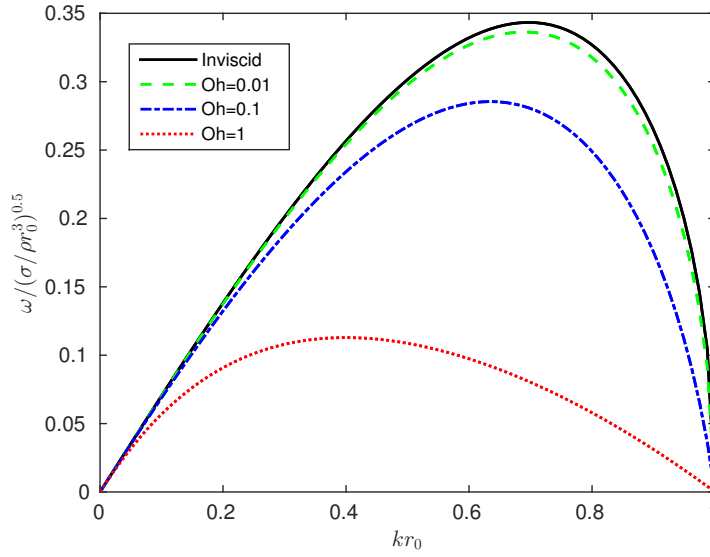


Figure 2.4.: Non-dimensional growth rate of instabilities on inviscid and viscous jets with respect to the wave number.

Weber [68] and Chandrasekhar [12] extended Rayleigh's inviscid theory concerning viscosity effect. The corresponding characteristic equation for the perturbation spectrum is given as

$$\begin{aligned} \omega^2 + \frac{2\eta k^2}{\rho I_0(kr_0)} \left(I_1'(kr_0) - \frac{2kl}{k^2 + l^2} \frac{I_1(kr_0)}{I_1(lr_0)} I_1'(lr_0) \right) \omega \\ = \frac{\sigma k}{\rho r_0^2} (1 - k^2 r_0^2) \frac{I_1(kr_0)}{I_0(kr_0)} \frac{l^2 - k^2}{l^2 + k^2}, \end{aligned} \quad (2.22)$$

where $l^2 = k^2 + \rho\omega/\eta$. For $\eta = 0$, this expression reduces to equation (2.19). The influence of viscosity on the growth rate is shown in Figure 2.4 regarding Ohnesorge numbers defined as $Oh = \eta/\sqrt{r_0\rho\sigma}$. One sees that the maximum growth rate and the dominant wavenumber decrease with increasing viscosity, while the cut-off wave number remains $k_c = 1/r_0$.

2.2.2 Rayleigh-Taylor instability

The Rayleigh-Taylor (RT) instability is an instability of interface between two fluids with different densities. It occurs when the lighter fluid supports the heavier fluid under gravity or equivalently, under an acceleration of the fluid system in the direction towards the denser fluid. Figure 2.5, obtained from own numerical simulations, illustrates the development of the RT instability under gravity.

The classical modeling of the Rayleigh-Taylor instability given by Taylor [63] assumes two inviscid fluids with density ρ_1 and ρ_2 originally at rest with $\rho_1 > \rho_2$. The gravitational field g points to the lighter fluid. Derived on the basis of potential theory, the growth rate of a small harmonic perturbation at the interface is given as

$$\omega(k) = \sqrt{kgA}, \quad (2.23)$$

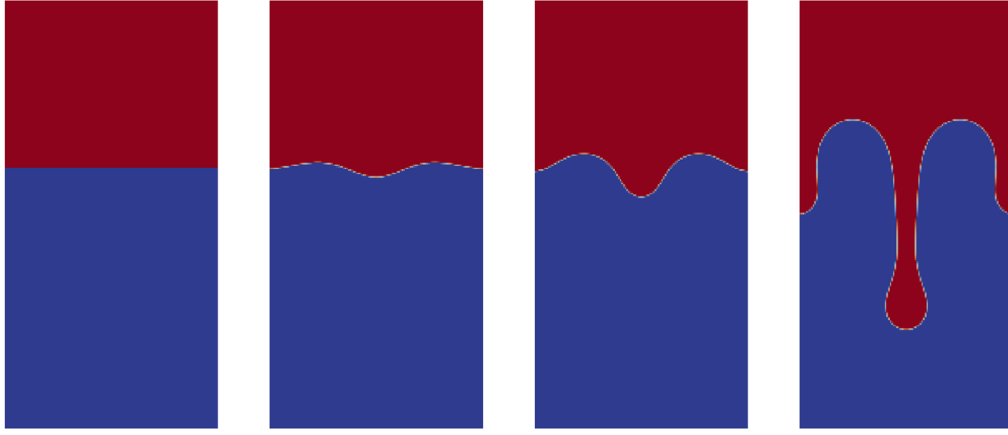


Figure 2.5.: Development of the Rayleigh-Taylor instability under gravity.

where $A = (\rho_1 - \rho_2)/(\rho_1 + \rho_2)$. With $A > 0$, the instability exists for every positive wavenumber k . For large wave numbers, it is natural to expect that the surface tension force will stabilize the instability, which is indeed the case. According to Bellman et al. [6], who extended the RT instability theory concerning the effect of the surface tension force, the interface perturbation is dampened for

$$k < \sqrt{\frac{(\rho_1 - \rho_2)g}{\sigma}}. \quad (2.24)$$

The fastest growth rate is given as

$$\omega_{\max} = \sqrt{\frac{2A}{3\sqrt{3}\sigma} g \sqrt{(\rho_1 - \rho_2)g}}, \quad (2.25)$$

occurring at wavenumber

$$k = \frac{1}{\sqrt{3}\sigma} \sqrt{(\rho_1 - \rho_2)g}. \quad (2.26)$$

2.3 Continuum mechanics and rarefied gas flow regimes

It is well known that gas is composed of discrete molecules or atoms on the microscopic scale. If the length scale of a given volume is large enough, the average property of the gas is not influenced by the concrete number of molecules in this volume. For example, there exist 3×10^{10} molecules in 10^{-9} cm^3 air under standard temperature and pressure conditions ensuring the average sense of the gas property [60]. On the basis of this conception, continuum mechanics assumes that the substance of the object completely fills the space it occupies and the property at a point is continuous (even twice continuously differentiable) function of coordinates and time allowing the description of the motion of the continuum by partial differential equations.

We introduce the Knudsen number for the gas medium defined as

$$\text{Kn} = \frac{\lambda}{L}, \quad (2.27)$$

where λ is the mean free path of the gas and L is the characteristic length scale of the flow. The continuum hypothesis is valid for very small Knudsen numbers, i.e. $\text{Kn} \ll 1$. For a gas flow with the mean free path of the gas comparable to the characteristic length scale of the flow, i.e. $\text{Kn} > 0.01$, the flow is regarded as rarefied. According to the rarefaction degree, the rarefied gas flow can be divided into three regimes [65]:

$$\begin{aligned} 0.01 < \text{Kn} < 0.1 & \quad \text{Slip flow regime,} \\ 0.1 < \text{Kn} < 10 & \quad \text{Transitional regime,} \\ \text{Kn} > 10 & \quad \text{Free molecular regime.} \end{aligned}$$

In the free molecular regime, the collisions between molecules and the collision of the molecules with the surface of a body have to be taken into account, which makes the problem more complicated and put it beyond the scope of the present work. In the slip flow regime, the continuum hypothesis can still be used; but it is necessary to introduce some modifications to the boundary conditions. For particular cases, it is also possible to extend the method used in the slip flow regime to the transitional regime. This issue will be further addressed in Chapter 7.

3 Numerical Methods

3.1 Finite Volume discretization

The numerical simulations in this thesis are performed with the Computational Fluid Dynamic (CFD) program Free Surface 3D (FS3D), which was originally developed at the ITLR (University of Stuttgart) [51] and has been extended both at the ITLR and in the Mathematical Modeling and Analysis (MMA) group of Technische Universität Darmstadt. FS3D is based on the Finite Volume (FV) method. The basic concept of the Finite Volume method is described by dealing with the conservation equation for an extensive quantity Φ with density ϕ in a fixed control volume:

$$\frac{d}{dt} \int_V \phi dV = \int_V P dV + \int_S \mathbf{F} \cdot \mathbf{n} dS, \quad (3.1)$$

where P and \mathbf{F} summarize all the source terms and the fluxes, respectively. Discretizing the domain into finite control volumes in cuboidal form, applying the above equation for each control volume Ω with surfaces $l = 1, \dots, 6$ and integrating over time step $\delta t = t^{n+1} - t^n$ yield

$$\int_{\Omega} \phi(t^{n+1}) dV - \int_{\Omega} \phi(t^n) dV = \int_{\Omega} \int_{t^n}^{t^{n+1}} P dt dV + \sum_{l=1}^{l=6} \int_{S_l} \int_{t^n}^{t^{n+1}} \mathbf{F} dt \cdot \mathbf{n}_l dS. \quad (3.2)$$

Approximation of the spatial average values by the values of the center of the control volumes or by the values of the center of the cell faces constructs the foundation of the Finite Volume method. For unsteady problems, the time averaged values are approximated by the values at the new or the last time step.

In FS3D, a cuboidal box serving as the computational domain is discretized into cuboidal cells. Specifically within this work, the edge lengths of the computational cells are restricted to be equidistant. Two layers of dummy cells are settled around the domain, which are used to employ the boundary conditions as suggested by Blazek [7]. The variables are arranged in a staggered way according to the MAC scheme [23], whereby the pressure and other scalar variables like the volume fraction are stored in cell centers and the velocity components are stored at cell faces separately. This staggered grid arrangement prevents an oscillating pressure field [58].

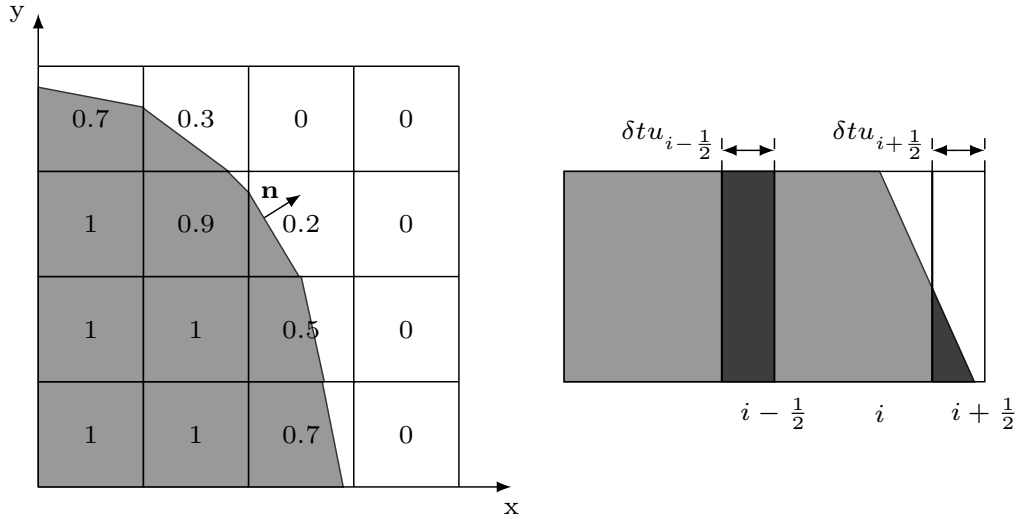


Figure 3.1.: Schematic description of the PLIC algorithm. Left: Reconstruction of the Interface. Right: Computation of the flux through cell faces. The volumes in the dark area are the advected volumes of fluid in one time step. The velocities in x-direction at cell faces are positive in this example.

3.2 Volume of Fluid method

Within this thesis, the Volume of Fluid method, originally developed by Hirt and Nichols [23], is employed for locating and tracking the interface position. In the VOF method, the transport equation

$$\frac{\partial \chi}{\partial t} + \nabla \cdot (\chi \mathbf{u}) = 0 \quad (3.3)$$

is solved for the phase indicator χ , which has the value one in the liquid phase and zero otherwise. Integrating the phase indicator function over the volume of a computational cell and then dividing the integral by the cell volume gives the volume fraction of the liquid phase in finite volume discretizations. The volume fraction is denoted by f and has the value

$$\begin{cases} 1 - \epsilon < f \leq 1 & \text{in the liquid phase,} \\ 0 \leq f < \epsilon & \text{in the gas phase,} \\ \epsilon \leq f \leq 1 - \epsilon & \text{in cells containing interface,} \end{cases} \quad (3.4)$$

where the numerical threshold ϵ is set to 10^{-6} in FS3D.

The transport equation (3.3) is solved by means of the Piecewise Linear Interface (Re-)Construction (PLIC) algorithm [50]. First, the interface is reconstructed by fulfilling two conditions simultaneously:

1. The interface is locally approximated by a plane possessing a normal vector \mathbf{n} given as

$$\mathbf{n} = -\frac{\nabla f}{\|\nabla f\|}. \quad (3.5)$$

For computing ∇f , the components of ∇f are evaluated at cell faces by central differencing. The obtained values are then averaged to obtain ∇f located at cell vertices. Averaging ∇f located at all vertices of one cell yields an approximation of ∇f which is located at the cell center. In total, a 27 (3^3) cells stencil is used for computing ∇f , so as for computing n .

2. The approximated interface and the wetted cell faces enclose the volume $f \Delta x \Delta y \Delta z$.

The reconstructed interface is exemplarily shown in Figure 3.1. Instead of solving the volume transport equation (3.3) directly, this advection equation is split into three one-dimensional transport equations that are solved successively. Furthermore, the volume transport equation is complemented with a divergence corrector, which ensures that the cells in the interior of the liquid phase are not confused with interface cells. The flux of the liquid phase through cell faces for one time step, e.g. in x-direction, is then the volume of the liquid phase located in the volume $u \delta t \Delta y \Delta z$; see Figure 3.1 for a schematic description in 2D. The procedure of the computation of the volume flux in each direction is the same; the sequence of computing the three split equations is symmetric between two subsequent time steps, which guarantees a second-order procedure. After one of the three one-dimensional transports, the f -values could be larger than one or smaller than zero in badly conditioned cells. The f -values are restricted between zero and one through a post-correction. For more details, we refer to [51].

Having the updated volume fraction in each cell, the local material properties can be approximated:

$$\rho = f \rho_L + (1 - f) \rho_G, \quad (3.6)$$

$$\eta = f \eta_L + (1 - f) \eta_G, \quad (3.7)$$

where the subscripts L and G denote the liquid phase and the gas phase, respectively. With given volume fractions, the so-called height function can be computed, which describes the distance of the interface to a given reference surface. The height function h can be written based on an elementary volume between the interface and a projected area serving as reference:

$$h = \lim_{dA \rightarrow 0} \frac{\iint h dA}{dA}, \quad (3.8)$$

where $\iint h dA$ is the volume of fluid between the interface and the projected area dA . It is possible to find the height function in three space directions. Taking z direction for example, one can approximate $\iint h dA$ by summing up the volume fractions in a cell column having the bottom area $\Delta x \cdot \Delta y$:

$$V = \sum_{k=1}^n (f(k) \cdot \Delta z(k)) \cdot \Delta x \cdot \Delta y, \quad (3.9)$$

where k indicates the cell and runs from the cell lying on the reference surface to the cell containing only gas phase in z direction. The height function can then be computed:

$$h = \frac{V}{\Delta x \cdot \Delta y} = \sum_{k=1}^n f(k) \cdot \Delta z(k). \quad (3.10)$$

The equation (3.10) computes the height function based on the liquid phase and the reference surface must be within the liquid phase. Reversing the f -values, the height function with respect to a reference surface that is located in the gas phase can be computed with equation (3.10) as well.

3.3 Modeling of the surface tension force

In order to employ the one-field formulation of the Navier-Stokes equations, the surface tension force \mathbf{f}_Γ has to be approximated. In the context of the Volume of Fluid method, the following approximations are performed:

$$\delta \approx \|\nabla \tilde{f}\|, \quad (3.11)$$

$$\tilde{\mathbf{n}} \approx -\frac{\nabla \tilde{f}}{\|\nabla \tilde{f}\|}, \quad (3.12)$$

$$\kappa \approx \nabla \cdot (-\tilde{\mathbf{n}}), \quad (3.13)$$

yielding the Continuum-Surface-Force (CSF) model [10] for computing the surface tension force:

$$\mathbf{f}_\Gamma = \sigma \kappa \delta \mathbf{n} \approx \sigma \kappa \nabla \tilde{f}. \quad (3.14)$$

The surface normal $\tilde{\mathbf{n}}$ and the delta function δ are computed on the basis of a smoothed volume fraction field \tilde{f} . The smoothing is conducted by means of a second-order B-Spline function. As a result, the surface tension force is computed not only on the interface but in a small region around the interface, acting as a volumetric force.

The CSF model suffers from the well-known parasitic currents: the velocity field around the interface oscillates unphysically. As a result, a spherical droplet with zero initial kinetic energy in resting environment, which is expected to be silent, will oscillate and move in an unpredictable way [2]. The parasitic currents can be significantly suppressed by discretizing ∇f instead of $\nabla \tilde{f}$ in the same manner as discretizing the pressure gradient ∇p , since the surface tension force can then be balanced by the pressure jump due to the compatible discretization [8]. This balanced version of the discretization of ∇f leads to the balanced-CSF model for computing the surface tension force.

Aside from the discretization of ∇f , it is necessary to compute the interface curvature accurately in the balanced-CSF model. The well-known variants of the balanced-CSF model are from Renardy and Renardy [49], Francois et al. [20] and Popinet [43], whereby the main difference

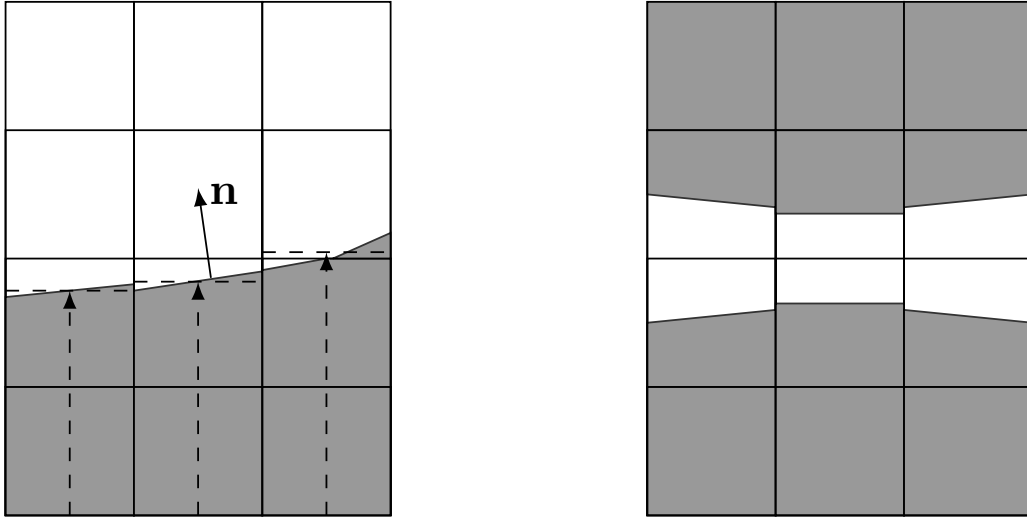


Figure 3.2.: Left: Computation of the interface curvature by means of height functions in direction of the maximum component of the interface normal. Right: A fragment of two approaching droplets as an example scenario.

lies in the estimation of the interface curvature. Renardy and Renardy [49] estimate the interface curvature through computing the curvature of a fitted paraboloid obtained on the basis of volume conservation. Francois et al. [20] estimate the interface curvature based on height functions constructed in a fixed region around the interface cells. In this thesis, the implementation of Popinet [43] is adopted. The algorithm estimates the interface curvature through three hierarchical methods. The interface curvature is preferably computed by means of height functions constructed in cell columns that align with the direction of the maximum component of the interface normal; see a 2D example in Figure 3.2. The curvature in 2D can be determined by means of the height functions:

$$\kappa = \frac{h_{xx}}{(1 + h_x^2)^{3/2}}. \quad (3.15)$$

If not all necessary height functions for computing the surface curvature can be found, the construction of the height function is conducted in the other space directions. In case the computation of the surface curvature by means of height functions is not possible, the computation is conducted with a fallback strategy, namely paraboloid fitting of the interface by means of height functions found in all the three space directions. If this is still not possible, the fitting is conducted by means of the barycenters of the PLIC surfaces. The fitting in the fallback strategies is conducted in a 27 (3^3 , and 3^2 in 2D) cells stencil. The total algorithm is rather sophisticated and the details can be found in the original work of Popinet [43].

It should be noted that in the cell columns where the volume fractions are summed for the computation of the height functions, an empty cell and a full cell must be identified, since the summation of the volume fractions is conducted between them. This leads to a limitation of the application of the implemented balanced-CSF method especially in simulating binary droplet



Figure 3.3.: Unphysical interface oscillation near contact area in a binary droplet collision. Three symmetry planes are employed in the simulation.

collisions, as the construction of a proper height function is not possible when a change in topology, e.g. the coalescence of droplets, is supposed to occur. Take the contact area schematically shown in Figure 3.2 (right) for example, a necessary empty cell for constructing the height function in direction perpendicular to the collision plane cannot be found; in tangential direction, a full cell can not be found. For this scenario, the fallback strategies will be employed in the simulation; however, only unpredictable results will be obtained, since no meaningful fitting is possible for computing the interface curvature in a 3^2 cells stencil in this 2D scenario. In Figure 3.3, a simulation result of a binary droplet collision shows an unphysical oscillation of the interface due to the failure while computing the interface curvature in the contact area. Another limitation of the balanced-CSF model is that it requires higher grid resolution for computing the curvature of sub-structures such as the rim of the collision complex, which is very thin at the early stage of a high energetic collision. The disadvantages of the balanced-CSF model restrict its use for certain scenario.

Another model for computing the surface tension force is the CSS model [28] which computes the surface tension force as

$$\mathbf{f}_T = \nabla \cdot \mathbf{T}, \quad (3.16)$$

with

$$\mathbf{T} = \sigma \|\nabla \tilde{f}\| (\mathbf{I} - \tilde{\mathbf{n}} \otimes \tilde{\mathbf{n}}). \quad (3.17)$$

The CSS model is a conservative model since it is written as a divergence of a tensor of second-order. The CSS model suffers from parasitic currents as well; however, it does not have the problems of the balanced-CSF model described above. In addition, the parasitic currents have relatively less effect at highly dynamic process, which extends the area of applicability of the CSS model. The comparison between the CSS model and the balanced-CSF model is summarized in Table 3.1. In this thesis, the decision of employing the CSS model, the balanced-CSF model or, if needed, a combination of the two models is made based on the advantages and the limitations of the two models in concrete application scenarios. Without explicit indication in

	advantages	limitations
CSS model	<ol style="list-style-type: none"> 1. stable for small sub-structure 2. stable with topology change 3. less problematic in highly dynamic processes, since the parasitic currents are small compared to the velocity field near the interface 	<ol style="list-style-type: none"> 1. parasitic currents
balanced-CSF model	<ol style="list-style-type: none"> 1. much smaller parasitic currents 	<ol style="list-style-type: none"> 1. high grid resolution required for small sub-structures 2. unstable with topology change

Table 3.1.: Comparison between the CSS model and the balanced-CSF model.

this thesis, the CSS model is employed. The unbalanced CSF model is not used in this thesis.

3.4 Time discretization

The time discretization is conducted by means of a first-order explicit Euler scheme, where the key semi-discrete equations are given as:

$$\nabla \cdot \mathbf{u}^{n+1} = 0, \quad (3.18)$$

$$\begin{aligned} \frac{\rho^{n+1} \mathbf{u}^{n+1} - \rho^n \mathbf{u}^n}{\delta t} = & -\nabla \cdot [(\rho \mathbf{u} \otimes \mathbf{u})]^n \\ & + \frac{\rho^{n+1}}{\rho(f^{n+1})} [-\nabla p^{n+1} + \nabla \cdot \mathbf{S}(\mu^{n+1}, \mathbf{u}^n) + \mathbf{f}^{n+1}], \end{aligned} \quad (3.19)$$

$$\frac{\rho^{n+1} - \rho^n}{\delta t} = -\nabla \cdot (\rho \mathbf{u})^n. \quad (3.20)$$

The density $\rho(f^{n+1})$, the viscosity μ^{n+1} and the body force \mathbf{f}^{n+1} in equation (3.19) are computed using the volume fraction at t^{n+1} , which is updated by the VOF method. The semi-discrete momentum equation (3.19) can be rewritten for the velocity at the new time as:

$$\mathbf{u}^{n+1} = \tilde{\mathbf{u}} - \frac{\delta t}{\rho(f^{n+1})} \nabla p^{n+1}, \quad (3.21)$$

with

$$\begin{aligned} \tilde{\mathbf{u}} = & \frac{1}{\rho^{n+1}} [\rho^n \mathbf{u}^n - \delta t \nabla \cdot [(\rho \mathbf{u} \otimes \mathbf{u})]^n] + \\ & \frac{\delta t}{\rho(f^{n+1})} [\nabla \cdot \mathbf{S}(\mu^{n+1}, \mathbf{u}^n) + \mathbf{f}^{n+1}]. \end{aligned} \quad (3.22)$$

The provisional velocity $\tilde{\mathbf{u}}$ is updated by the convective and the non-convective acceleration that correspond to the first and second term on the right-hand side of equation (3.22), respectively. The convective acceleration and the mass conservation equation (3.20) are computed simultaneously, whereby an operator split procedure and a divergence corrector are employed. Inserting equation (3.21) together with the updated velocity field $\tilde{\mathbf{u}}$ in equation (3.18) yields the discrete pressure-Poisson equation:

$$\nabla \cdot \left[\frac{1}{\rho(f^{n+1})} \nabla p^{n+1} \right] = \frac{\nabla \cdot \tilde{\mathbf{u}}}{\delta t}. \quad (3.23)$$

Complemented by homogeneous Neumann conditions or Dirichlet conditions, the pressure-Poisson equation is solved by means of a multigrid equation solver. The computation of the velocity field \mathbf{u}^{n+1} is then finished with equation (3.21).

Due to the explicit time discretization, the time step is limited according to the following three criteria to ensure a stable numerical scheme [52] :

Courant-Friedrichs-Lewy condition:

$$\delta t \leq \frac{\Delta x}{\max\{|u|, |v|, |w|\}} \quad (3.24)$$

Constraint due to surface tension force:

$$\delta t \leq \sqrt{\frac{(\rho_l + \rho_g)(\Delta x)^3}{4\pi\sigma}} \quad (3.25)$$

Constraint due to fluid viscosity:

$$\delta t \leq \frac{(\Delta x)^2}{2\max\{\frac{\eta_L}{\rho_L}, \frac{\eta_L}{\rho_L}\}} \quad (3.26)$$

The constraints due to surface tension force and due to fluid viscosity are constant during a simulation. Noticing equation (3.24), the time step in simulations can be dynamically controlled by limiting the maximum allowable Courant-number:

$$C = \frac{\max\{|u|, |v|, |w|\} \cdot \delta t}{\Delta x}. \quad (3.27)$$

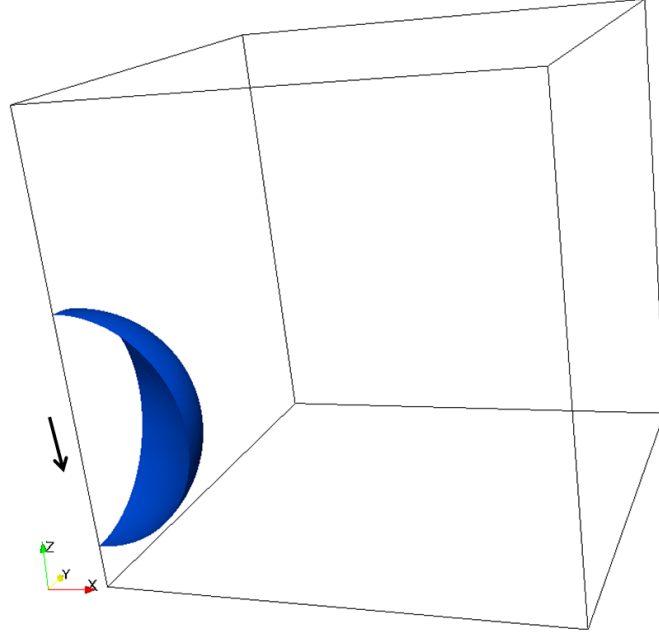


Figure 3.4.: Typical setup for head-on collisions of two identical droplets by means of three symmetry planes.

3.5 Typical setup for head-on collisions of two identical droplets

The typical setup for head-on collisions of two identical droplets, which are the main object of this study, is described in this section. The simulation is initialized with a quarter of a droplet lying on two symmetry planes. The droplet collides with an initial velocity towards a symmetry plane, which is equivalent to the head-on collision of two identical droplets, see Figure 3.4. The cuboidal domain is decomposed into equidistant cuboidal cells. On the symmetry planes the slip conditions are prescribed; the homogeneous Neumann boundary conditions for the velocity and zero pressure are prescribed on all the other boundary planes (outer boundaries).

The setup described in this section serves as a template, from which the setups of almost all of the simulations conducted in this work are derived.

3.6 Computation of the energy contributions

For an isolated fluid system without gravity, the total amount of the kinetic energy K_E plus the surface energy S_E is decreasing with the dissipation rate Φ_E . The different contributions can be calculated based on the local flow field. The local kinetic energy in a computational cell is given as

$$k_e = \int_{\text{Cell}} \frac{1}{2} \rho \|\mathbf{u}\|^2 dV \approx \frac{1}{2} \rho \overline{\|\mathbf{u}\|^2} \Delta x \Delta y \Delta z, \quad (3.28)$$

where the averaged square of the absolute value of the velocity is computed on the basis of assuming a linear velocity profile within a cell, which ensures a second order accuracy. The local kinetic energy is then given as

$$k_e = \frac{1}{6} \rho (u_{i-\frac{1}{2},j,k}^2 + u_{i+\frac{1}{2},j,k}^2 + u_{i-\frac{1}{2},j,k} \cdot u_{i+\frac{1}{2},j,k} + v_{i,j-\frac{1}{2},k}^2 + v_{i,j+\frac{1}{2},k}^2 + v_{i,j-\frac{1}{2},k} \cdot v_{i,j+\frac{1}{2},k} + w_{i,j,k-\frac{1}{2}}^2 + w_{i,j,k+\frac{1}{2}}^2 + w_{i,j,k-\frac{1}{2}} \cdot w_{i,j,k+\frac{1}{2}}) \Delta x \Delta y \Delta z, \quad (3.29)$$

where i, j and k denote the index of cells and $\pm \frac{1}{2}$ denote the cell faces. A graphic example for the notations is found in Figure 3.6.

The surface energy within a cell is given as

$$s_e = \sigma A = \sigma \int_{\text{Cell}} \|\nabla f\| dV \approx \sigma \|\nabla f\| \Delta x \Delta y \Delta z, \quad (3.30)$$

where A is the surface area of the interface. ∇f is computed by means of a 27 cells stencil, as it is described in section 3.2. The values of k_e and s_e are summed up over all the computational cells to obtain K_E and S_E , respectively.

Alternatively, the interface area can also be computed by adding the areas of all PLIC-surfaces. Rieber [51] states that computing the surface area by means of summing $\|\nabla f\|$ (as suggested in equation (3.30)) is a better choice, because it corresponds closely to the discretization of the surface tension force. This statement is verified through a simulation, whereby a quarter of a droplet lying at the intersection of three symmetry planes is initialized with an initial velocity. After dissipation of the kinetic energy, the droplet is expected to retain its original form, i.e. original surface area. The comparison between the surface area evolutions computed by means of the two above mentioned methods does support the statement made by Rieber [51]; see Figure 3.5. However, the deviation between the two profiles shown in Figure 3.5 is not very large, especially when the oscillation is still relatively strong.

The dissipation rate for a cell is given as

$$\phi_e = 2\eta \int_{\text{Cell}} \mathbf{D} : \mathbf{D} dV \approx 2\eta \mathbf{D} : \mathbf{D} \Delta x \Delta y \Delta z, \quad (3.31)$$

where $\mathbf{D} = \frac{1}{2}(\nabla \mathbf{u} + \nabla \mathbf{u}^T)$ is the deformation tensor of the flow field. The scalar product $\mathbf{A} : \mathbf{B}$ between tensors is defined as $\mathbf{A} : \mathbf{B} = \sum_{i,j} a_{i,j} b_{i,j}$. For computing the local energy dissipation, the velocity gradients have to be evaluated. Taking the velocity component u as an example, the velocity gradients are given using central differencing:

$$\frac{\partial u}{\partial x} = \frac{u_{i+\frac{1}{2},j,k} - u_{i-\frac{1}{2},j,k}}{\Delta x}, \quad (3.32)$$

$$\frac{\partial u}{\partial y} = \frac{u_{i-\frac{1}{2},j+1,k} + u_{i+\frac{1}{2},j+1,k} - u_{i-\frac{1}{2},j-1,k} - u_{i+\frac{1}{2},j-1,k}}{4\Delta y}, \quad (3.33)$$

$$\frac{\partial u}{\partial z} = \frac{u_{i-\frac{1}{2},j,k+1} + u_{i+\frac{1}{2},j,k+1} - u_{i-\frac{1}{2},j,k-1} - u_{i+\frac{1}{2},j,k-1}}{4\Delta z}. \quad (3.34)$$

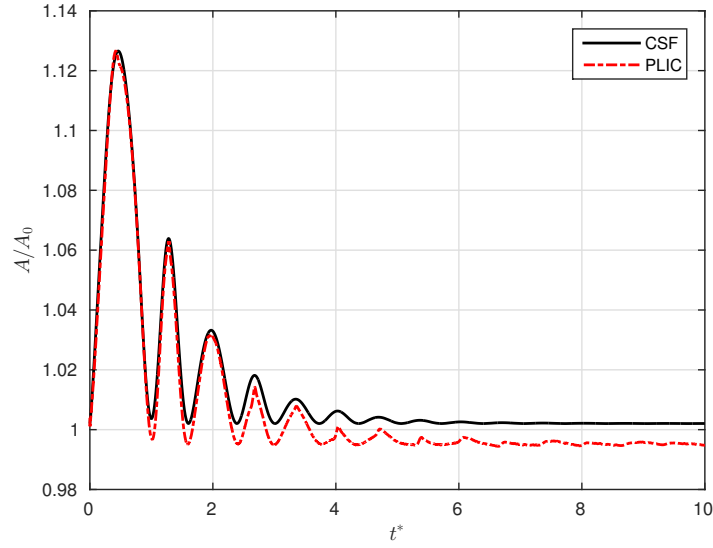


Figure 3.5.: Comparison between the surface area evolutions computed by means of $\|\nabla f\|$ (denoted in the Figure by CSF due to their similar discretization) and PLIC-surfaces. The balanced-CSF model is employed in the simulation. The surface area is normalized by the original surface area given analytically. The time is normalized by the time when the droplet finishes the first oscillation in the sense that the solid line reaches its minimum. The setup of the simulation is listed in Table C.1 in appendix C.

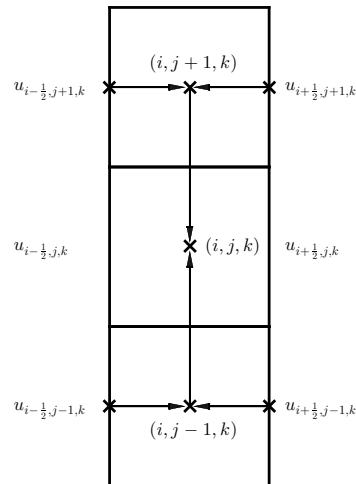


Figure 3.6.: Computation of $\frac{\partial u}{\partial y}$ by means of a 3 cells stencil. The velocities are interpolated from cell faces to the cell centers. The differencing is then conducted over $2\Delta y$.

It should be noted that the computation of $\frac{\partial u}{\partial y}$ and $\frac{\partial u}{\partial z}$ is conducted in a 3 cells stencil, see the schematic illustration in Figure 3.6. The dissipated energy can be computed by summing the local dissipation rate over all cells and integrating the obtained total dissipation rate Φ_E over time.

4 Lamella Stabilization

In direct numerical simulations of binary droplet collisions using the VOF method, a fluid lamella arises and ruptures during a droplet collision process under certain conditions, which leads to an unphysical topology change and thus strong deviation of the collision complex shape in the successive deformation process. This Lamella can be a liquid lamella in droplet collisions at high Weber numbers ($We > 100$) and a gas lamella (the gas lamella is also referred to as the gas layer or gas film in this thesis) in droplet collisions at low Weber numbers ($We = O(1) \sim O(10)$), the context of which will be described in detail in this chapter.

4.1 Stabilization of a liquid lamella

Head-on collisions of two identical droplets at high Weber numbers lead to the formation of an extremely thin liquid lamella, which artificially ruptures in numerical simulations even at relatively fine grid resolutions. The rupture of the thin lamella leads to a deviation of the collision complex shape as illustrated exemplarily by Figure 4.1. Similar lamella ruptures are also noted in many other numerical works [41, 37, 17, 16]. In experimental studies of binary droplet collisions, this kind of lamella rupture is not observed even when the Weber number is increased to $We = 2876$ [56], which confirms that the mentioned rupture of a liquid lamella is artificial and must be prevented in numerical studies for capturing sound physics.

According to the work of Focke and Bothe [17] and Focke [16] in particular, the interaction while computing the surface tension forces of both sides of the liquid lamella leads to the artificial lamella rupture. With respect to the CSS model in FS3D, the surface tension force is computed from the divergence of the surface stress tensor, which is computed from a smoothed volume fraction field \tilde{f} . Both the smoothing of the volume fraction and the calculation of the divergence of the surface stress tensor are carried out in stencils of 27 cells (3^3 cells). Altogether the surface tension force in each cell containing a surface is affected by volume fractions in a stencil of 125 cells (5^3 cells) [17]. When the lamella is resolved by fewer than four cells, the

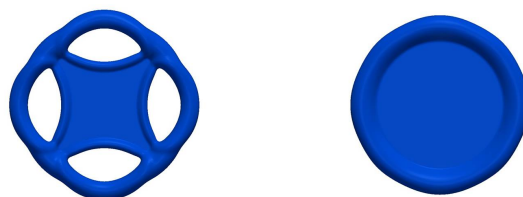


Figure 4.1.: Lamella rupture (left) vs. stabilized lamella (right). Reproduced from [30] with permission.

block of 125 cells contains interface cells from the opposite side of the lamella, which causes an unphysical interaction that leads to the lamella rupture.

In addition, the surface reconstruction is affected by the artificial interface interaction as well. The surface reconstruction is unambiguously determined by the f -field and the surface normal computed by equation (3.5). The computation of the surface normal is conducted in a stencil of 27 cells. If this contains additional interface cells from the opposite side of the lamella, the computation of the surface normal is affected and, hence, the surface reconstruction as well.

Both the problem in computing the surface tension force and the problem with the surface reconstruction can be prevented by identifying the lamella region and then treating the cells of the opposite side of the lamella as ‘fully wetted’. Focke and Bothe [17] implemented the lamella stabilization method for head-on collisions of two identical droplets based on the collision of a droplet on a symmetry plane, which is equivalent to the head-on droplet collision. The boundary conditions of a symmetry plane are incorporated using two layers of dummy cells adjacent to the computational domain [7]. Focke and Bothe [17] sort out the lamella region from the rim region of the collision complex by detecting the direct neighboring cells of an interface cell (we denote it here as a ‘target’ cell) in the first layer of the computational grid on the symmetry plane. If not every direct neighboring cell contains liquid, the target cell is defined as ‘rim’. Target cells whose neighboring cells are all also interface cells, are defined as ‘lamella’. The volume fraction is then set to $f = 1$ in the dummy cells in the lamella region, thereby avoiding the above-mentioned unphysical interaction. It turns out that, in this way, the lamella is well stabilized. However, the rim region is not optimally identified since only the direct neighboring cells of a target cell are detected, which may lead to the confusion of the rim region with the lamella region.

In order to correctly identify the rim region, some modifications are introduced to the work of Focke and Bothe [17]. The implementation of this modified lamella stabilization method is based on a collision complex on a symmetry plane as well. The procedure is as follows (see Figure 4.2 for a schematic diagram):

1. The region is denoted as ‘empty’ if the volume fraction in the first layer of computational cells of this region equals 0 ($f(i, j, 1) = 0$). The region is denoted as ‘full’ if the volume fraction in both the first and second layer equals 1 ($f(i, j, 1) = 1$ and $f(i, j, 2) = 1$).
2. The algorithm detects all the neighboring cells of the remaining cells in the first layer as follows: if one of the volume fractions $f(i+3, j, 1), f(i+3, j+3, 1), f(i, j+3, 1), f(i-3, j+3, 1), f(i-3, j, 1), f(i-3, j-3, 1), f(i, j-3, 1), f(i+3, j-3, 1)$ equals 0, the region is denoted as ‘rim’; the remaining region is set to ‘lamella’. The detection distance ‘3’ is chosen, since it is large enough to avoid the confusion of the rim region with the lamella region addressed above and small enough to avoid reaching the neighboring finger-structures in spatter phenomenon while detecting.
3. The volume fractions of dummy cells in the lamella region are set to 1 and are mirrored in the remaining regions.

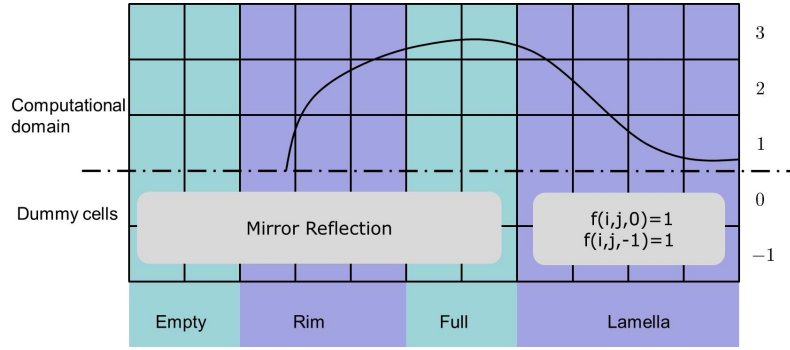


Figure 4.2.: Schematic of lamella stabilization. Reproduced from [30] with permission.

4. The surface tension force, the gradient of f and, hence, the surface normal due to equation (3.5) are computed from this modified f -field.
5. The modification of the f -field in dummy cells is discarded.

To summarize, the stabilization algorithm for the liquid lamella corrects the computation of the surface tension force and the reconstruction of the PLIC-surfaces for the stabilization of the liquid lamella by modifying the f -values in dummy cells temporarily. Meanwhile, the computation of ∇f so as the computation of $\|\nabla f\|$ are also corrected. In addition, the lamella stabilization of Focke and Bothe [17] keeps the f -value in the lamella from falling below 10^{-6} during the transport of the f -field. Focke and Bothe [18] extended the work of Focke and Bothe [17] for simulating off-center droplet collision without a symmetry plane by adding liquid into the lamella to stabilize the lamella. In contrast, no mass needs to be added in the present work in order to keep the lamella from rupturing.

4.1.1 Validation

In order to validate the new implementation of the lamella stabilization, the numerical results are compared with the experimental work of Roth et al. [55]. The fluid is iso-propanol. Figure 4.3 shows that the shapes of the collision complex resulting from the simulation and from the experiment are in good agreement. The slight corrugation at the rim of the collision complex at the later stage of the deformation (around $400\mu s$) is also predicted by the simulation.

The developments of the collision complex diameter D for two cases with different Weber numbers $We = 268$ and $We = 518$ are presented in Figure 4.4. In the simulations, D is defined as the average diameter on the collision plane and is computed based on the barycenter of the PLIC-surfaces; in the experiment, the measurement of D is indicated in the experimental part of Figure 4.3 (denoted there as d). The diameter of the collision complex and the time are presented in a dimensionless form defined by $D^* = D/D_0$ and $t^* = t \cdot U_r/D_0$, respectively. In the case of $We = 268$ (the same case as presented in Figure 4.3), the development of D predicted by the simulation is in very good agreement with the experimental results. In the case of $We = 518$, the curves for the diameter of the collision complex converge with increasing grid resolution. However, the limit curve lies above the corresponding experimental results. This

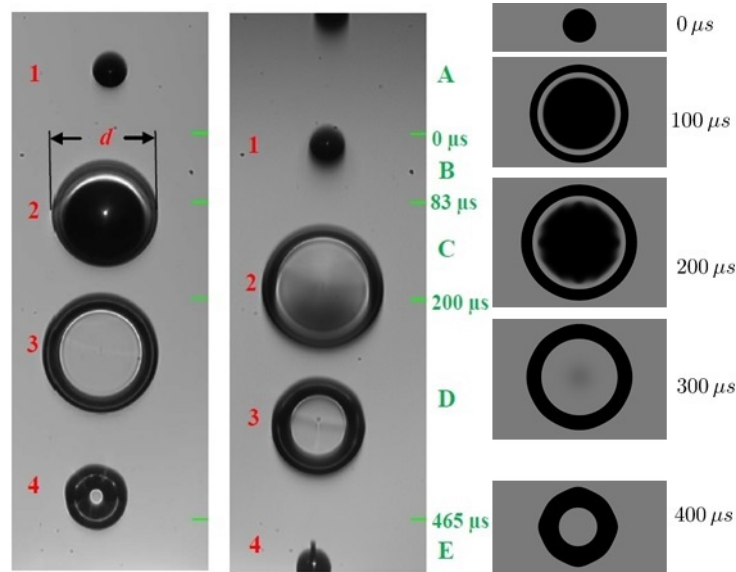


Figure 4.3.: Comparison of the predicted shapes of the collision complex (right) with the experimental results (left) of Roth et al. [55]. The two columns of the collision complexes in the experiment result from double exposure. See Roth et al. [55] for more details about the experimental setups. The Weber number and Reynolds number are $We = 268$, $Re = 426$. The setup of the simulation is listed in Table C.2 in appendix C. Post-processing is done by means of the open source ray tracer program POV-Ray (<http://www.povray.org>). Reproduced from [30] with permission.

deviation is attributed to both the numerical and experimental inaccuracies. In the experiment, errors arise and are accumulated measuring the droplets' material and kinetic parameters. For example, assuming that the velocity in the experiment might be smaller than measured, an additional simulation with a smaller Weber number ($We = 448$, the relative velocity is 7% smaller than the original) is performed, which achieves a very good accordance. In total, these comparisons show the ability of the lamella stabilization method in predicting the development of the collision complex.

4.1.2 Lamella stabilization in terms of the balanced-CSF model

In the lamella region that is not well resolved, as it is exemplarily shown in Figure 4.2, it is not possible to compute the interface curvature in a meaningful way with the algorithm of the balanced-CSF model described in Chapter 3, since neither meaningful height functions nor meaningful fittings can be found. As a result, the surface tension force cannot be computed correctly in the lamella region and the lamella collapses. In order to compute the interface curvature in the lamella region accurately through meaningful height functions, it is necessary to find a full cell and an empty cell in a cell column that aligns with the direction of the maximum component of the surface normal. By using the lamella stabilization algorithm, the absent full cells in the lamella region can be artificially guaranteed for computing accurate interface curvatures and thus the lamella can be stabilized. In spite of its functionality, the balanced-CSF

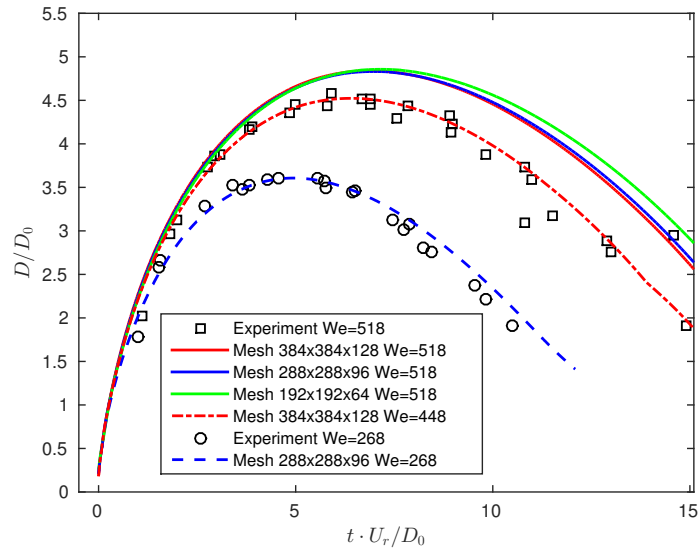


Figure 4.4.: Comparison of the predicted diameter of the collision complex with experimental results. The case $We = 268$ is the same case as presented in Figure 4.3. The Reynolds number of the case $We = 518$ is $Re = 600$. The Reynolds number of the case $We = 448$ is $Re = 558$. The setups of the corresponding simulations are listed in Tables C.2, C.3 and C.4 in appendix C. Reproduced from [30] with permission.

model is not used together with the stabilization algorithm within this thesis, since it cannot deal with the topology change at binary droplet collisions in the contact area. Although it is possible to switch the model for computing the surface tension force after a topology change from the CSS model to the balanced CSF model, the complexity is not compensated because parasitic currents do not play an important role in droplet collisions at high Weber numbers.

4.1.3 Correction of the computation of the surface energy

The lamella stabilization algorithm corrects the computation of $\|\nabla f\|$ for an under-resolved lamella and therefore also corrects the computation of the surface energy in the domain computed by means of summing $\|\nabla f\|$ (CSF-like approach). Nonetheless, one further step of correction has to be taken for a valid computation of the integral surface energy by means of the CSF-like approach, i.e. by equation (3.30). This correction is conducted by extending the region for summing $\|\nabla f\|$ from the domain to the layer of dummy cells adjacent to the symmetry plane based on the fact that the value of $\|\nabla f\|$ is not zero in dummy cells when the lamella is under-resolved, as it is exemplarily shown in Figure 4.5. This correction is only employed in the identified lamella region.

The diagram in Figure 4.6 shows the corrected surface energy evolution of a droplet collision process compared to the uncorrected one. The collision process can be roughly divided into an expanding phase, when the surface energy increases due to the expansion of the collision complex and a receding phase, when the surface energy decreases due to the retraction of the collision complex. At around $t^* = 4$, the deviation between the original result and the corrected

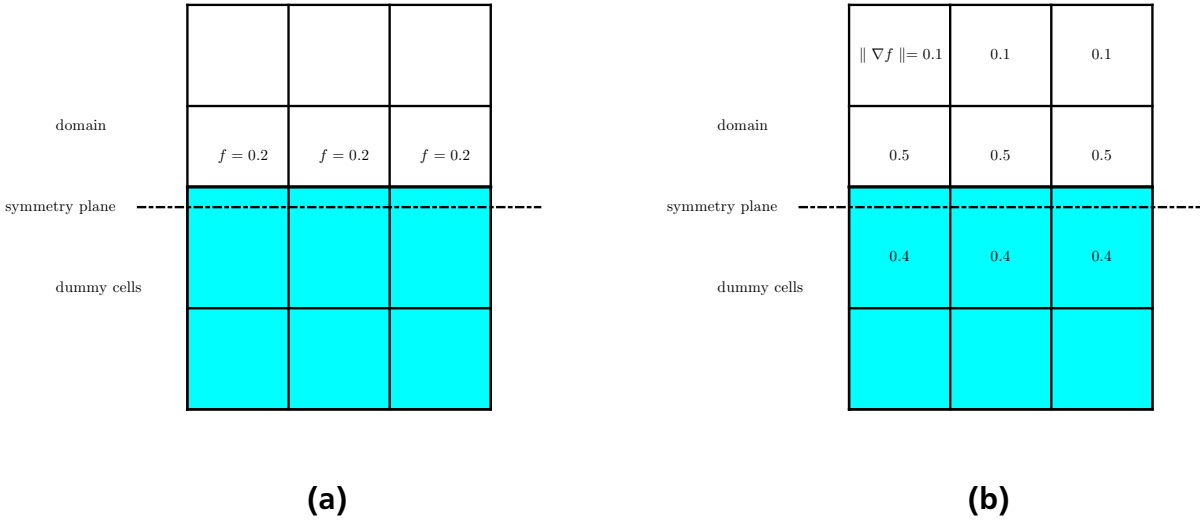


Figure 4.5.: A fragment of an under-resolved lamella which is ideally planar. The volume fractions are constant in tangential direction. The cell width is 1. (a) f -values are set to 1 by the lamella stabilization algorithm in dummy cells. (b) summing $\|\nabla f\|$ in the extended region yields the surface area exactly.

one begins to become more obvious, since the lamella is then increasingly under-resolved. At around $t^* = 14.8$ the deviation vanishes since the lamella vanishes due to the retraction of the collision complex. The curve representing the energy evolution computed by summing the area of the PLIC-surfaces provides an additional evidence for the necessity of correcting the computation of the surface energy conducted by means of summing $\|\nabla f\|$.

4.2 Stabilization of a gas lamella

Similar to the liquid lamella of a collision complex, a gas lamella between two liquid-gas interfaces also ruptures in VOF-simulations conducted with the CSS model as long as the interfaces from both sides of the gas lamella are located in a 5^3 cells stencil due to the artificial interaction while computing the surface tension force. In binary droplet collisions, this kind of gas lamella rupture always leads to coalescence of droplets. We consider two droplets as numerically coalesced if the liquid phase allows to connect the droplet centers without leaving the liquid. In the low Weber number regime ($We = O(1) \sim O(10)$), binary droplet collisions result in either coalescence or bouncing due to the presence of the gas layer between the colliding droplets. In standard VOF simulations conducted with feasible resolutions, the thickness of the gas layer is on the sub-grid scale. Thus, the simulations cannot reproduce bouncing due to the unphysical gas lamella rupture.

Making use of the symmetry plane in the context of head-on binary droplet collisions, the gas lamella can be simply stabilized by setting the volume fractions in dummy cells to zero while computing the surface tension force, as it is schematically shown in Figure 4.7. In this way, the computation of the surface tension force of one droplet is not affected by the other one

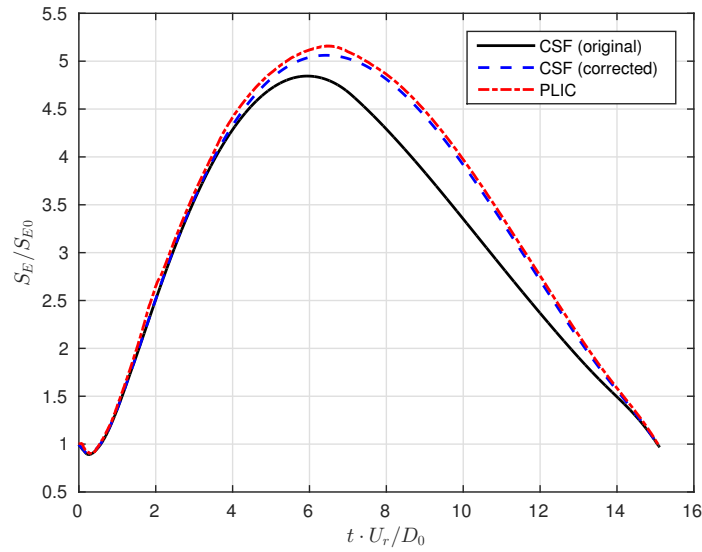


Figure 4.6.: Surface energy evolution computed by means of the CSF-like approach with and without correction and by means of summing the area of the PLIC-surfaces in a binary droplet collision process run with $We = 416$, $Re = 530$. The setup of the simulation is listed in appendix C.5. The surface energy is normalized with the initial surface energy. The time is normalized with D_0/U_r .

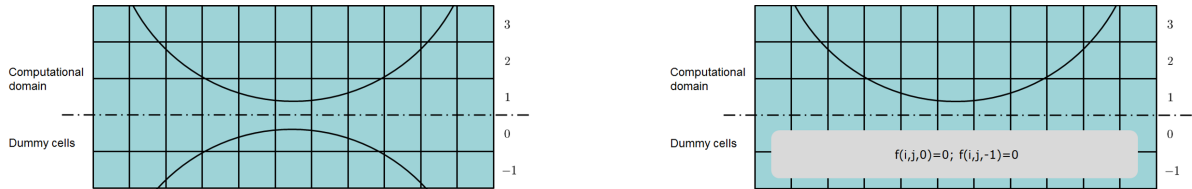


Figure 4.7.: Stabilization of a gas lamella through a modification of volume fraction in dummy cells on the symmetry plane. Left: symmetry condition. Right: stabilization of the gas lamella.

and the gas layer is therefore prevented from rupture. By means of this lamella stabilization algorithm through modification of the boundary condition of the volume fractions, the bouncing phenomenon can be reproduced in simulations. However, the coalescence of droplets is then not possible, since the two droplets do not affect each other at all. In fact, more physics, i.e. the molecular forces as well as the rarefied flow effect have to be involved for modeling the coalescence process, as it is discussed in the introduction. Despite the lack of additional physics in the numerical modeling on the microscopic scale, a prescribed collision outcome ‘bouncing’ or ‘coalescence’ can be simulated by using standard and/or modified boundary conditions of the f -field. The simulation methods and corresponding results are described in the following.

Imposed bouncing

The gas lamella stabilization can be applied to both the CSS model and the balanced-CSF model, in order to impose bouncing. It has been described in Chapter 3.3 that the height function cannot be found in direction perpendicular to the collision plane near the impact in head-on droplet collisions due to the lack of necessary empty cells. This problem is however not present in imposed bouncing, since the the lacking empty cells near the impact can then be found in dummy cells while applying the gas lamella stabilization. In all simulations of imposed bouncing in this work, the balanced CSF model is employed to reduce the parasitic currents that have a prominent effect at low Weber numbers. The comparison between simulation result and experiment conducted by Pan et. al [40] shows that the evolution of the collision complex shapes with the outcome bouncing can be well predicted by the simulation; see Figure 4.8.

Coalescence

In experiments, the coalescence of the colliding droplets (especially in sector III of the collision diagram) does not occur immediately when the droplets are supposed to get in touch (at $t^* = 0$) due to the presence of the gas layer. Instead, the coalescence is delayed to a later time after significant deformation of the droplets. It has been suggested by Pan et al. [40] that the abrupt smoothing of the cuspy contour of the collision complex indicates the occurrence of coalescence. Based on this approach, Pan et al. [40] studied the coalescence process by removing the interface that is modeled by the Front Tracking method at a prescribed time obtained from the experimental observation. In their experimental results shown in Figure 4.9, the coalescence instant is identified to be between $t = 0.366$ ms and $t = 0.370$ ms. Using the interpolated value $t = 0.368$ ms as the time of coalescence, the macroscopic phenomena of the collision process are well reproduced in their simulations. In order to simulate the coalescence phenomenon, the idea of specifying coalescence at a prescribed time is followed. The simulation is started with the balanced-CSF method due to its advantage in reducing the parasitic currents. Meanwhile, the gas lamella is stabilized. At the time of coalescence, the lamella stabilization is discarded by switching the boundary condition of the volume fractions in dummy cells to standard boundary condition at a symmetry plane. Meanwhile, the method for computing the surface tension force is switched to the CSS model due to its ability to deal with the expected topology change causing coalescence. The simulation of coalescence is conducted by using the above-described methods. The comparison with the corresponding experiment yields again very good agreement on the macroscopic scale, as shown in Figure 4.9.

4.2.1 Dependence on the grid resolution

In order to illustrate the dependence of the simulations of bouncing and coalescence on the grid resolution, the evolution of the collision complex diameter defined as the maximum radial extension is plotted in Figure 4.10 for three different resolutions. It is obvious that the results

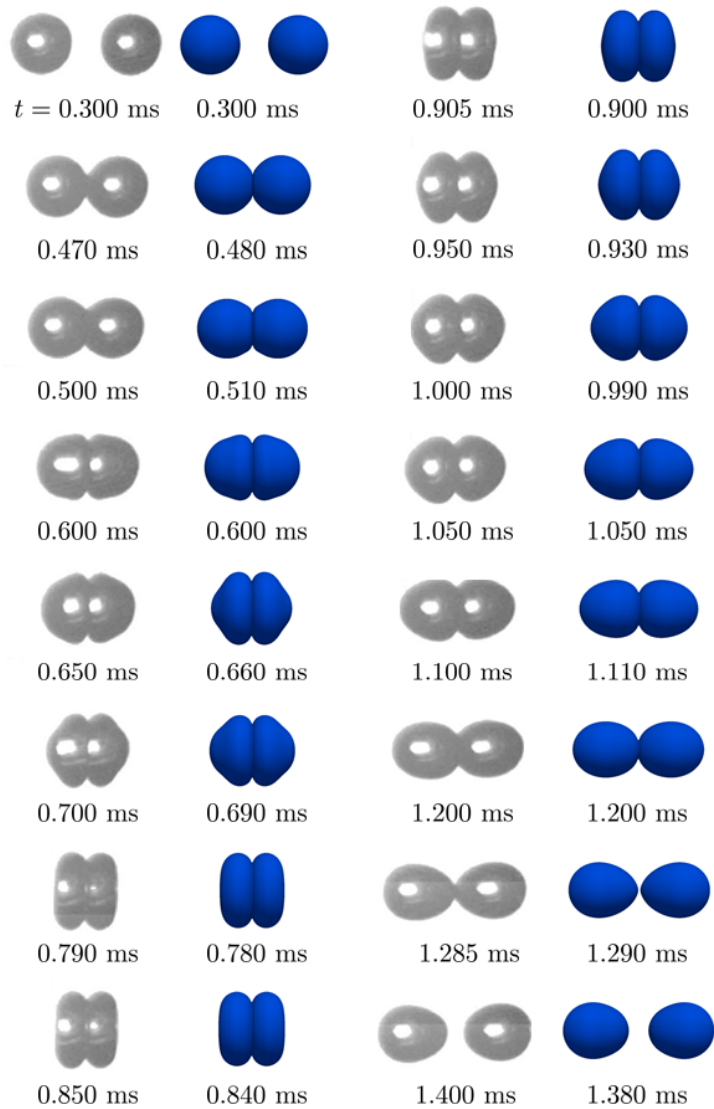


Figure 4.8.: Evolution of collision complex shapes in bouncing phenomenon. Experimental results are obtained from Pan et al. [40]. $We = 9.33$, $Re = 110.36$. The initial droplet diameter is resolved by 64 cells. Detailed numerical setups are listed in Table C.6 in appendix C.

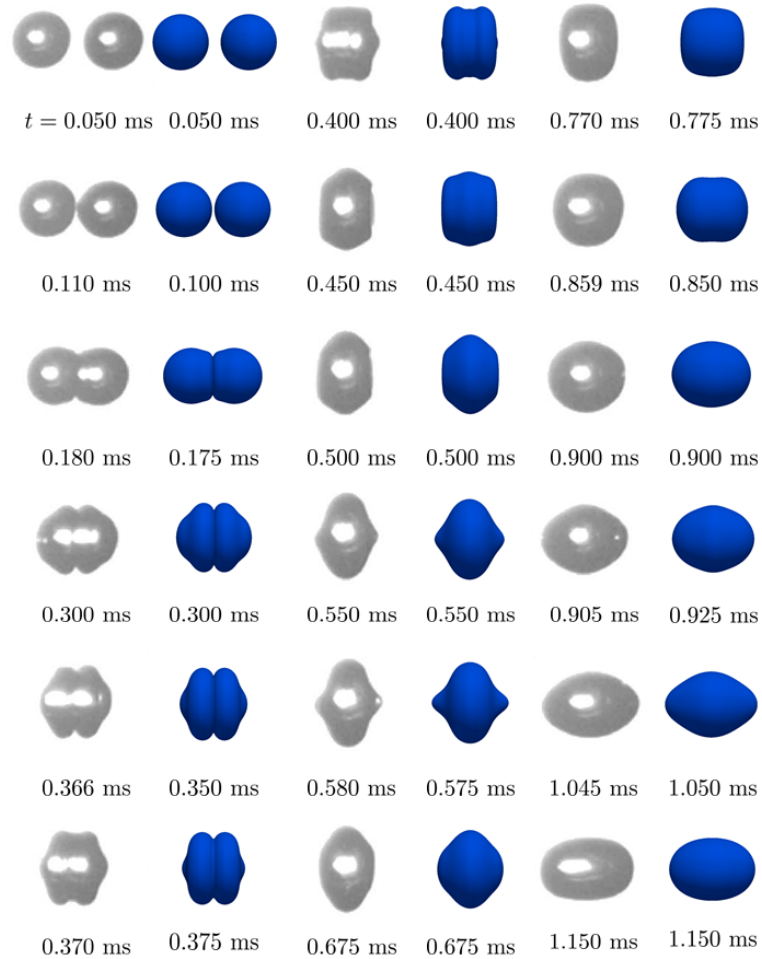


Figure 4.9.: Evolution of collision complex shapes in coalescence phenomenon. Experimental results are obtained from Pan et al. [40]. $We = 13.63$, $Re = 134.24$. The initial droplet diameter is resolved by 64 cells. Detailed numerical setups are listed in Table C.7 in appendix C.

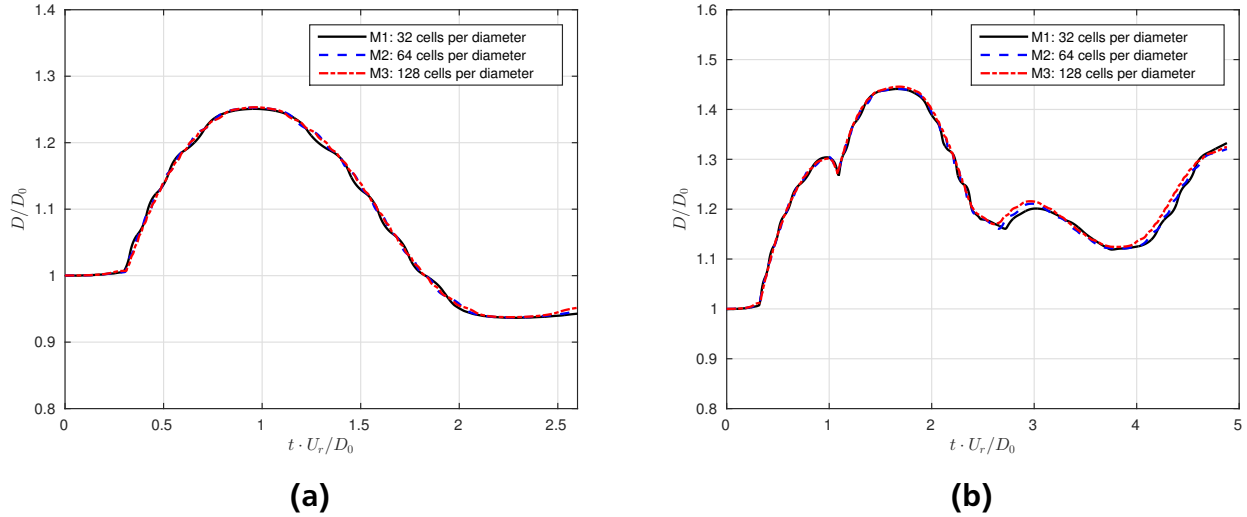


Figure 4.10.: Evolution of the collision complex diameter for three different meshes. (a) Bouncing. (b) Coalescence.

of both bouncing and coalescence are not dependent on the mesh sizes, more precisely, in the macroscopic sense. In the microscopic sense, especially in the sense of the thickness of the entrapped gas layer, however, the deviations of the results obtained from different resolutions are very large, as it is shown in Figure 4.11. This dependence of the gas layer thickness on the grid resolution is not a surprise, because even the finest grid cannot resolve this extremely small length scale. Modeling the flow in the gas layer facilitates more detailed simulation of the collision process. The flow in the gas layer can be modeled by means of a SGS model that will be introduced in Chapter 7.

4.2.2 Correction of the computation of the surface energy with a present under-resolved gas lamella

Reversing the volume fractions in Figure 4.5a, it is easy to perceive that the computation of the surface energy by means of the CSF-like approach also needs to be corrected in case a gas lamella is under-resolved. The correction is exactly the same as in the case of a liquid lamella, namely extending the region for summing $\|\nabla f\|$ to the layer of dummy cells adjacent to the domain, with the precondition that the gas lamella is stabilized. The corrected surface energy evolution of the simulation of bouncing (same case as shown in Figure 4.8) and the uncorrected one are shown in Figure 4.12a. The surface energy computed by means of PLIC-surfaces, also shown in Figure 4.12a, confirms that without a correction, a part of the energy get lost.

In the case of coalescence, the correction of the surface energy computed by means of the CSF-like approach is valid before the coalescence occurs, which is confirmed by the surface energy computed by means of PLIC-surfaces; see Figure 4.12b obtained for the same case as shown in Figure 4.9. Right after the instant of coalescence, the gas lamella stabilization is discarded in order to enable coalescence in the simulation and $\|\nabla f\|$ is then not computed

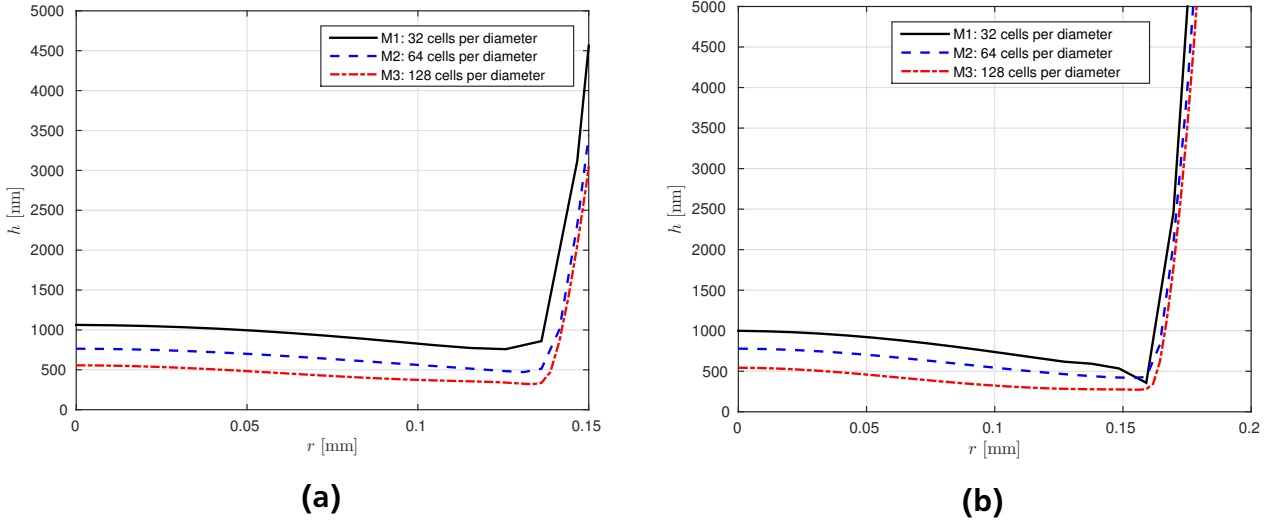


Figure 4.11.: Half of the interface thicknesses computed by means of summing the inversed f -field in cell columns perpendicular to the collision plane. (a) evaluated at $t = 0.84$ ms for the case of bouncing. M1 corresponds to a cell width of $\Delta x = 10.46 \mu\text{m}$ (b) evaluated at $t = 0.368$ ms for the case of coalescence. M1 corresponds to a cell width of $\Delta x = 10.60 \mu\text{m}$.

validly near the symmetry plane, as it is exemplarily shown in Figure 4.13. As a result, a correction of the computation of the surface energy is not possible anymore. The false $\|\nabla f\|$ values in the gas lamella region also result in a sudden drop of the surface energy computed by standard computation. One may have the idea that $\|\nabla f\|$ should still be computed based on the modified f -field in dummy cells. But this is only valid temporarily. The gas film will collapse due to the interaction of the computation of the surface tension force after a short time and the modification of the f -field for the correction of the computation of the surface energy does not make sense anymore. Therefore, the computation of the surface energy after coalescence by means of summing $\|\nabla f\|$ is not valid. As a fallback strategy, the surface energy after coalescence can be computed by means of summing the area of PLIC-surfaces.

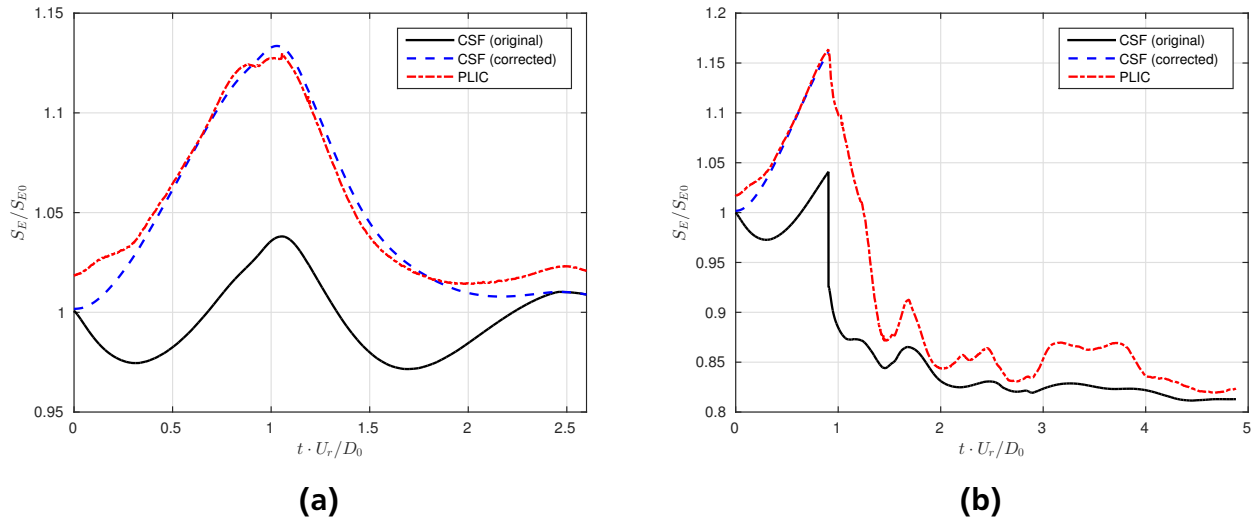


Figure 4.12.: Surface energy evolution computed by means of the CSF-like approach with and without correction and by means of summing the area of PLIC-surfaces. The surface energy is normalized with the initial surface energy. The time is normalized with D_0/U_r . (a) imposed bouncing, conducted with mesh M2. (b) prescribed coalescence, conducted with mesh M2.

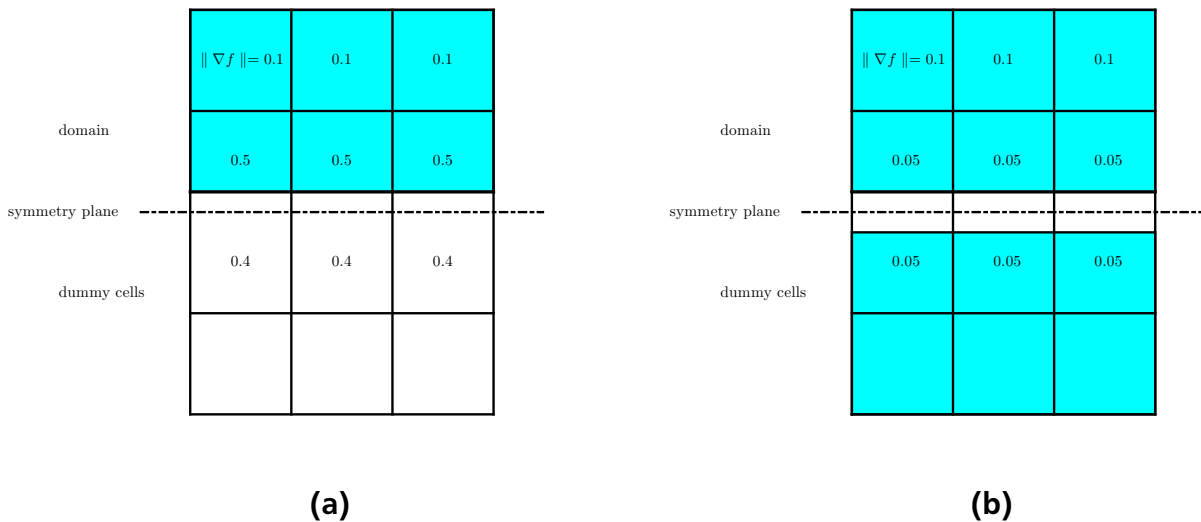


Figure 4.13.: A fragment of an under-resolved lamella which is ideally planar. The volume fractions correspond to the inversed f -values of the example shown in Figure 4.5 and are constant in tangential direction. The cell width is 1. (a) summing the gradients of f in the extended region yields the surface area exactly. (b) Discarding the gas lamella stabilization yields reduced values of $\|\nabla f\|$ in the lamella region. The surface area cannot be computed correctly by means of the CSF-like approach.



5 Numerical Simulations of Spatter Phenomenon and the Mechanism of the Rim Instability

In this chapter, a domain adjustment technique developed for the simulation of the spatter phenomenon is first described. The numerical setups of the simulations and the results of preliminary investigations, which are essential to reach a good agreement between simulations and experiments, are detailed. Next, the simulation results are compared to corresponding experimental work of Pan et al. [39]. Then, the mechanism of the instability growing on the rim of the collision complex, which is called the rim instability for short, is discussed and the effect of the liquid viscosity on the rim instability is studied. In all the simulations in this chapter, the lamella stabilization algorithm is employed for the stabilization of the liquid lamella.

5.1 Domain adjustment

The numerical simulation of binary droplet collisions at high Weber numbers requires a high grid resolution, meaning large computational effort, due to the large deformation of the collision complex. Based on the assumption that the gas phase in the computational domain does not affect the collision dynamics significantly at high Weber numbers, a domain adjustment is employed to reduce the computational effort. This technique is based on the work of Focke [16]. The procedure to implement this technique is described below (see the schematic in Figure 5.1):

1. The computation is started in an initial computational domain.
2. The computation is stopped before the collision complex reaches the boundary of the computational domain. The computational data are saved in restart-files for each CPU.
3. The computational domain is reinitialized by enlarging the domain in the direction in which the collision complex is extending, and shrinking the domain in the direction in which the collision complex is receding.
4. Only the computational data in the overlap region of the old and new computational domains are loaded. The velocities in the non-overlapping domain are set to zero. The relative grid resolution is kept unchanged. Then the computation is restarted without additional modification. Solving the pressure Poisson equation and conducting velocity correction as in a normal time step without domain adjustment ensures a divergence-free velocity field after the domain change.

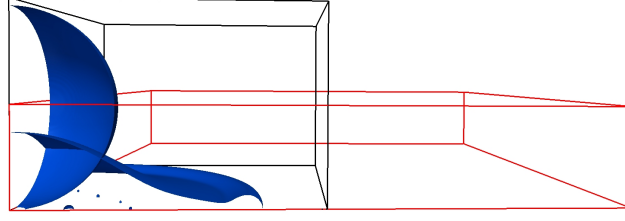


Figure 5.1.: Domain adjustment. Reproduced from [30] with permission.

Using this technique, either the number of necessary CPUs can be reduced or the computational resolution can be enlarged. The surface energy at the time $t^* = 10$ normalized with initial surface energy obtained with and without this domain adjustment technique for the aforementioned case $We = 518$ (Mesh: $384 \times 384 \times 128$) in Chapter 4 is 6.463 and 6.469, respectively. The deviation is very small, which reveals that the domain adjustment technique is usable in the simulation of binary droplet collisions at high Weber numbers.

5.2 Numerical setups for water droplet collisions

In this section, the setups for the simulations of water droplet collisions are detailed, the results of which are compared to experiments in section 5.3.1. The material properties of the air/water system are: $\eta_L = 1.000 \times 10^{-3} \text{ N s/m}^2$, $\rho_L = 1000 \text{ kg/m}^3$, $\eta_G = 1.8 \times 10^{-5} \text{ N s/m}^2$, $\rho_G = 1.2 \text{ kg/m}^3$, $\sigma = 72.0 \times 10^{-3} \text{ N/m}$. In all simulations at least one symmetry plane, namely the collision plane, is used, since the implementation of the lamella stabilization is based on this symmetry plane as described in Chapter 4. In the case of $We = 1520$, owing to the extremely high collision energy, two additional symmetry planes are employed to increase the computational resolution with restricted number of CPUs. The slip conditions are prescribed on the symmetry planes; the homogeneous Neumann boundary condition for the velocity and zero pressure are prescribed on all the other boundary planes. The simulations are started at $t^* = 0$ when the distance between the centers of the initial spherical droplets is D_0 . The parameters of the cases of water droplet collisions which are discussed in this chapter with corresponding setups are summarized in Table 5.1.

The time step is restricted dynamically by the Courant-Friedrichs-Lewy (CFL) condition. The maximum allowed Courant number is set to 0.05 which means:

$$\Delta t \leq \frac{0.05 \Delta x}{|\mathbf{u}_{\max}|}. \quad (5.1)$$

A very small Courant number is selected to ensure a high temporal resolution which avoids oscillation in the velocity field observed at larger Courant numbers. The stability conditions related to the capillary wave and the fluid viscosity are also fulfilled at this small time step.

In all the simulations of droplet collisions a small quantity of air is enclosed in the collision complex. Simulating collision between droplets of high and low viscosity, Focke et al. [19] also

N	We	Re	D_0 (mm)	Initial Domain(mm ³)	Domain Adjustment	Initial Grid
1	442.3	6207.3	1.21	$5 \times 5 \times 1.25$	yes	$512 \times 512 \times 128$
2	805.2	6370.0	0.7	$3 \times 3 \times 0.75$	yes	$512 \times 512 \times 128$
3	1520	8750.0	0.7	$1.5 \times 1.5 \times 0.75$	no	$1024 \times 1024 \times 512$

Table 5.1.: Setups of conducted simulations. Reproduced from [30] with permission.

observed the entrainment of air and argued that the entrainment is attributed to the failure of the interface reconstruction when the approaching interfaces of the colliding droplets appear in one cell. A test simulation replacing the entrainment of air with water has been conducted. The evolution of the collision complex does not show any significant deviation compared to the corresponding results with entrainment of air. Hence, the decision was made to keep the entrainment of air untouched.

5.2.1 Role of imposed disturbances

In order to obtain physically reasonable numerical results in simulating the spatter phenomenon at droplet impact on a fluid film, Rieber et al. [53] imposed an artificial disturbance to the initial velocity field of the droplet and fluid film with a Gaussian distribution. The standard deviation of the Gaussian distribution is selected up to half of the initial velocity of the droplets. Analogously, a random noise is added to the initial velocity field:

$$\mathbf{u} = \mathbf{u}_0 + \tilde{\mathbf{u}}, \quad (5.2)$$

where $\tilde{\mathbf{u}}$ is the added velocity which is distributed over the whole computational domain according to the Gaussian distribution. The standard deviation of the Gaussian distribution for each component of $\tilde{\mathbf{u}}$ is denoted as ΔU , which is normalized with the relative velocity of the colliding droplets U_r . Based on the case of $We = 442.3$, we first examine the influence of the disturbance strength and the time when the disturbance is exerted. The shapes of the collision complex at $t^* = 12.72$ with different ΔU imposed at $t^* = 0$ are presented in Figure 5.2. As expected, the deformation of the collision complex becomes more violent when ΔU is increased. The shapes of the collision complex at $t^* = 12.72$ with $\Delta U = 1\%$ imposed at different times are presented in Figure 5.3. One observes that the deformation of the collision complex which is disturbed very early after the collision ($t^* = 0.1$) is most violent. If the disturbance is exerted after $t^* = 0.1$, the influence of the disturbance tends to vanish with increasing disturbance time, again as to be expected.

All the simulations presented in section 5.3.1 are conducted both with and without disturbances to further investigate the influence of the disturbance on the collision dynamics. The

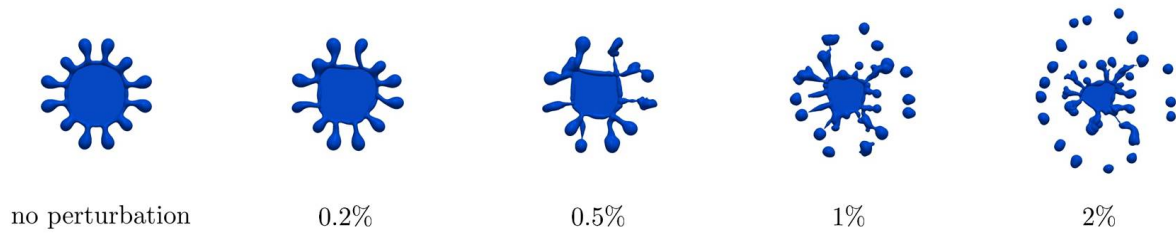


Figure 5.2.: Collision complex at $t^* = 12.72$ resulting from disturbance imposed at $t^* = 0$ with different ΔU . Reproduced from [30] with permission.

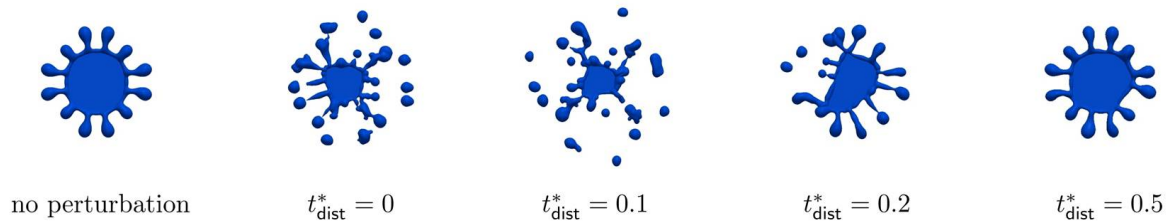


Figure 5.3.: Collision complex at $t^* = 12.72$ resulting from disturbance imposed at different times t_{dist}^* with $\Delta U = 1\%$. Reproduced from [30] with permission.

disturbances are exerted at $t^* = 0$, which corresponds to the reality that at the beginning of the collision an initial disturbance of the colliding droplets and a disturbance of the surroundings exist. The disturbance strength $\Delta U = 1\%$ is selected for the three cases of water droplet collisions that are to be compared to experiments, and also for the simulations conducted with varied droplet viscosities described in section 5.6.

5.3 Simulation results for water droplet collisions and quantification of the rim development

5.3.1 Comparison with experiments

We compare the numerical results with the experimental work of Pan et al. [39]. The comparison of the evolution of the droplet complex for the case of a relatively low Weber number ($We = 442.3$) is presented in Figure 5.4. The deformation history of the droplet complex that results from simulation without an initial disturbance (subfigure b) can be described as follows: A fluid sheet is formed in the middle of the collision complex after the coalescence of the droplets (not shown in the images). This fluid sheet is radially extended within the collision plane and forms a toroidal rim at the edge. At about the maximum diameter of the collision complex ($t^* = 6.23$), an obvious corrugation of the rim is observed. The corrugation is then magnified and evolves to finger-like structures, which grow at the receding stage of the deformation. Compared to the experimental results, the appearance of the corrugation and the evolution of

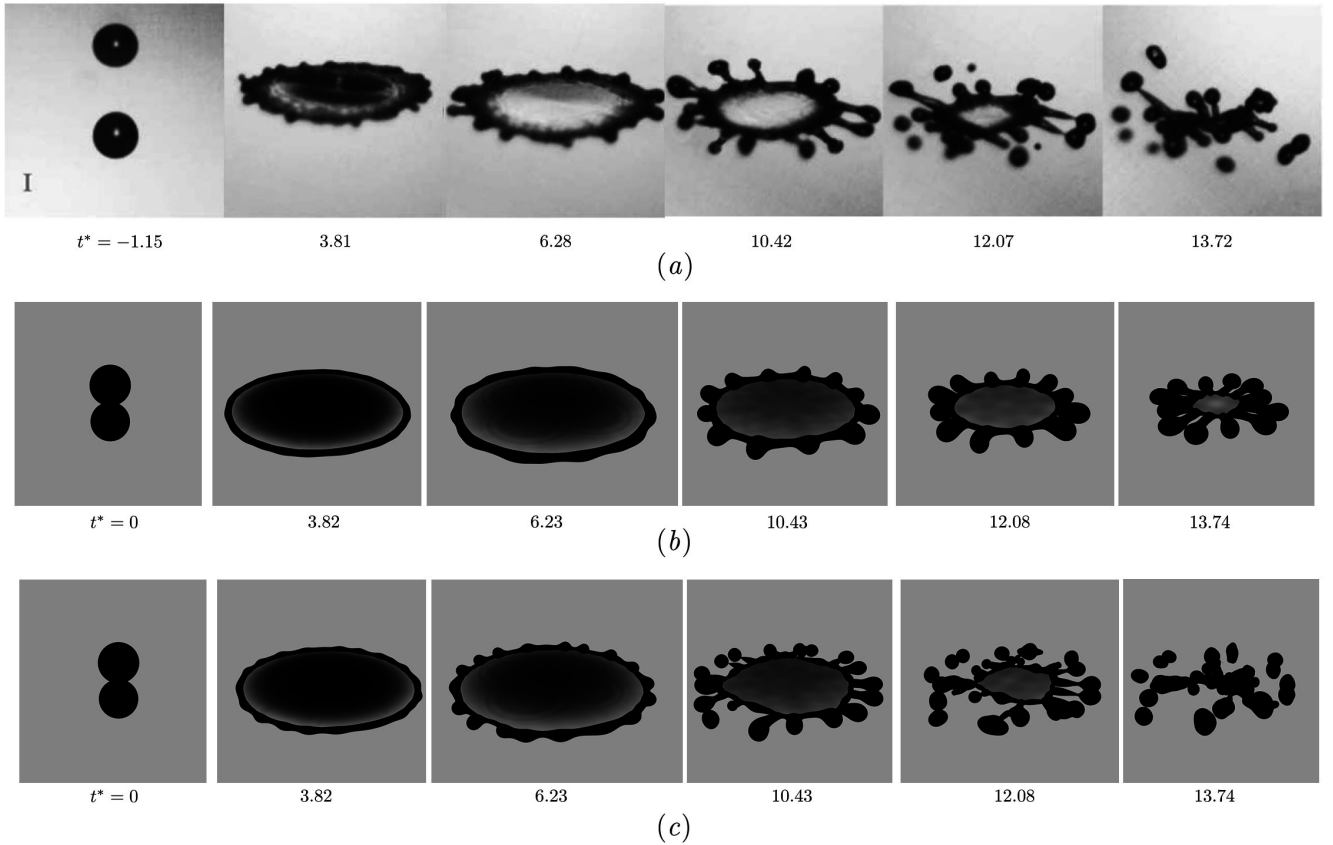


Figure 5.4.: Photographs and visualized simulation results of the head-on collision of water droplets with $We = 442.3$, $Re = 6207.3$. (a) experimental result of Pan et al. [39]. (b) simulation results without initial disturbance. (c) simulation result with an initial disturbance of $\Delta U = 1\%$. The post-processing in the simulations is conducted with POV-Ray (<http://www.povray.org>). Reproduced from [30] with permission.

the fingers are delayed so that no secondary droplets are detached from the rim of the collision complex. The evolution of the collision complex that results from the simulation with an initial disturbance is quite synchronized with the experimental results and yields detachment of secondary droplets, which corresponds well with the experimental results. The development of fingers in the simulation with an initial disturbance is not regular due to the stochastic nature of the Gaussian distribution of the initial disturbance.

Figure 5.5 presents the results for a higher Weber number ($We = 805.2$). In this case the detachment of secondary droplets starts before the maximum diameter is reached in the simulations both with and without an initial white noise. However, even in the simulation without an initial disturbance, the secondary droplets are detached earlier than in the experimental results. A possible explanation for the reason of this deviation will be given in the following section. In the visualizations of the numerical part in Figure 5.5, some secondary droplets at the periphery of the domain are much brighter, since these droplets flying out of the computational domain cannot be correctly captured by used Post-processing program POV-Ray. It should be noted that the grid resolution is not supposed to be the reason of the relatively poor agreement between

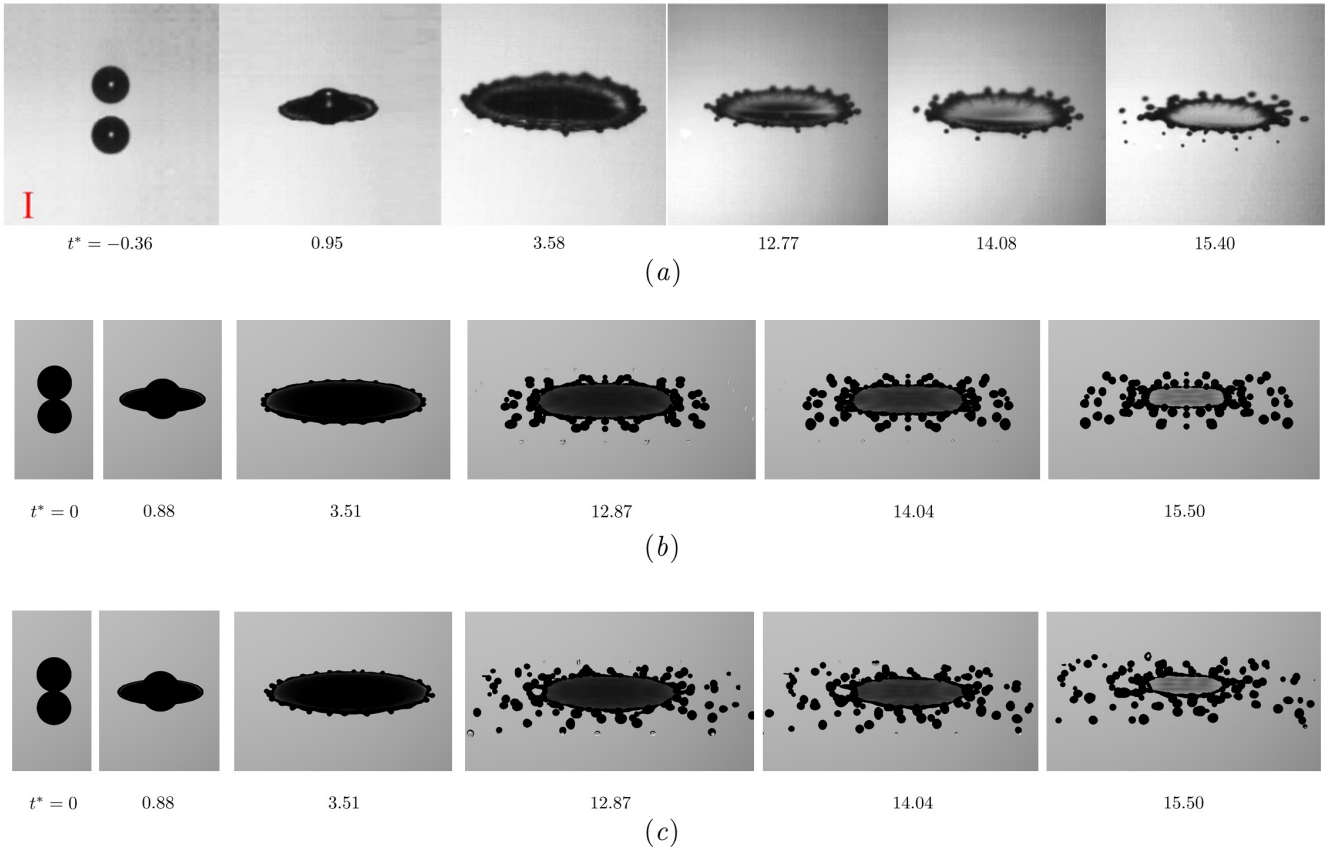


Figure 5.5.: Photographs and visualized simulation results of the head-on collision of water droplets with $We = 805.2$, $Re = 6370$. (a) experimental result of Pan et al. [39]. (b) simulation results without initial disturbance. (c) simulation result with an initial disturbance of $\Delta U = 1\%$. The post-processing in the simulations is conducted with POV-Ray (<http://www.povray.org>). Reproduced from [30] with permission.

the simulations and the experiment in terms of the time when the secondary droplets are splattered. Simulations of the same case with $We = 805.2$ conducted at ITLR of Stuttgart University with doubled grid resolution do not show significant differences; see Figure A.1 in appendix A.

Figure 5.6 presents the results for a much higher Weber number ($We = 1520$). The detachment of secondary droplets from the rim at the very early stage of the deformation called ‘prompt splashing’ [39] is reproduced in the simulation with an initial disturbance (subfigure c), which corresponds well with the experimental results. The results without an initial disturbance (subfigure b) yield no secondary droplets until $t^* = 1.05$. Due to the restriction of the computational resource, the simulation is only conducted until $t^* = 1.05$. Kuan et al. [27] concluded on the basis of their numerical observations that at this extremely high Weber number the whole toroidal rim will be separated from the sheet and will then break up into secondary droplets. In contrast, the simulation results obtained within this work show that the rim is still connected to the sheet and the secondary droplets are splattered out from the rim. Kuan et al. [27] reached their conclusion probably because the lamella was not stabilized, which typically leads to a

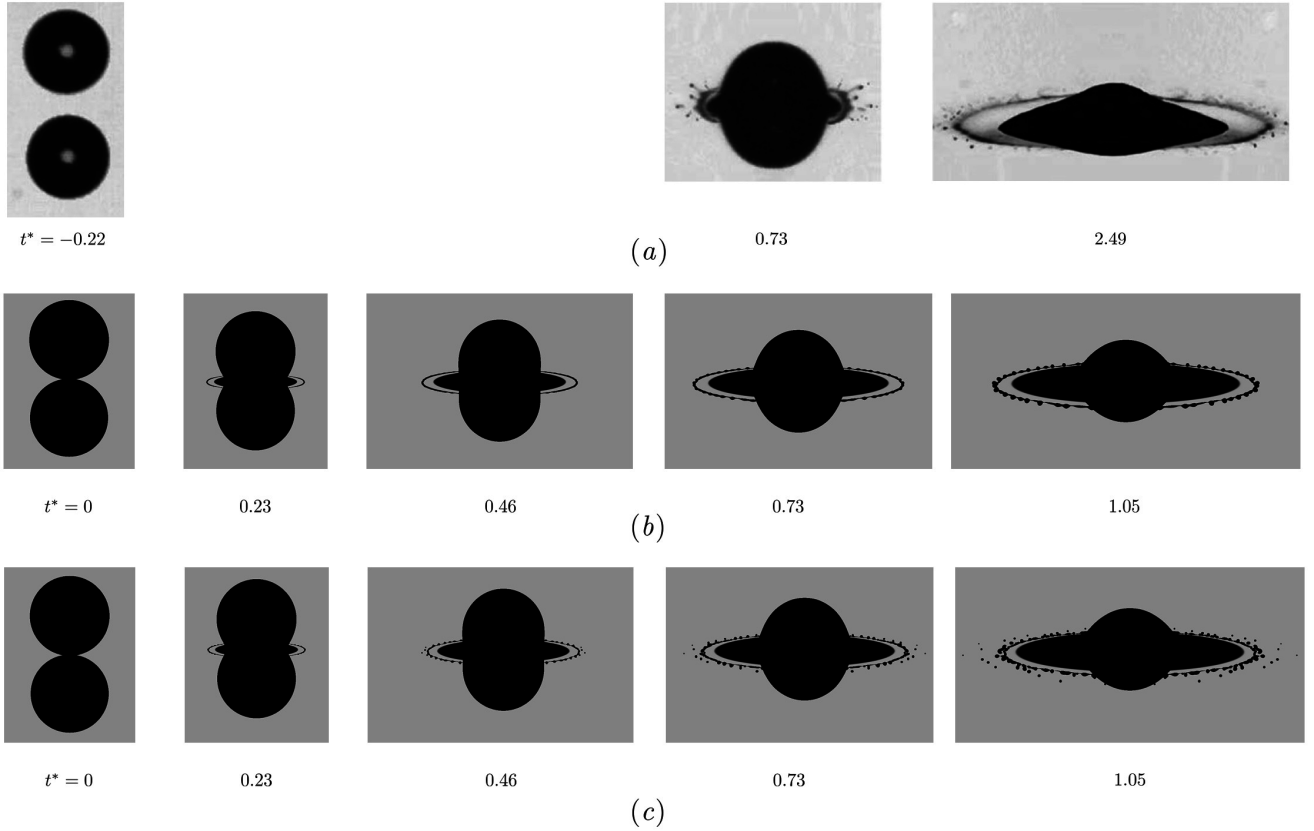


Figure 5.6.: Photographs and visualized simulation results of the head-on collision of water droplets with $We = 1520$, $Re = 8750$. (a) experimental result of Pan et al. [39]. (b) simulation results without initial disturbance. (c) simulation result with an initial disturbance of $\Delta U = 1\%$. The post-processing in the simulations is conducted with POV-Ray (<http://www.povray.org>). Reproduced from [30] with permission.

non-physical lamella rupture at the joint between the lamella and the sheet and therefore the separation of the rim from the sheet.

5.3.2 Quantification of the rim development

A comprehensive quantification of the rim development is conducted for the case $We = 442.3$, which is in best agreement with the experiment. In the following, for simplification, the length is rescaled by the initial droplet radius and the velocity by the initial velocity of one droplet (half the relative droplet velocity). The superscript $*$ that represents the dimensionless time is dropped. We extract the radius of the collision complex on the collision plane based on isosurfaces of $f = 0.5$ and compute the amplitude a_m of instability mode m by conducting Fast-Fourier-Transformation (FFT). The amplitudes and the corresponding curve of the frontier of the collision complex for the case $We = 442.3$ without imposed initial disturbance at $t = 3.82$ are shown in Figure 5.7 (a) and (b). One observes that $m = 4$ dominates the rim instability, which corresponds to the anisotropic Cartesian grid arrangement. Furthermore, all the other strong

peaks correspond to the higher harmonics of the mode $m = 4$. The amplitudes of modes $m = 4n$, on one hand, occur in form of the rim instability. On the other hand, they occur systematically due to the grid structure and, hence, cannot be suppressed. This is a possible explanation why in the case $We = 805.2$ without imposed disturbance, the rim instability is already stronger than in the corresponding experiment.

In order to include the randomness of the disturbance, the same simulation is repeated 10 times with different disturbance of same strength ($\Delta U = 1\%$). Then, the averaged spectral diagrams for the radius of the collision complex are computed. To minimize the unwanted effect of the grid anisotropy and its harmonics (exemplarily shown in Figure 5.7 (c)), the amplitudes of modes $m = 4n$ are replaced by interpolated amplitude values of the neighboring modes (exemplarily shown in Figure 5.7 (d)). The averaged spectral diagrams for a large time span are shown in Figure 5.8. One observes that during the time evolution the region of the largest amplitudes is first shifted to larger modes and then moves slightly backwards.

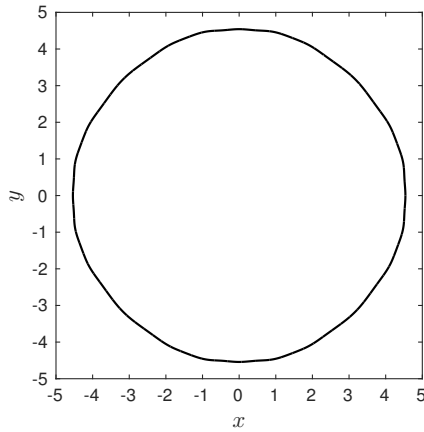
The mean rim radius r_0 is computed based on the case $We = 442.3$ without an initial disturbance and serves as the average value for the corresponding 10 repeated simulations. The rim radius r_0 is computed implicitly, based on the rim volume given as

$$V_{\text{rim}} = 2\pi R_c \pi r_0^2, \quad (5.3)$$

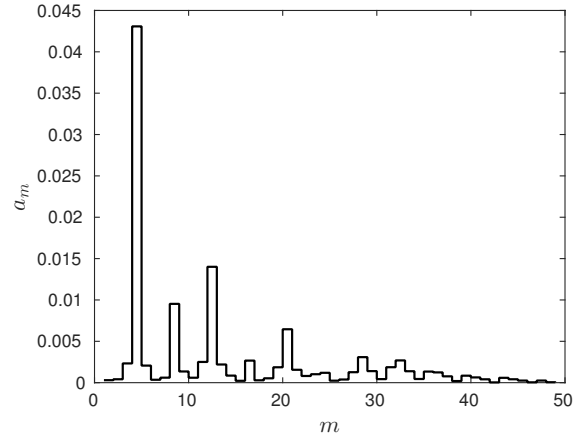
where $V_{\text{rim}} = V_{\text{cell}} \sum_{\text{rim}} f(x, y, z)$. The rim region, over which the summation is computed, is determined from the location of the minimum interface height normal to the collision plane, which always appears adjacent to the rim and separates the rim from the lamella. In (5.3), $R_c = R_0 - r_0$ is the radius of the rim centerline and R_0 is the amplitude of the 0th mode of the FFT analysis. The rim radius is plotted in Figure 5.9. The evolution of the rim radius can be fitted best by a power law according to

$$r_0 = 0.073 t^{0.569}. \quad (5.4)$$

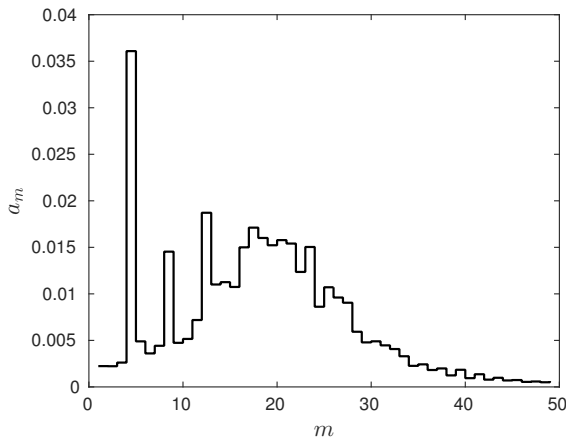
The radius of the collision complex on the collision plane $R(t)$, the rim velocity $\dot{R}(t)$ and rim acceleration $\ddot{R}(t)$ are also computed for the case $We = 442.3$ without an initial disturbance: $R(t)$ is computed as the average value of PLIC-surface center positions; $\dot{R}(t)$ and $\ddot{R}(t)$ are then derived from $R(t)$ by forward differencing. While computing the time difference, $R(t)$ and $\dot{R}(t)$ are locally smoothed by least-squares fitting to eliminate high-frequency oscillations. The evolution of $R(t)$, $\dot{R}(t)$ and $\ddot{R}(t)$ and the corresponding smoothed lines are shown in Figure 5.10. The curves start at $t = 0.01$ to avoid the singularity at $t = 0$. Surprisingly, one observes an oscillation in the development of the rim acceleration, and the acceleration is even positive for quite a long period, which is in contradiction to the common opinion that the rim only decelerates [26]. The acceleration field computed by means of DNS, shown exemplarily in Figure 5.10 (d) for $t = 0.07$, confirms that the frontier of the collision complex on the collision plane is located in the region of positive acceleration. According to Kim et al. [26], the rim is decelerated due to its radial expansion. In the specific case of binary droplet collisions at early time, the surface force pulls the interface outwards on the collision plane (see Figure 5.10



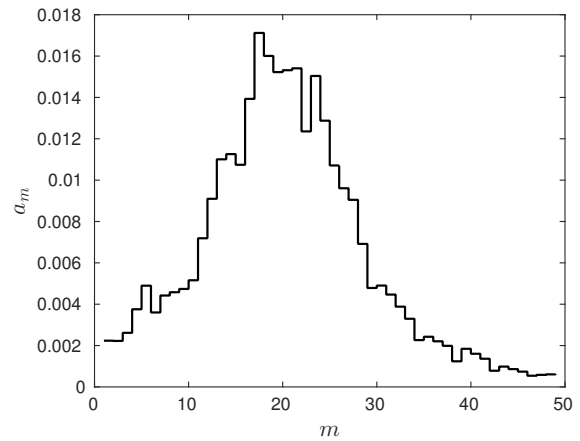
(a)



(b)

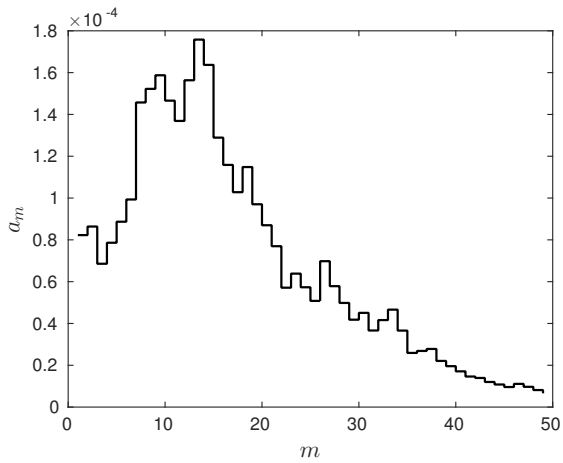


(c)

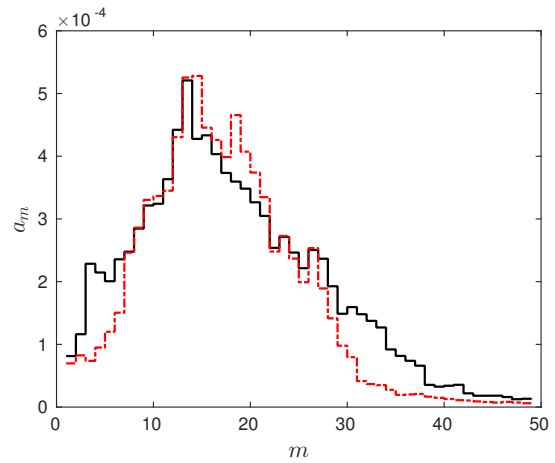


(d)

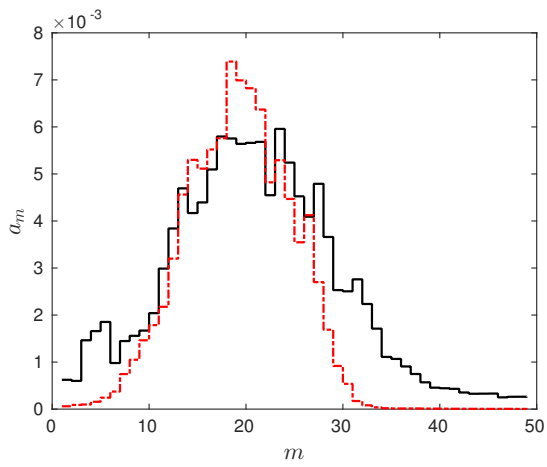
Figure 5.7.: (a) Extracted curve of the frontier of the collision complex on the collision plane for the case $We = 442.3$ without imposed noise at $t = 3.82$. (b) Corresponding amplitudes. (c) Averaged amplitudes of 10 repeated simulations with imposed disturbance of the same strength ($\Delta U = 1\%$) also at $t = 3.82$. (d) The amplitudes of modes $m = 4n$ in (c) are replaced with interpolated values of the neighboring modes. Reproduced from [30] with permission.



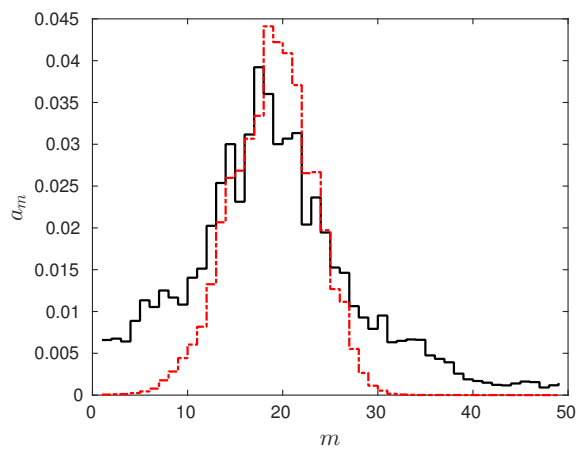
(a) $t = 0.25$



(b) $t = 0.64$



(c) $t = 2.54$



(d) $t = 5.09$

Figure 5.8.: Averaged amplitudes of 10 numerical experiments (black solid line) and amplitudes predicted by PR theory (red dot-dash line). Reproduced from [30] with permission.

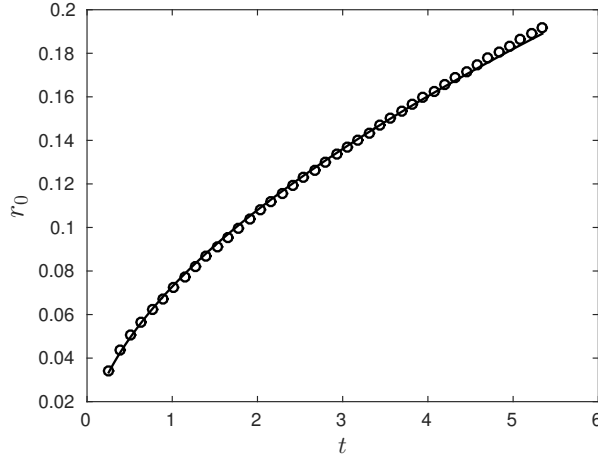


Figure 5.9.: Evolution of the rim radius and its best fitting power-law curve. Reproduced from [30] with permission.

(d) for the local geometry) after droplets coalescence and before the fluid sheet is ejected on the collision plane. This force contributes to the positive acceleration. After the toroidal rim is formed, it oscillates essentially like an oscillating fluid cylinder. According to Rayleigh [47], the angular frequency of a fluid cylinder for mode m can be estimated as

$$\omega_m = \sqrt{(m^3 - m) \frac{\sigma}{\rho r_0^3}}. \quad (5.5)$$

From Figure 5.10 (c), the oscillation period is extracted as the time difference between the first two minima, resulting in a value of 0.147. Applying equation (5.5), the corresponding calculated oscillation period for mode $m = 2$ is 0.145. This very good agreement of the oscillation period confirms that the rim oscillates and that this oscillation is governed by equation (5.5).

5.4 Division of the collision process

In binary droplet collisions at high Weber numbers, the rim of the collision complex is unstable. It grows and forms finger-like structures and, finally, possibly ejects secondary droplets. Based on the quantifications and analysis described in the above section, we can consider the whole unstable collision process as a system that magnifies an initial signal, which is a white noise signal in the simulations. In the conducted simulations, it is assumed that 10 simulations with different initial disturbances of the same strength are enough to compensate the randomness in individual simulations. This system can be roughly subdivided into three sequential connected subsystems corresponding to three phases in terms of the geometrical characteristics of the rim; see also the schematic illustration in Figure 5.11:

- Initial phase (Subsystem I): the period between the contact of the droplets and the emerging of the toroidal rim. This subsystem magnifies an initial signal, which outcome is then transmitted to subsystem II.

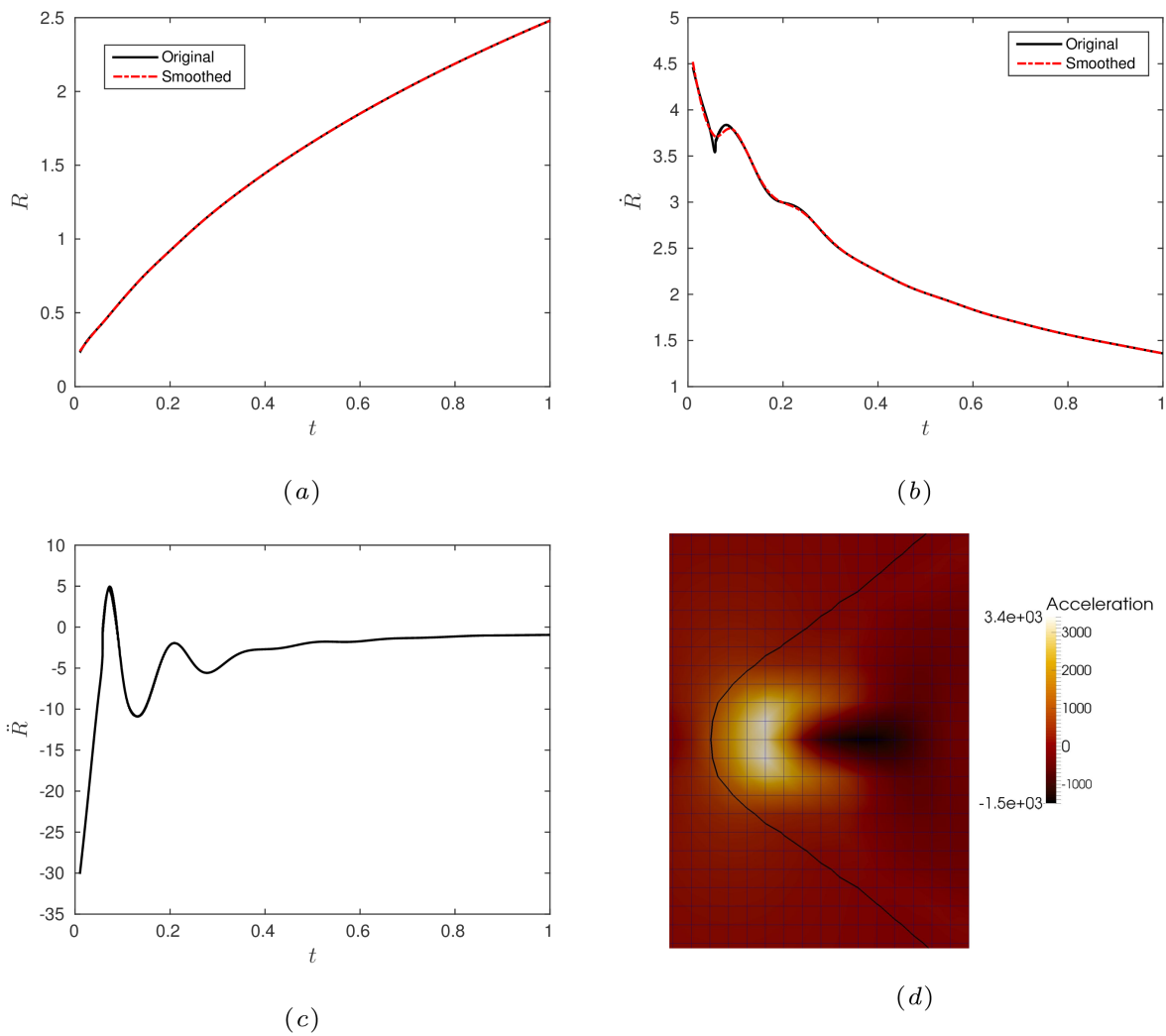


Figure 5.10.: (a) Evolution of the radius of the collision complex. (b) Evolution of the rim velocity. (c) Evolution of the rim acceleration. (d) Acceleration field by means of DNS at $t = 0.07$; the symmetry plane corresponds to the collision plane. The interface represented by the black curve separates the liquid phase on the left from the gas phase on the right. Reproduced from [30] with permission.

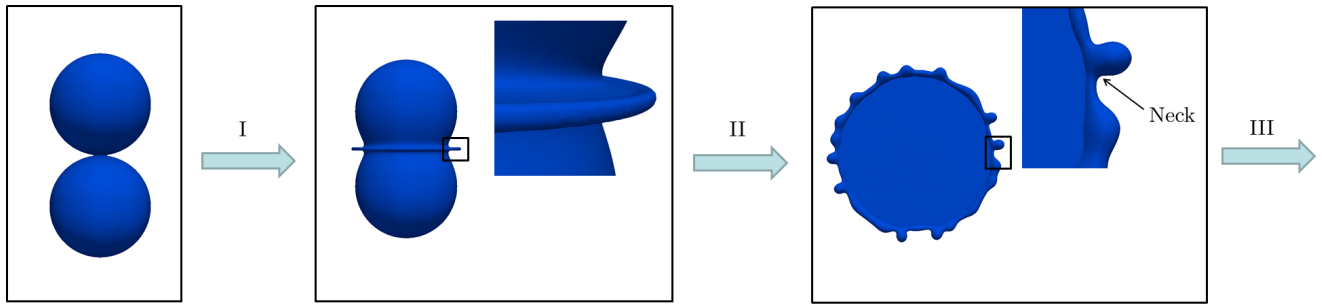


Figure 5.11.: Subdivision of the collision process into three sequential connected signal amplification systems (indicated as I, II and III) based on the geometrical characteristics of the rim.

- Linear phase (Subsystem II): In this period, a toroidal rim forms and gradually grows to fingers. This period ends when a neck forms on the finger. The signals in the initial and linear phase can be characterized by the FFT analysis presented in the previous section.
- Nonlinear phase (Subsystem III): This period begins with the formation of the neck and continues to the end of the collision process. The signal magnified by the subsystem II is further magnified, resulting in fingering and possible detachment of secondary droplets. In this phase, the outcome can be characterized by the number of fingers and the size spectrum of the secondary droplets, although a clear quantification is until now not possible due to the complex geometry and topology of the collision complex in this phase.

In the numerical simulations, the three phases are distinguished according to whether the toroidal rim and the neck on the finger can be identified by the quantification algorithms described in section 5.3.2.

5.5 The rim instability

The ejection of secondary droplets results from the unstable development of the rim of the collision complex formed on the collision plane. Aside from head-on binary droplet collisions, this unstable rim is observed in the impact of a droplet on a solid substrate [34, 29, 64, 54] and the impact of a droplet on a thin film of the same fluid [13, 70]. From previous studies, the reason of the rim instability was mainly explained by: (1) the Plateau-Rayleigh (PR) instability theory in which a cylindrical fluid jet breaks into droplets due to capillary effects [46, 56, 53, 70]; (2) the Rayleigh-Taylor (RT) theory in which the rim corrugation is magnified by the rim deceleration [63, 3, 26, 34]. Which mechanism is the main cause of the rim instability is still under debate. The head-on collision of two identical droplets is the best scenario for studying the rim instability since: (1) compared to the other two mentioned scenarios, the rim is symmetric with respect to the collision plane; (2) the impact of contact angle dynamics is not present. Until now, the rim instability in binary droplet collisions has rarely been studied. In this section, we examine the two mentioned instability patterns based on the quantifications obtained for the case of $We = 442.3$.

The formation of the toroidal rim finishes at around $t = 0.25$, indicating the end of the initial unstable phase. The importance of the RT theory is examined within the initial unstable phase due to the high deceleration of the rim frontier in this phase. The PR instability theory is verified in the linear unstable phase from $t = 0.25$ to $t = 5.09$, when a toroidal rim is present. The instability in the nonlinear phase is discussed based on the pressure field and velocity field later on.

5.5.1 Initial unstable phase: RT instability?

In the classic RT theory [63], a decelerating flat interface that moves in the direction from a dense fluid to a less dense fluid is unstable, as it is described in Chapter 2.2. Kim et al. [26] extended the RT theory for studying the rim instability of a droplet spreading on a solid substrate to cylindrical coordinates. In fact, their model is more suitable for studying the rim instability in binary droplet collisions where the effect of contact angle, which is not included in their model, is not present. The derivation of the model of Kim et al. [26] starts with the spectral decomposition of the radius of the collision complex according to

$$\bar{R}(\phi, t) = R_0(t) + \sum_{m=1}^N a_m(t) \cos(m\phi), \quad (5.6)$$

where ϕ is the angle and a_m the amplitude of mode m . Below, we employ $R(t)$ given in Figure 5.10 instead of $R_0(t)$ since the latter is only computed for certain times by FFT analysis in post-processing. It is not at the disposal for all time steps. The difference between $R(t)$ and $R_0(t)$ is small.

The derivation ends with solving a second-order linear differential equation for the amplitude of mode m [26]:

$$\ddot{a}_m + \alpha(t)\dot{a}_m + \beta(t)a_m = 0, \quad (5.7)$$

where α and β are given as

$$\alpha(t) = 2 \frac{\dot{R}(t)}{R(t)}, \quad (5.8)$$

$$\beta(t) = \frac{(m+1)}{R(t)^3} \left[\frac{m(m-1)}{We} + R(t)^2 \ddot{R}(t) \right]. \quad (5.9)$$

Here We is $1/8$ of the Weber number that is defined for binary droplet collisions. Equation (5.7) is solved numerically by means of a first-order explicit Euler scheme.

We insert $R(t)$, $\dot{R}(t)$ and $\ddot{R}(t)$ into equations (5.8) and (5.9) and evaluate the perturbation growth from $t = 0.13$ to $t = 0.25$, using amplitudes at $t = 0.13$ computed by FFT analysis to serve as initial value $a(0)$. The other initial value $\dot{a}(0)$ is set to 0. The evaluation is not started at an earlier time for two reasons: (1) the FFT analysis at an earlier time was not reliable due to the restriction of grid resolution for small R ; (2) the acceleration at early time is positive

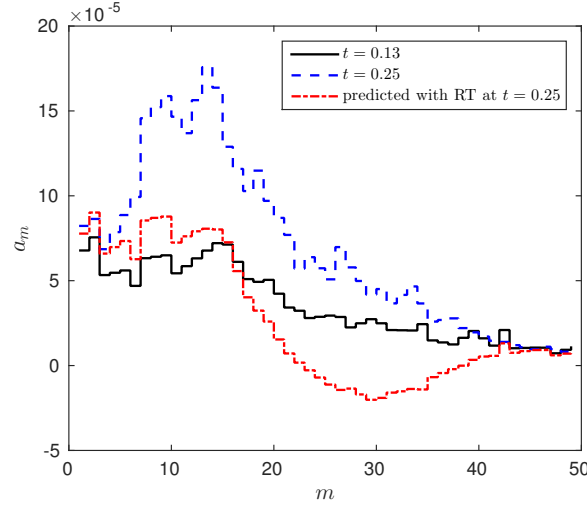


Figure 5.12.: The evolution of amplitudes from $t = 0.13$ to $t = 0.25$ obtained from FFT analysis and the prediction with RT theory. Reproduced from [30] with permission.

over a large time span, which according to RT theory [63] decreases the rim instability. The diagrams in Figure 5.12 show that the amplitudes with small modes are magnified by the rim deceleration, which is in agreement with the FFT analysis. However, the amplitude growth computed by Rayleigh-Taylor theory is rather small compared to the amplitude growth obtained from FFT analysis of the numerical results. Similar statements are also given by Agbaglah and Deegan [1].

5.5.2 Linear unstable phase: PR instability?

The toroidal rim is present between $t = 0.25$ and $t = 5.09$ in all of the 10 conducted simulations, allowing us to examine the PR theory in this linear phase. The same PR expression derived by Zhang et al. [70] is employed for the prediction of the amplitude evolution of mode m . The mathematical model is briefly described below, further details can be found in [70].

The spectral decomposition of the local rim radius is written as

$$r(\phi, t) = r_0(t) + \epsilon(\phi, t) = r_0(t) + \sum_{m=1}^N a_m(t) \cos(m\phi), \quad (5.10)$$

where ϵ is a small perturbation of r_0 . The growth rate S_m of the m^{th} mode is implicitly computed on a cylinder of constant radius via

$$2x^2(x^2 + y^2) \frac{I_1'(x)}{I_0(x)} \left[1 - \frac{2xy}{x^2 + y^2} \frac{I_1(x) I_1'(y)}{I_1(y) I_1'(x)} \right] - x^4 + y^4 = \frac{\rho \sigma r_0}{\eta^2} \frac{x I_1(x)}{I_0(x)} (1 - x^2), \quad (5.11)$$

where $x = k_m r_0$, $k_m = m/R_c$ is the wavenumber of the m^{th} mode, $y^2 = x^2 + \rho S_m r_0^2 / \eta$, and I_n are modified Bessel functions of the first kind. We introduce $\epsilon_m = a_m(t) \cos(m\phi)$. Including the growth and the expansion of the rim, the time evolution of the perturbation is given by

$$\frac{d \ln \epsilon_m(t)}{dt} = -\frac{s}{2} + S_m, \quad (5.12)$$

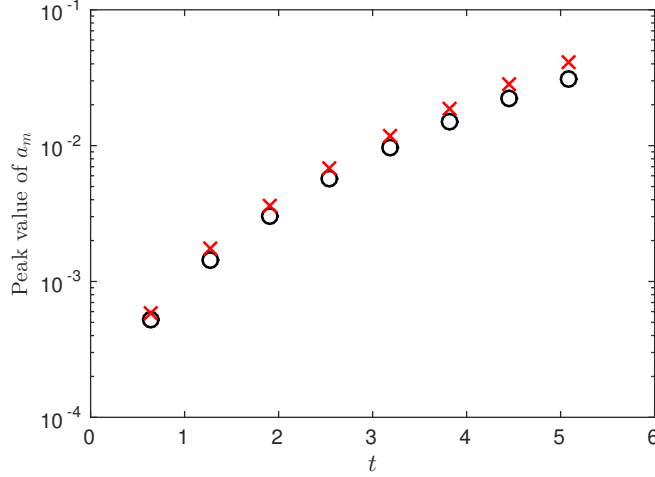


Figure 5.13.: Theoretical maximum amplitude (red cross) and the maximum amplitude in the simulation (black circle) vs time. Reproduced from [30] with permission.

where s is the stretch rate due to the expansion of the rim given by $s = \dot{R}_c/R_c$. Equation (5.12) can then be integrated in time to obtain

$$\ln \frac{\epsilon_m(t)}{\epsilon_m(0)} = -\frac{1}{2} \ln \frac{R_c(t)}{R_c(0)} + \int_0^t S_m dt'. \quad (5.13)$$

Using initial perturbation $a_m(0)$, the amplitude of the m^{th} mode at t is given as

$$a_m(t) = a_m(0) \sqrt{\frac{R_c(0)}{R_c(t)}} \exp\left(\int_0^t S_m(m/R_c(t'), r_0(t')) dt'\right). \quad (5.14)$$

We insert the amplitudes at $t = 0.25$ (shown in Figure 5.8 (a)) as initial conditions in equation (5.14) and compute the amplitude evolution, which is compared with FFT analysis of the numerical results in Figure 5.8. Both the region of the maximum amplitudes and the amplitude scale in this region are predicted very well over quite a long time span, which strongly indicates that the evolution of the rim instability is dominated by the PR instability pattern in the linear phase. The variation of the region of maximum amplitudes is simply due to both the different initial amplitudes of mode m and their different amplification histories.

The theoretical peak amplitude value and the peak amplitude value obtained in the simulations are computed by fitting the corresponding spectral diagram to a Gaussian distribution and compared in Figure 5.13. It turns out that the peak amplitude is somewhat higher in the theoretical prediction. The overestimation factor computed on the basis of data shown in Figure 5.13 is 1.23 ± 0.06 .

5.5.3 The nonlinear unstable phase

A more detailed interface evolution history for the case of $We = 442.3$ with an initial disturbance of $\Delta U = 1\%$ is shown in Figure 5.14. In these images, the phenomena in the nonlinear

unstable phase, i.e. the growth of fingers and the detachment of secondary droplets, are illustrated more clearly. In order to gain more insights into the flow in the collision complex, the pressure field and the velocity field for a truncated area (originally in the black box) of Figure 5.14 are presented in Figure 5.15.

A negative pressure region located at the joint of the sheet and the rim is observed in all of the presented pictures; in the same region the velocity is high. It seems that the fluid is drawn into the rim by the negative pressure region at least at the later stage of the deformation. The velocity fields show that the flow in the circumferential direction occurs only inside the rim (not considering the gas flow).

In the later phase of collision (nonlinear phase regarding the rim instability), it is impossible to predict the strength of the rim instability by means of the PR instability theory as described in section 5.5.2 due to the large deformations. Despite this, instability patterns similar to the PR instability pattern are observed. Comparing the pressure field at $t^* = 5.09$ and at $t^* = 6.36$, the high pressure within the rim fraction between the middle finger and the right finger forces the fluid to flow out of the contracted rim fraction, which results in a rim fraction with a smaller diameter and even higher pressure within this rim fraction. The higher pressure in return forces more fluid to flow out of this rim fraction resulting in capillary pinching, which represents locally an unstable process similar to the PR instability pattern. This instability expels liquid out of the rim constantly and leads to the growth of the right finger and merging of the middle finger and the left finger. At $t^* = 8.9$, the high pressure in the neck of the right finger forces the fluid to flow out of the neck constantly, which is also similar to the PR instability pattern, leading to a detachment of the secondary droplet at $t^* = 9.67$.

5.6 Influence of liquid viscosity

With the toolkit described in previous sections, we go forward to investigate the influence of the liquid viscosity on the collision process, above all, on the rim instability in the linear phase. Again, it is based on the most reliable case of $We = 442.3$. In the simulations, four other viscosities are employed resulting in Reynolds number 620.73, 3103.7, 31037 and 62073, along with the original water viscosity corresponding to $Re = 6207.3$ serving as a reference. All the other setups are untouched. A comparison between the reference case of $Re = 6207.3$ and a case with increased viscosity ($Re = 620.73$) and a case with a reduced viscosity ($Re = 62073$) is illustrated in Figure 5.16. It is obvious, that the higher viscosity suppresses the rim instability to a large amount, while the lower viscosity seemingly does not have a great impact on the rim instability, although the secondary droplets detach somewhat earlier.

5.6.1 Evolution of the rim geometry depending on viscosity

Neglecting the attached liquid film and assuming a circular section, the rim geometry is unambiguously determined by the evolution of the rim circumference $C(t) = 2\pi R_c(t)$ and the evolution of the rim radius $r_0(t)$, which are plotted in Figure 5.17 and 5.18, respectively. It should be noted that the evaluation starts at $t = 0.38$ other than $t = 0.25$ as it is described in

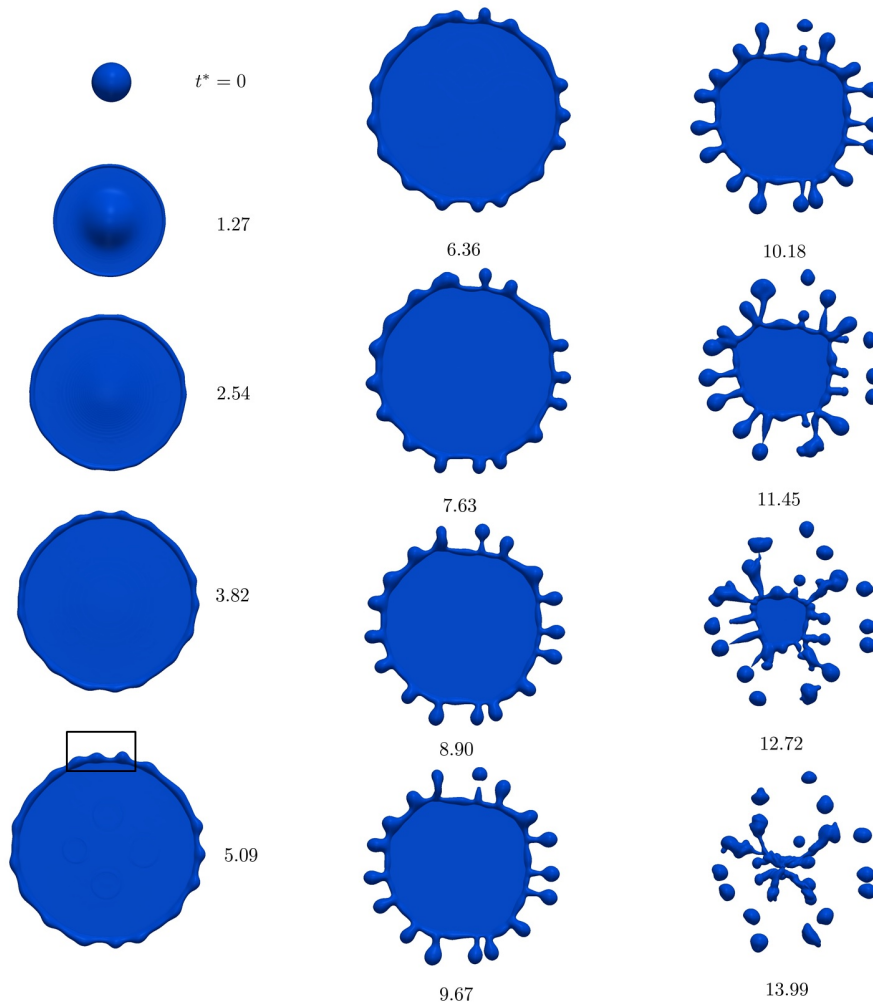


Figure 5.14.: Top view of interface evolution in the case $We = 442.3$ with initial disturbance of $\Delta U = 1\%$. The same simulation as shown in Figure 5.4 (c).

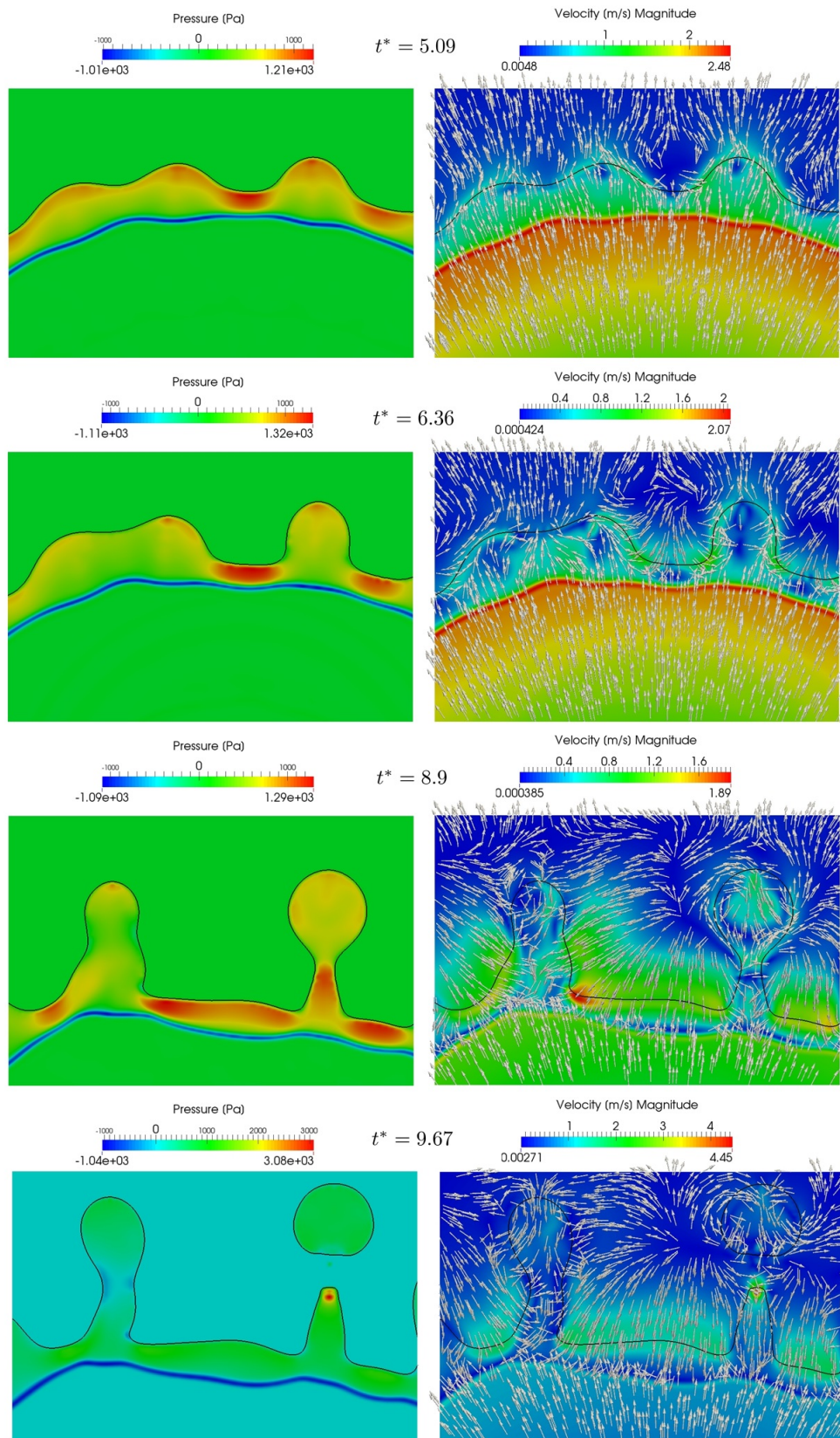


Figure 5.15.: Pressure field and velocity field of case $We = 442.3$ with initial disturbance of $\Delta U = 1\%$. The same simulation as shown in Figure 5.4 (c).

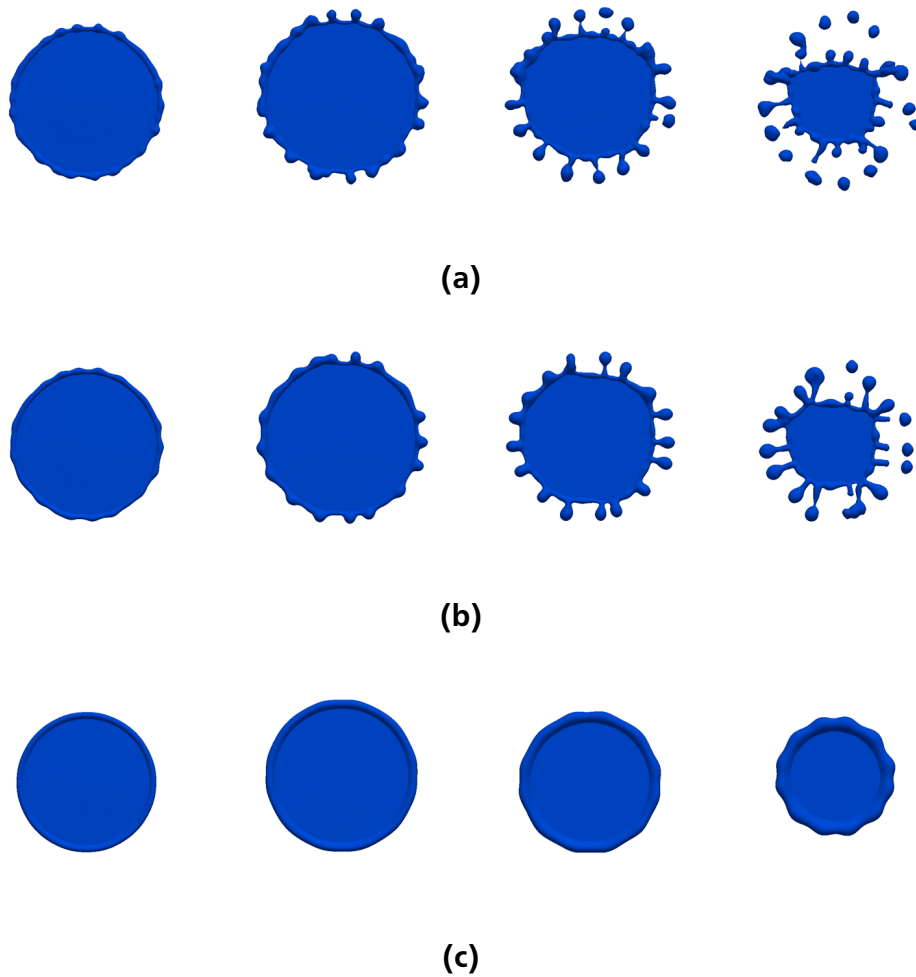


Figure 5.16.: Influence of viscosity variation on the rim instability. The Weber number is 442.3 for the three cases. (a) $Re = 62073$. (b) $Re = 6207.3$, reference case. (c) $Re = 620.73$. The corresponding dimensionless time is from left to right 3.82, 6.36, 8.91 and 11.20. In (a) and (c), the simulations are conducted with the same initial disturbance, as it is done in the reference case (b).

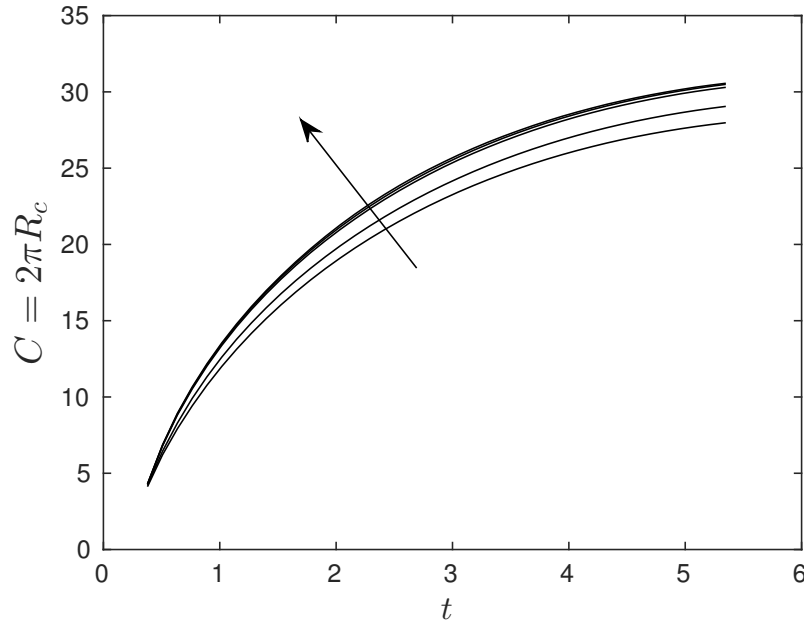


Figure 5.17.: Evolution of the rim circumferences. The Reynolds number are 620.73, 3103.7, 6207.3 (reference case), 31037 and 62073. The arrow points to the direction with increasing Reynolds number.

section 5.3.2, since at $t = 0.25$ not all the toroidal rims are formed in the five studied cases. One observes that the rim circumference increases and the rim radius decreases with increasing Reynolds number. This increment of the rim circumference and decrement of the rim radius become tiny at high Reynolds numbers.

5.6.2 Input signals and output signals in the linear unstable phase

Knowing the PR instability pattern dominates the rim instability in the linear phase, one can consider the evolving rim (from $t = 0.38$ to $t = 5.09$) as an amplification system that magnifies an input signal at $t = 0.38$ and yields an output signal at $t = 5.09$, as it is described in section 5.4. The signals are represented by the spectral diagrams shown in Figure 5.19 for three representative Reynolds numbers. The spectral diagrams are obtained by averaging 10 simulations with different initial disturbances of the same strength, as it is described in section 5.3.2. Since the spectral diagrams are not smooth, the maximum amplitudes and the region where the maximum amplitudes are located are represented by the (black) crosses in Figure 5.19. The position of the crosses is found as follows: in a first step, the spectrum is smoothed by applying local averaging over a window of ± 5 modes. The resulting curve shows a global maximum which yields the position of the crosses.

Comparing the input signals in Figure 5.19, the maximum amplitudes resulting from $Re = 6207.3$ and $Re = 62073$ are of the same order, while the maximum amplitudes resulting from $Re = 620.73$ are significantly smaller. The deviation of the region where the maximum amplitudes are located is small in the three cases. Comparing the output signals resulting from $Re = 6207.3$ and $Re = 62073$, the maximum amplitudes are again of the same order, and

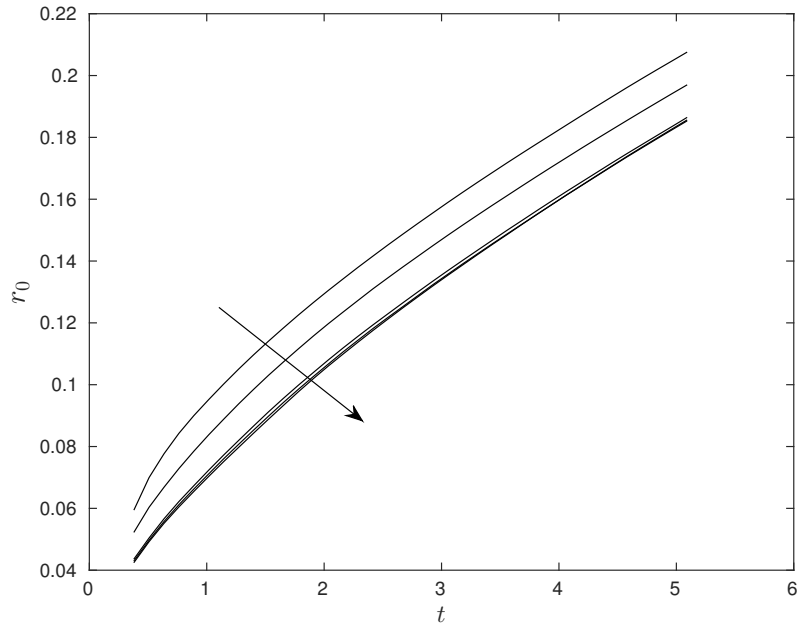


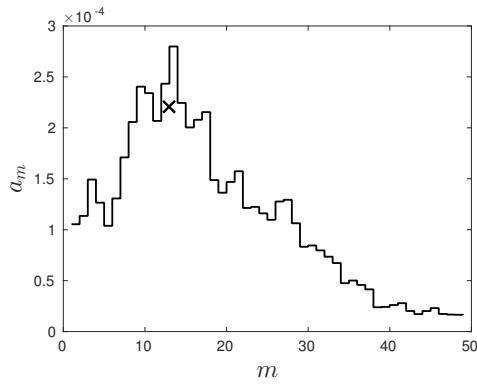
Figure 5.18.: Evolution of the rim radii. The Reynolds number are 620.73, 3103.7, 6207.3 (reference case), 31037 and 62073. The arrow points to the direction with increasing Reynolds number.

the deviation of the region where the maximum amplitudes are located is small. In the case of $Re = 620.7$, the maximum amplitudes are one order smaller and the region where the maximum amplitudes are located is significantly shifted to the left.

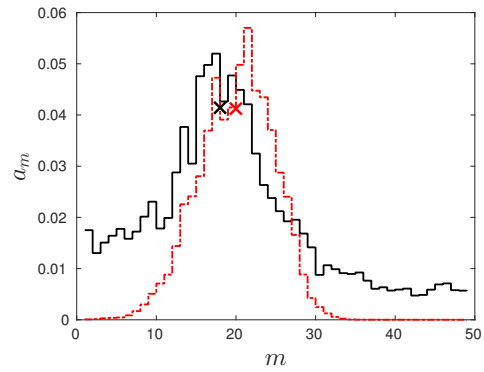
5.6.3 Growing rim as a signal amplification system

Applying the signals at $t = 0.38$ as initial conditions, the output signals predicted by the PR instability theory is shown in Figure 5.19. The maximum amplitudes and the region where the maximum amplitudes are located are represented by the red crosses in Figure 5.19, which are also obtained through averaging, as it is done for obtaining the black crosses. One can conclude, the rim instability can be predicted by the PR-Theory both at high and low Reynolds numbers, providing additional evidence for the previous statement that the PR-instability dominates the rim instability in the linear phase. At the low Reynolds number, the amplitudes are a bit underestimated due to the larger portion of the inherent disturbance in the simulation. The inherent disturbance consists of the anisotropic grid arrangement, the parasitic current, the discretization error and the truncation error, etc.

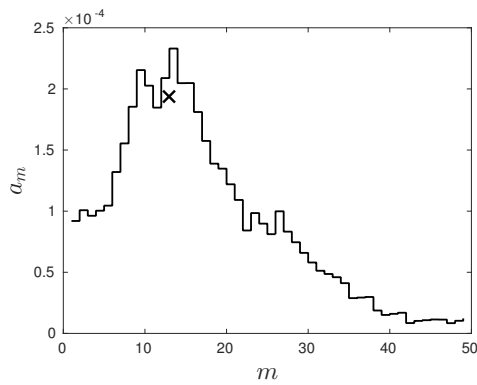
In the case of collision of water droplets ($Re=6307.3$), the maximum amplitudes are somewhat underestimated in the theoretical prediction which is in contradiction with the comparison shown in Figure 5.8 (d). The prediction shown in Figure 5.8 (d) is based on the signals at $t = 0.25$ other than $t = 0.38$. The difference between the results of the two predictions reveals that the growth rate between $t = 0.25$ and $t = 0.38$ is a bit overestimated. Still, the predictions starting from $t = 0.25$ and from $t = 0.38$ are both very good.



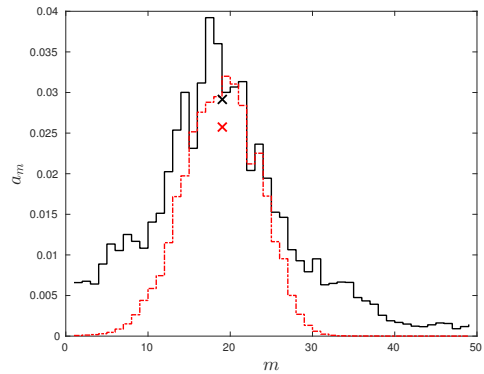
(a1): black cross: $(13, 2.2 \cdot 10^{-4})$



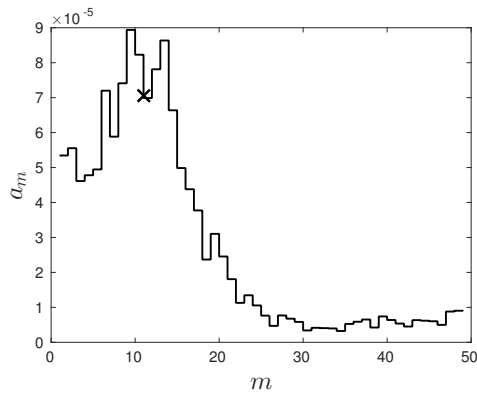
(a2): black cross: $(18, 414.7 \cdot 10^{-4})$
red cross: $(20, 412.4 \cdot 10^{-4})$



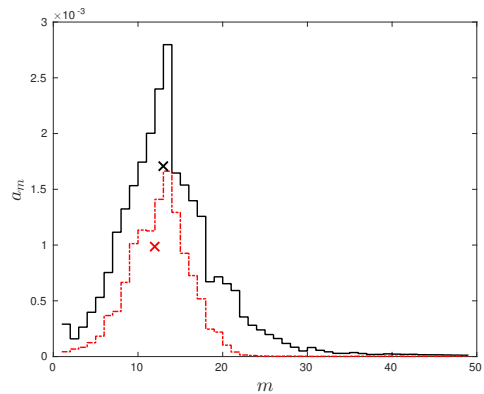
(b1): black cross: $(13, 1.94 \cdot 10^{-4})$



(b2): black cross: $(19, 291.8 \cdot 10^{-4})$
red cross: $(19, 257.4 \cdot 10^{-4})$



(c1): black cross: $(11, 7.06 \cdot 10^{-5})$



(c2): black cross: $(13, 170 \cdot 10^{-5})$
red cross: $(12, 98.92 \cdot 10^{-5})$

Figure 5.19.: Input signals at $t = 0.38$ (on the left) and output signals at $t = 5.09$ (on the right) and predicted output signals by the PR theory. The signals obtained from the evaluation of the DNS results are indicated by the black solid lines, while the predicted output signals by the red dot-dash lines. (a) $Re = 62073$. (b) $Re = 6207.3$, reference. (c) $Re = 620.73$. The black crosses represent the results from DNS. The red crosses represent the theoretical predictions.

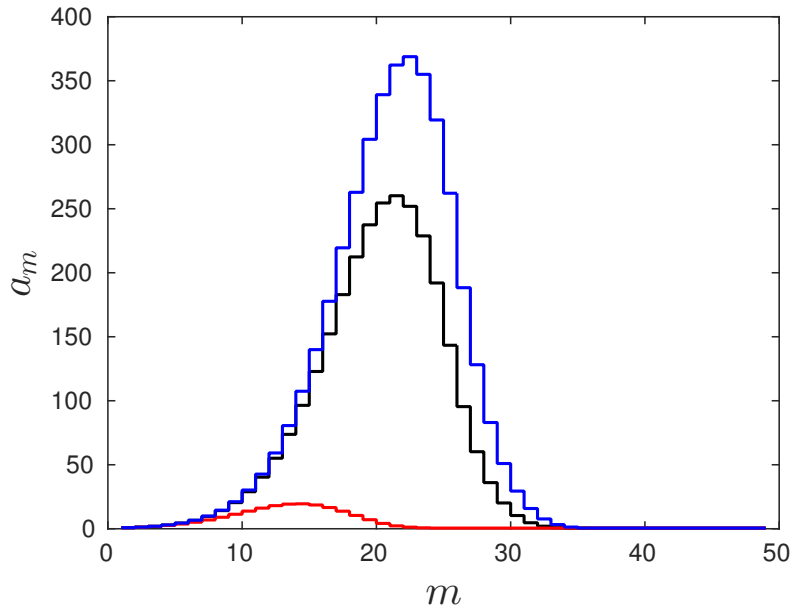


Figure 5.20.: Amplification factors of the three signal amplification systems corresponding to $Re = 6207.3$ (black line, reference), $Re = 62073$ (blue line) and $Re = 620.73$ (red line). The coordinates of the maximum amplification are $(21, 260.2)$, $(22, 368.8)$ and $(14, 19.5)$, respectively.

The signal amplification system can be characterized by the amplification factors of corresponding unstable modes. Applying the same initial values $a_m = 1$ for all modes, the magnified signal outcomes computed by the PR theory are shown in Figure 5.20, which reflects the amplification property of the three systems. Obviously, higher viscosity has a more significant effect, reducing the amplification factors and shifting the maximum growing mode to the left.

The liquid viscosity affects the property of the signal amplification system on one hand by affecting the evolution of the rim of the collision complex, i.e. $C(t)$ and $r_0(t)$ shown in Figure 5.17 and 5.18, on the other hand by affecting the growth rate of the instability modes, as the viscosity appears in the dispersion equation (5.11). The question is then, which effect is the dominant one. To answer this question, while computing the growth rate of the rim instability by means of equation (5.11) in the case of the low Reynolds number ($Re = 620.73$), the liquid viscosity is substituted by the viscosity of water (that of the reference case $Re = 6207.3$). The resulting amplification factors and the modes having the maximum amplification factors obtained from the theoretical prediction do not change much (in the sense that the amplification factors are still much smaller than the amplification factors at $Re = 6207.3$, which corresponds to a water droplet collision, and the mode having the maximum amplification factor merely shifts), revealing that the viscosity affects the rim instability mainly through varying the geometrical evolution of the rim on which the instability grows, see Figure 5.21. Note that the viscosity is only changed while applying the theoretical prediction, in order not to change the geometrical evolution of the rim in the simulation; if the viscosity would also be changed in the simulation, the result would be that of the reference case of $Re = 6207.3$.

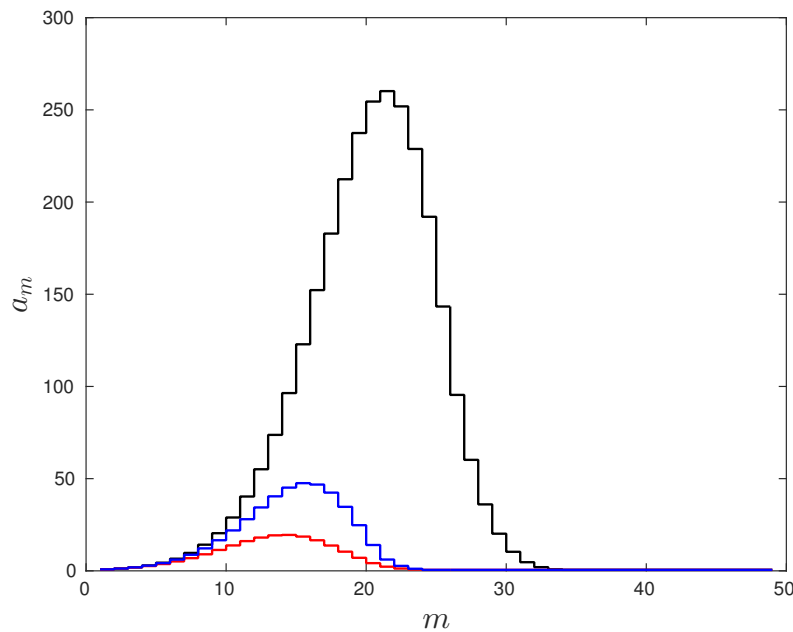


Figure 5.21.: Viscosity effect on the amplification factors of the signal amplification system. The black line represents the amplification factors of the case $Re = 6207.3$ (reference). The red line represents the amplification factors of the case $Re = 620.73$. The blue line represents the amplification system of the case $Re = 620.73$, while the liquid viscosity is substituted with that of the water viscosity. For the case of $Re = 620.73$ the coordinate of the maximum amplification shifts from $(14, 19.5)$ to $(15, 47.56)$ when the liquid viscosity is reduced by a factor of ten.

Lowering the liquid viscosity does not affect the amplification system much because it does not affect the geometry evolution of the rim much, as it is shown in Figure 5.17 and Figure 5.18.

5.6.4 Conclusion on the viscosity effect

On the basis of the above observations and analysis, one can conclude that reducing the liquid viscosity will promote the rim instability significantly at relatively low Reynolds numbers, while this effect becomes insignificant at very high Reynolds numbers. Very high liquid viscosity reduces the number of fingers by shifting the modes having the maximum amplitudes to a smaller number. When the liquid viscosity is high enough to have a significant effect, it yields on one hand more silent input signal for the linear phase of the rim instability considered as an amplification system, on the other hand leads to a linear amplification system with weaker amplification ability, resulting finally in much more stable collision processes. High liquid viscosity suppresses the amplification ability of the linear amplification system mainly through varying the geometrical evolution of the rim.

In addition, it has been shown that the rim instability can be predicted by the PR instability theory over a large Reynolds number range, which serves as a further evidence for the statement that the PR instability pattern is dominant in the linear unstable phase.

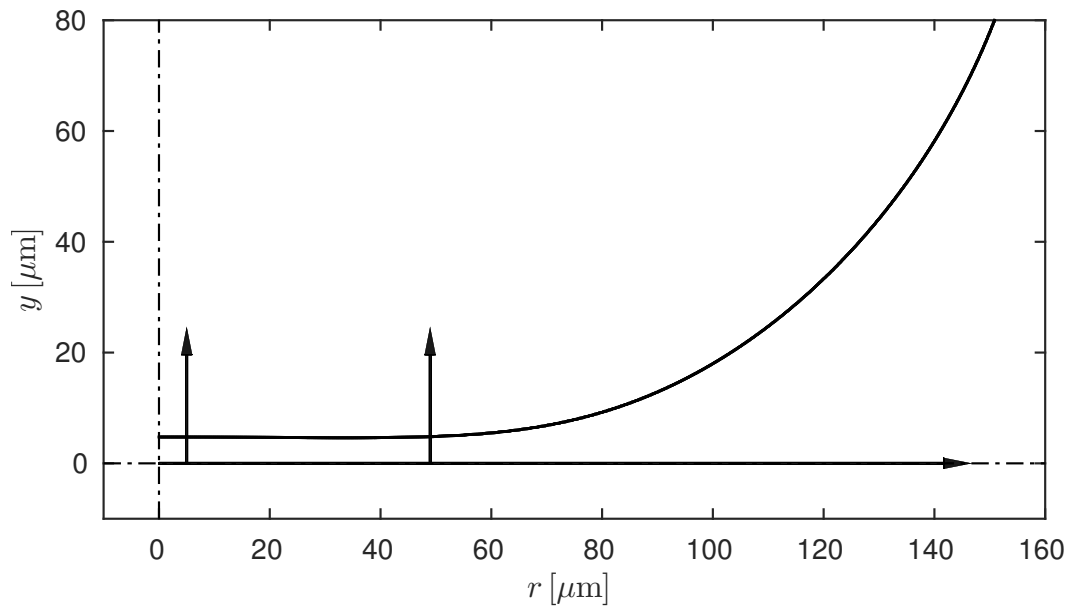


6 Flow in the Gas Layer between the Colliding Droplets

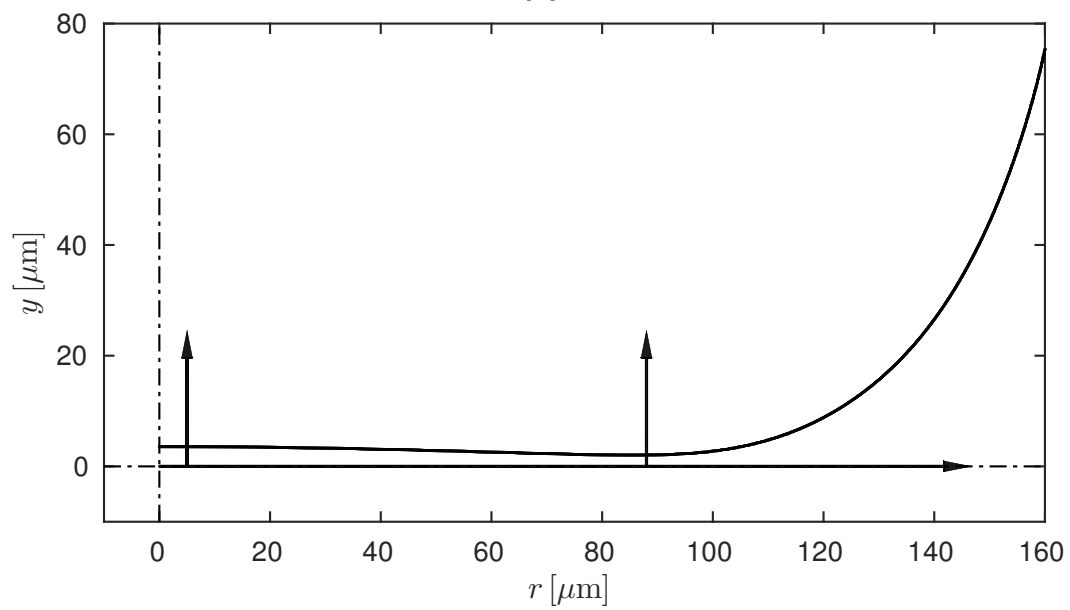
The flow in the gas layer between the colliding droplets, which is essential for the collision outcomes in terms of bouncing versus coalescence cannot be resolved by the computational cells feasible in 3D simulations. In order to gain some insight into the flow in the gas layer, a simulation in two-dimensions (2D) is conducted, which enables a significant increase of the grid resolution. Noticing the time step constraint due to viscosity is dependent on the square of the cell width, see equation (3.26), the grid refinement causes a fast decrease of the time step making the computation more expensive. In order to obtain an acceptable time step, the material parameters of the gas are modified to $\rho_g = 0.1 \cdot \rho_l$ and $\mu_g = 0.1 \cdot \mu_l$. The material of the droplets is tetradecane. Compared to the properties of air, the gas density and the gas viscosity are significantly increased. As a result, the gas layer resists the approach of the droplets more strongly and possesses therefore a larger thickness, which further facilitates the numerical investigation of the flow in the gas layer. The droplet diameter is resolved by 512 cells. The balanced-CSF model is employed. Detailed setups are found in table C.8 in Appendix C.

The following description is more about the objective observation which serves as basis knowledges of the flow in the gas layer. The simulation results are evaluated for two typical stages in the collision process, i.e. when the gas layer is just formed with tiny deformations of the droplets ($t = 0.28$ ms) and when the gas layer is significantly extended in radial direction ($t = 0.32$ ms), see Figure 6.1. At the two evaluated time instants, the thickness of the gas layer is resolved by at least 16 cells. The arrows in Figure 6.1 indicate the lines along which the results are evaluated. For $t = 0.28$ ms, the pressure profiles and the velocity profiles are shown in Figure 6.2. One observes that the pressure is almost constant across the gas layer and there is a pressure jump across the interface both near the stagnation point and near the edge of the gas layer. The edge of the gas layer is defined as the position before rapidly enlarging gas layer thickness. The pressure jump can be attributed to both the surface tension force and the jump of the viscous force across the interface as it is implied by the momentum jump condition (equation (2.12)). The velocity u_r in the gas layer is much larger than the velocity in the droplet near the interface indicating the squeezing of the gas out of the gap. Furthermore, the profile of the velocity u_r across the gas layer corresponds nearly to a parabolic curve. The pressure decreases in radial direction. The velocity decreases rapidly beyond around $r = 80 \mu\text{m}$ because of the rapid increase of the gas layer thickness beyond the edge of the gas layer.

The evaluation for the latter instant $t = 0.32$ ms is shown in Figure 6.3. Here, only the significant differences compared to the results at earlier time $t = 0.28$ ms are addressed. First, the squeezing velocity u_r near the stagnation point is much smaller compared to the result at the earlier time, indicating a trapping of the gas near the stagnation point. This is consistent



(a)



(b)

Figure 6.1.: The profiles of the droplet near the gas layer. The dot-dashed lines represent the symmetry planes. The arrows represent the lines along which the velocity and pressure are evaluated. (a) evaluation at $t = 0.28$ ms. (b) evaluation at $t = 0.32$ ms.

with the fact that the gas layer thickness near the stagnation point does not decrease much compared to the former time instant and is larger than the gas layer thickness at the edge. Secondly, the velocity profile changes from convex to concave, which reason is attributed to the reversed sign of the pressure derivative in radial direction at the corresponding position ($\frac{dp}{dx}|_{x=5.0\mu\text{m}} = 1.5 \cdot 10^4 \text{ N/m}^3$ compared to the negative pressure derivative $-3.2 \cdot 10^5 \text{ N/m}^3$ at $t = 0.28 \text{ ms}$).

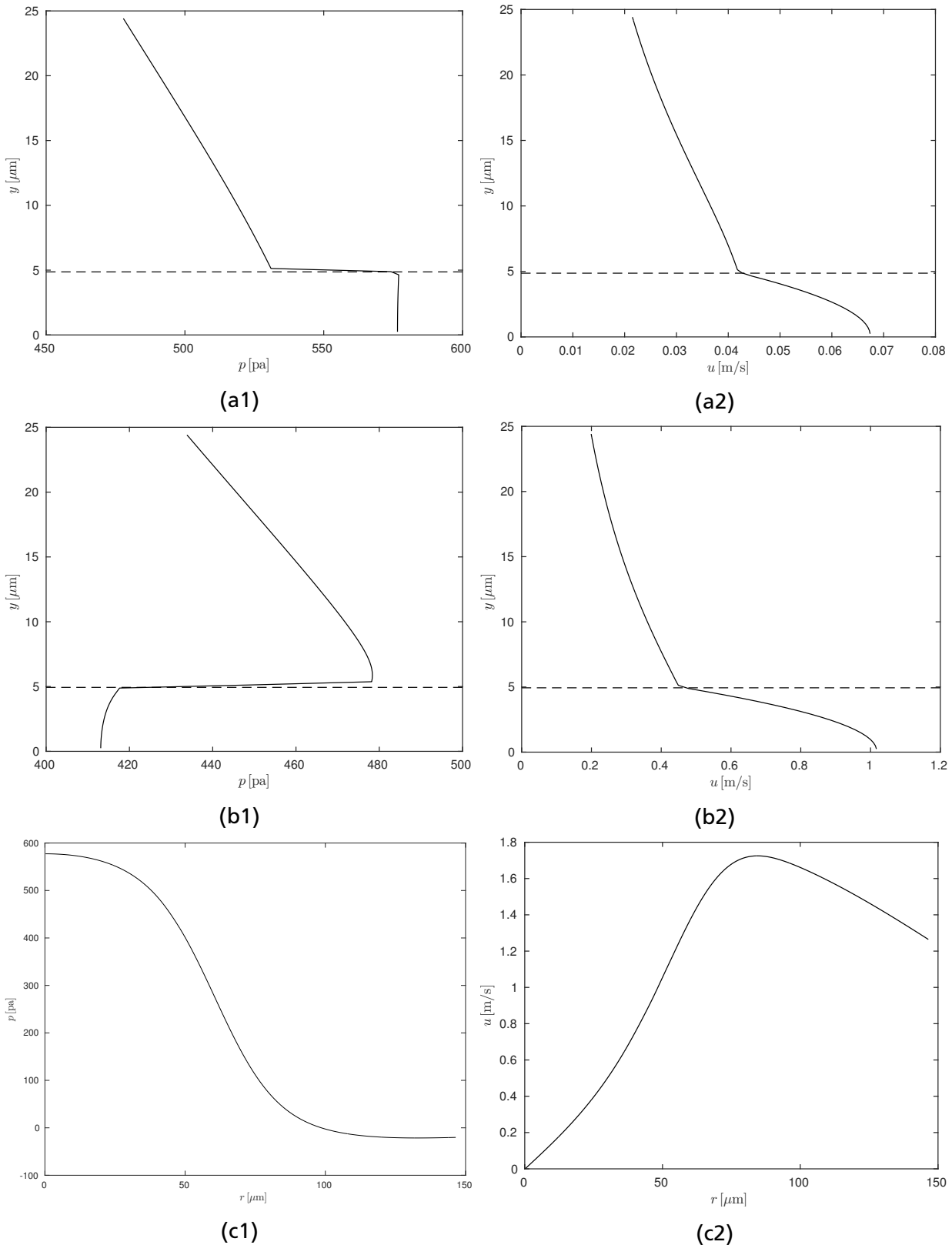


Figure 6.2.: The pressure and velocity profiles along the arrows indicated in Figure 6.1a. The dashed lines represent the local interface positions computed by means of the height function. (a) evaluation near the stagnation point at $r = 5.0 \mu\text{m}$. (b) evaluation at the edge of the gas layer ($r = 49.0 \mu\text{m}$). (c) evaluation along the symmetry plane.

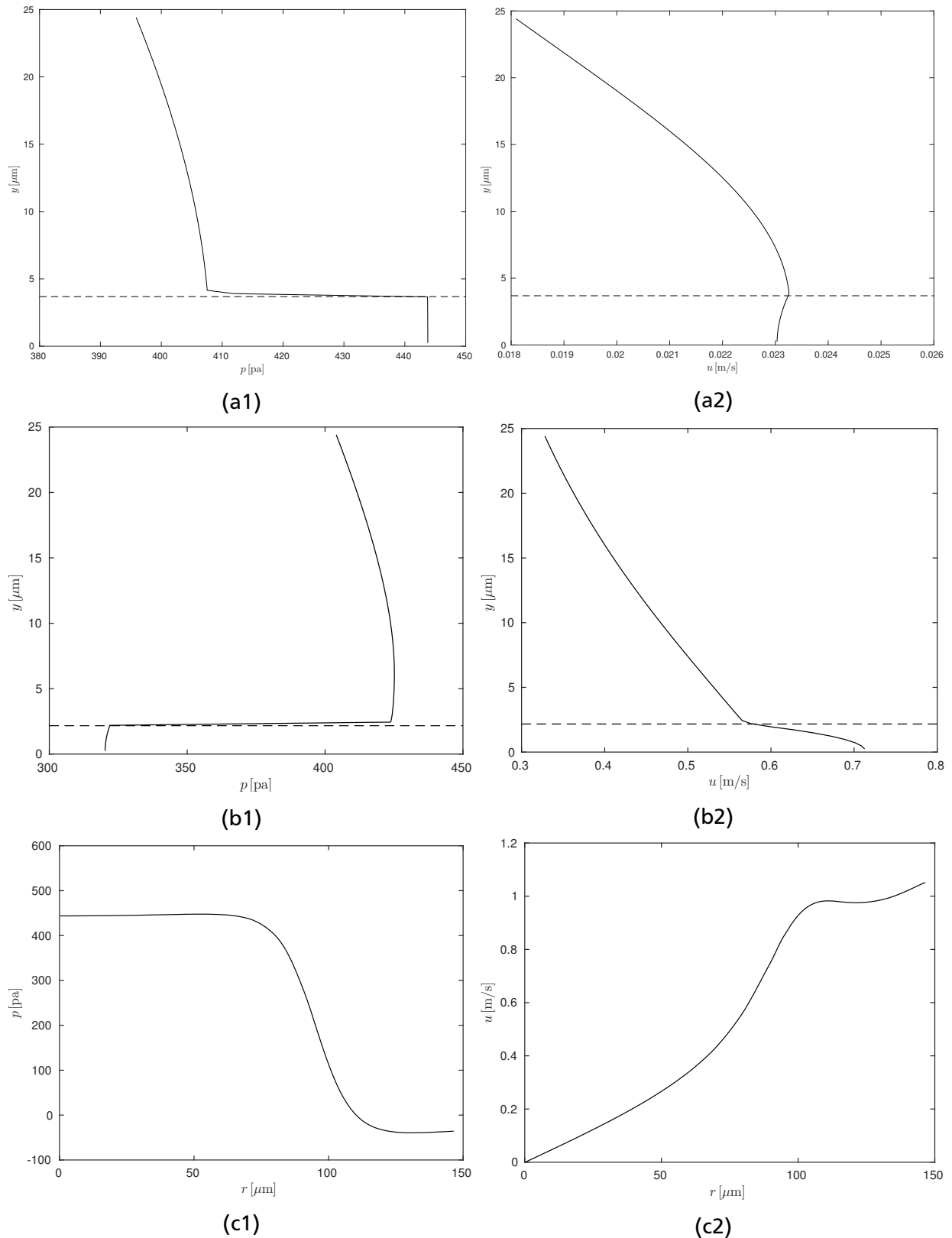


Figure 6.3.: The pressure and velocity profiles along the arrows indicated in Figure 6.1b. The dashed lines represent the local interface positions computed by means of the height function. (a) evaluation near the stagnation point at $r = 5.0 \mu\text{m}$. (b) evaluation at the edge of the gas layer ($r = 88.0 \mu\text{m}$). (c) evaluation along the symmetry plane.



7 Multi-Scale Simulations aiming at Predictions of the Transition between Bouncing and Coalescence

It is shown in Chapter 4 that both coalescence and bouncing can be reproduced by a modification of the boundary conditions of the f -field for the collision plane in the simulations, which have not been able to be predictive in terms of whether the collision outcome is bouncing or coalescence. The flow in the gas layer cannot be resolved by computational cells in DNS in feasible 3D-simulations. Establishing a SGS model properly, the flow in the gas layer has to be resolved on a sub-grid scale. With proper coalescence criteria, the simulations should be able to predict the collision outcome in terms of coalescence versus bouncing. The conceptual design for facilitating a predictive simulation is summarized as follows:

1. Developing a SGS model that solves the flow in the gas layer and which is integrated into the main solver FS3D.
2. The coalescence is first suppressed by modifying the boundary condition for the f -field on the collision plane.
3. At the time when a proper coalescence criterion is fulfilled, the boundary condition is switched to standard symmetric boundary condition so that coalescence is able to occur.

A simulation is called a multi-scale simulation within this thesis if it is conducted with a SGS model which solves the flow on the microscopic scale and is integrated into the main solver FS3D solving the macroscopic process.

In this chapter, the derivation, implementation and validation of the SGS model are first presented. Then the integration of the SGS model into the main solver FS3D is discussed. By means of two possible coalescence criteria, the predictions of the collision outcomes are presented and discussed. At the end, the rarefaction effect is studied qualitatively.

7.1 Derivation of the SGS model starting from the lubrication theory

In binary droplet collisions, a gas layer between the approaching droplets forms which causes bouncing or delays the possible coalescence. As it has been shown in the 2D simulation in Chapter 6, the dimension of the gas layer in the radial direction is much larger than in the axial direction. The flow in such a fluid film can be described by the lubrication theory which exploits the very small ratio between the film thickness to lateral extension in order to reduce the Navier-Stokes equations.

Assuming constant material parameters without considering the body force, the incompressible Navier-Stokes equations for a general fluid film between two planes are written as

$$\begin{aligned}\rho\left(\frac{\partial u}{\partial t} + u\frac{\partial u}{\partial x} + v\frac{\partial u}{\partial y} + w\frac{\partial u}{\partial z}\right) &= -\frac{\partial p}{\partial x} + \eta\left(\frac{\partial^2 u}{\partial x^2} + \frac{\partial^2 u}{\partial y^2} + \frac{\partial^2 u}{\partial z^2}\right), \\ \rho\left(\frac{\partial v}{\partial t} + u\frac{\partial v}{\partial x} + v\frac{\partial v}{\partial y} + w\frac{\partial v}{\partial z}\right) &= -\frac{\partial p}{\partial y} + \eta\left(\frac{\partial^2 v}{\partial x^2} + \frac{\partial^2 v}{\partial y^2} + \frac{\partial^2 v}{\partial z^2}\right), \\ \rho\left(\frac{\partial w}{\partial t} + u\frac{\partial w}{\partial x} + v\frac{\partial w}{\partial y} + w\frac{\partial w}{\partial z}\right) &= -\frac{\partial p}{\partial z} + \eta\left(\frac{\partial^2 w}{\partial x^2} + \frac{\partial^2 w}{\partial y^2} + \frac{\partial^2 w}{\partial z^2}\right),\end{aligned}\quad (7.1)$$

along with the equation of continuity, i.e.

$$\frac{\partial u}{\partial x} + \frac{\partial v}{\partial y} + \frac{\partial w}{\partial z} = 0. \quad (7.2)$$

According to Hamrock et al. [22], the following dimensionless variables can be defined:

$$\begin{aligned}\tilde{x} &= \frac{x}{l_0} & \tilde{y} &= \frac{y}{b_0} & \tilde{z} &= \frac{z}{h_0} & \tilde{t} &= \frac{t}{t_0} \\ \tilde{u} &= \frac{u}{u_0} & \tilde{v} &= \frac{v}{v_0} & \tilde{w} &= \frac{w}{w_0} & \tilde{p} &= \frac{h_0^2 p}{\eta u_0 l_0}\end{aligned}\quad (7.3)$$

with

- l_0 characteristic length in x direction, m
- b_0 characteristic length in y direction, m
- h_0 characteristic length in z direction, m
- t_0 characteristic time, s
- u_0 characteristic velocity in x direction, m/s
- v_0 characteristic velocity in y direction, m/s
- w_0 characteristic velocity in z direction, m/s

Employing the dimensionless variables according to equation (7.3), the x -component of equation (7.1) gives

$$\begin{aligned}\frac{l_0}{u_0 t_0} \frac{\partial \tilde{u}}{\partial \tilde{t}} + \tilde{u} \frac{\partial \tilde{u}}{\partial \tilde{x}} + \frac{l_0 v_0}{b_0 u_0} \tilde{v} \frac{\partial \tilde{u}}{\partial \tilde{y}} + \frac{l_0 w_0}{h_0 u_0} \tilde{w} \frac{\partial \tilde{u}}{\partial \tilde{z}} &= -\frac{\eta}{\rho u_0 l_0} \left(\frac{l_0}{h_0}\right)^2 \frac{\partial \tilde{p}}{\partial \tilde{x}} \\ &+ \frac{\eta}{\rho u_0 l_0} \frac{\partial^2 \tilde{u}}{\partial \tilde{x}^2} + \frac{\eta l_0}{\rho u_0 b_0^2} \frac{\partial^2 \tilde{u}}{\partial \tilde{y}^2} + \frac{\eta l_0}{\rho u_0 h_0^2} \frac{\partial^2 \tilde{u}}{\partial \tilde{z}^2}.\end{aligned}\quad (7.4)$$

Equation (7.4) can be reformulated:

$$\Omega \frac{\partial \tilde{u}}{\partial \tilde{t}} + \text{Re}_x \tilde{u} \frac{\partial \tilde{u}}{\partial \tilde{x}} + \text{Re}_y \tilde{v} \frac{\partial \tilde{u}}{\partial \tilde{y}} + \text{Re}_z \tilde{w} \frac{\partial \tilde{u}}{\partial \tilde{z}} = -\frac{\partial \tilde{p}}{\partial \tilde{x}} + \left(\frac{h_0}{l_0}\right)^2 \frac{\partial^2 \tilde{u}}{\partial \tilde{x}^2} + \left(\frac{h_0}{b_0}\right)^2 \frac{\partial^2 \tilde{u}}{\partial \tilde{y}^2} + \frac{\partial^2 \tilde{u}}{\partial \tilde{z}^2}, \quad (7.5)$$

where the modified Reynolds number Re_x , Re_y , Re_z and the squeeze number Ω are defined as

$$Re_x = \frac{\rho u_0 h_0^2}{\eta l_0}, \quad (7.6)$$

$$Re_y = \frac{\rho v_0 h_0^2}{\eta b_0}, \quad (7.7)$$

$$Re_z = \frac{\rho w_0 h_0}{\eta}, \quad (7.8)$$

$$\Omega = \frac{\rho h_0^2}{\eta t_0}. \quad (7.9)$$

Due to the equation of continuity (7.2) it is clear that $u_0/l_0 \sim w_0/h_0 \sim v_0/b_0$. Furthermore, the characteristic time can be estimated based on the approaching movement of the two planes or $t_0 \approx h_0/w_0$. Therefore, Re_x , Re_y , Re_z and Ω are all of order h_0/l_0 or h_0/b_0 . The first and second viscous terms of equation (7.5) are of order $(h_0/l_0)^2$ and $(h_0/b_0)^2$, respectively. Neglecting the first- and second-order terms of h_0/l_0 and h_0/b_0 in equation (7.5) yields

$$\frac{\partial p(x, y, z)}{\partial x} = \eta \frac{\partial^2 u(x, y, z)}{\partial z^2} \quad (7.10)$$

in the form containing dimensions. A similar procedure applies to the y - and z -components of the Navier-Stokes equations (7.1), giving

$$\frac{\partial p(x, y, z)}{\partial y} = \eta \frac{\partial^2 v(x, y, z)}{\partial z^2}, \quad (7.11)$$

$$\frac{\partial p(x, y, z)}{\partial z} = 0. \quad (7.12)$$

Equation (7.12) describes that the pressure can be assumed to be constant along the thickness of the fluid film, the validity of which for the gas layer in binary droplet collisions is confirmed by the 2D simulation described in Chapter 6. The equations (7.10), (7.11) and (7.12) are reformulated as

$$\frac{\partial p}{\partial x} = \eta \frac{\partial^2 u}{\partial z^2}, \quad (7.13)$$

$$\frac{\partial p}{\partial y} = \eta \frac{\partial^2 v}{\partial z^2}, \quad (7.14)$$

with $u = u(x, y, z)$, $v = v(x, y, z)$, $p = p(x, y)$. The following derivations are based on a coordinate system possessing the xy -plane as a symmetry plane, see Figure 7.1. Integrating equation (7.13) twice with respect to z and applying the boundary conditions $\frac{\partial u}{\partial z}|_{z=0} = 0$ and $u(x, y, h) = u_a$, the velocity of the flow in the fluid film in x -direction is given as

$$u = u_a + \frac{z^2 - h^2}{2\eta} \frac{\partial p}{\partial x}. \quad (7.15)$$

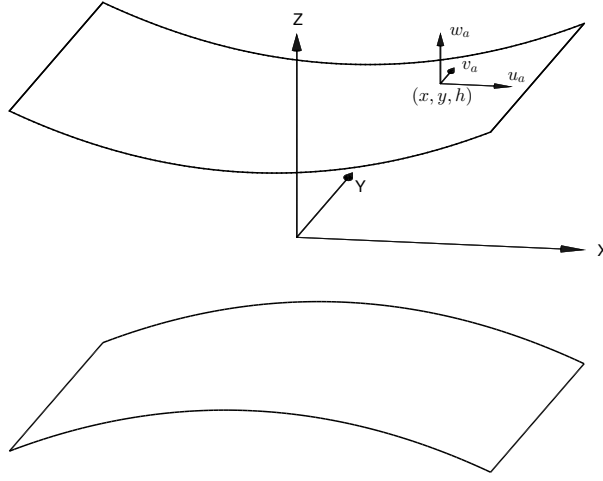


Figure 7.1.: A fluid film between two planes that can move and deform. The local movement of the upper plate is described by $\mathbf{u}_a = (u_a, v_a, w_a)$. The two planes are symmetric with respect to the plane xy .

Similarly with $\frac{\partial v}{\partial z}|_{z=0} = 0$ and $v(x, y, h) = v_a$, the velocity in y -direction is given as

$$v = v_a + \frac{z^2 - h^2}{2\eta} \frac{\partial p}{\partial y}. \quad (7.16)$$

Inserting equations (7.15) and (7.16) into the equation of continuity (7.2) yields

$$\begin{aligned} \frac{\partial w}{\partial z} = & -\frac{\partial u_a}{\partial x} - \frac{\partial v_a}{\partial y} + \frac{h}{\eta} \frac{\partial p}{\partial x} \frac{\partial h}{\partial x} + \frac{h}{\eta} \frac{\partial p}{\partial y} \frac{\partial h}{\partial y} \\ & - \frac{1}{2\eta} \frac{\partial^2 p}{\partial x^2} (z^2 - h^2) - \frac{1}{2\eta} \frac{\partial^2 p}{\partial y^2} (z^2 - h^2). \end{aligned} \quad (7.17)$$

Integration in z -direction and applying the boundary condition $w(x, y, 0) = 0$ yields

$$\begin{aligned} w = & -z \frac{\partial u_a}{\partial x} - z \frac{\partial v_a}{\partial y} + z \frac{h}{\eta} \frac{\partial p}{\partial x} \frac{\partial h}{\partial x} + z \frac{h}{\eta} \frac{\partial p}{\partial y} \frac{\partial h}{\partial y} \\ & - \frac{1}{2\eta} \frac{\partial^2 p}{\partial x^2} \left(\frac{1}{3} z^3 - h^2 z \right) - \frac{1}{2\eta} \frac{\partial^2 p}{\partial y^2} \left(\frac{1}{3} z^3 - h^2 z \right). \end{aligned} \quad (7.18)$$

Applying the boundary condition $w(x, y, h) = w_a$ yields

$$\frac{\partial}{\partial x} \left(h^3 \frac{\partial p}{\partial x} \right) + \frac{\partial}{\partial y} \left(h^3 \frac{\partial p}{\partial y} \right) = 3\eta \left(w_a + h \left(\frac{\partial u_a}{\partial x} + \frac{\partial v_a}{\partial y} \right) \right). \quad (7.19)$$

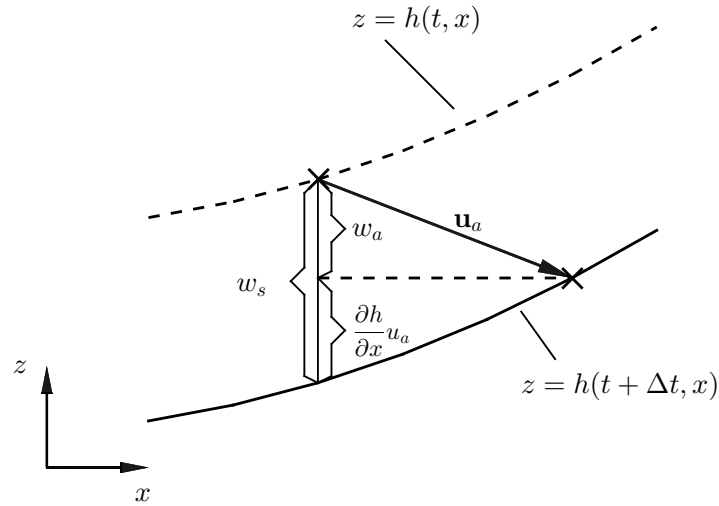


Figure 7.2.: Relation between the z -component w_a of the boundary velocity \mathbf{u}_a and the resultant velocity w_s of the upper boundary.

Assuming ‘frozen’ local partial derivatives of h (time-independent $\frac{\partial h}{\partial x}$ and $\frac{\partial h}{\partial y}$), the velocity w_a of the upper boundary in z -direction is given as (see the schematic in Figure 7.2)

$$w_a = w_s + u_a \frac{\partial h}{\partial x} + v_a \frac{\partial h}{\partial y}, \quad (7.20)$$

where w_s is the resultant velocity of the upper boundary given as

$$w_s(x, y) = \frac{\partial h}{\partial t}. \quad (7.21)$$

Inserting (7.20) into (7.19) finally yields the lubrication equation:

$$\frac{\partial}{\partial x} \left(h^3 \frac{\partial p}{\partial x} \right) + \frac{\partial}{\partial y} \left(h^3 \frac{\partial p}{\partial y} \right) = 3\eta \left(w_s + \frac{\partial(hu_a)}{\partial x} + \frac{\partial(hv_a)}{\partial y} \right). \quad (7.22)$$

7.1.1 Analytical solutions of two idealized cases

In binary droplet collisions, the gas film between the colliding droplets is on one hand squeezed out of the gas layer due to the approaching motion of the droplets, on the other hand dragged by the liquid/gas interfaces moving outwards in the radial direction. The corresponding ‘squeezing effect’ and ‘dragging effect’ are described in detail by means of analytical solutions of the lubrication equation for two idealized 2D cases. In order to understand the ‘squeezing effect’, we consider the flow between two parallel planes approaching each other with constant velocity w_s ; see the schematic in Figure 7.3a. Eliminating the derivatives of

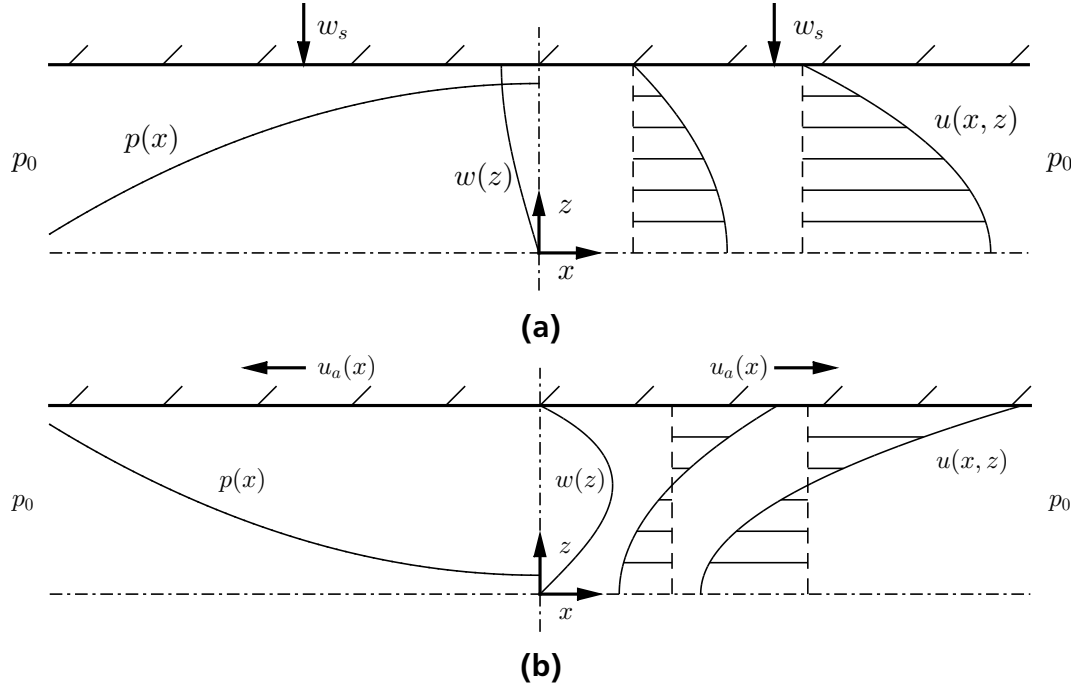


Figure 7.3.: Schematic description of two idealized cases and analytical solutions. The dot-dashed lines represent the symmetry planes. The lengths of the planes are $2l$. (a) two parallel planes approach each other. The sign of $w(z)$ is negative. (b) the parallel planes stretch outwardly in x -direction. The sign of $w(z)$ is positive.

the lubrication equation (7.22) with respect to y and applying the boundary conditions, the analytical solution for the pressure is given as

$$p(x) = \frac{3\eta w_s}{2h^3}(x^2 - l^2) + p_0. \quad (7.23)$$

Inserting the obtained pressure into equations (7.15) yields

$$u(x, z) = \frac{3w_s(z^2 - h^2)x}{2h^3}. \quad (7.24)$$

Then, the equation of continuity gives

$$w(z) = \frac{1}{2}w_s\left(3\frac{z}{h} - \left(\frac{z}{h}\right)^3\right). \quad (7.25)$$

The solutions are also illustrated in Figure 7.3a. One sees that the ‘squeezing effect’ results in a higher pressure in the interior of the fluid film and the pressure gradient results in velocity profiles pointing outwards. The ‘dragging effect’ is described by means of two parallel planes stretching outwardly with velocity $u_a(x) = \alpha x$, see Figure 7.3b. The analytical solutions are given as

$$p(x) = \frac{3\eta\alpha}{2h^2}(x^2 - l^2) + p_0, \quad (7.26)$$

$$u(x, z) = \alpha x + \frac{3\alpha(z^2 - h^2)x}{2h^2}, \quad (7.27)$$

$$w(z) = \frac{\alpha z}{2}\left(1 - \frac{z^2}{h^2}\right). \quad (7.28)$$

The solutions are also illustrated in Figure 7.3b. One sees that the ‘dragging effect’ results in a lower pressure in the interior of the fluid film and the pressure gradient results in velocity profiles pointing inwards. Especially, the velocity $u(x, z)$ is negative near the x -axis. This is no surprise due to the volume conservation.

7.1.2 Rarefied lubrication equation

In binary droplet collisions, the critical distance between the colliding droplets is in the order of 10 nm, as it is mentioned in the introduction. Since the mean free path of gas molecules λ is about 100 nm [71] under standard ambient conditions, the flow in the gas film must necessarily go from the continuous flow through the slip flow regime and then into the transitional flow regime before possible coalescence of droplets or in case the droplets ‘almost’ coalesce.

The derivation of the lubrication equation is valid for continuous flow meaning $\text{Kn} \ll 1$. In the slip regime where $0.01 < \text{Kn} < 0.1$, the continuum models can still be used to investigate the gas flow with a modified boundary condition which allows a slip at the gas/liquid or gas/solid interfaces. According to Shukla et al. [61], a relation between slip velocity and shear can be given as

$$u_{\text{slip}} = \lambda \left(\frac{\partial u}{\partial z} \right)_{\text{wall}}. \quad (7.29)$$

In order to investigate the rarefied flow in the transitional region where $0.1 < \text{Kn} < 10$, generally one needs to solve the Boltzmann equation [60]. Dongari et al. [14] suggested that the validity of the continuum models can be extended to the transitional region by applying second-order slip models, which general form is given as

$$u_{\text{slip}} = C_1 \lambda \left(\frac{\partial u}{\partial z} \right)_{\text{wall}} + C_2 \lambda^2 \left(\frac{\partial^2 u}{\partial z^2} \right)_{\text{wall}}. \quad (7.30)$$

Although the validity of the second-order slip models seems to be a consensus, a general agreement on the values of the coefficients C_1 and C_2 has not been achieved, see a summary given by Dongari et al. [14]. In the present thesis, the coefficients of C_1 and C_2 are calibrated by means of an analytical solution of a lubricant problem given by Zhang and Law [71]. The calibration is described later on.

Starting from the lubrication assumption (7.13) and (7.14), the lubrication equation including the rarefaction effect is derived. The derivation is inspired by the work of Shukla et al. [61]. With the general form of the second-order slip model (7.30), the boundary conditions are given for the lower surface as

$$u = (u)_1 = u_{a1} + C_1 \lambda \left(\frac{\partial u}{\partial z} \right)_1 + C_2 \lambda^2 \left(\frac{\partial^2 u}{\partial z^2} \right)_1, \quad (7.31)$$

$$v = (v)_1 = v_{a1} + C_1 \lambda \left(\frac{\partial v}{\partial z} \right)_1 + C_2 \lambda^2 \left(\frac{\partial^2 v}{\partial z^2} \right)_1, \quad (7.32)$$

and for the upper surface as

$$u = (u)_2 = u_{a2} - C_1 \lambda \left(\frac{\partial u}{\partial z} \right)_2 - C_2 \lambda^2 \left(\frac{\partial^2 u}{\partial z^2} \right)_2, \quad (7.33)$$

$$v = (v)_2 = v_{a2} - C_1 \lambda \left(\frac{\partial v}{\partial z} \right)_2 - C_2 \lambda^2 \left(\frac{\partial^2 v}{\partial z^2} \right)_2, \quad (7.34)$$

where the subscript 1 and 2 denote the gas phase at $z = H_1$ and $z = H_2$ respectively. The subscript a denotes the gas/liquid or gas/solid interface.

The velocities in z -direction are given as (compare with the schematic illustration in Figure 7.2):

$$(w)_1 = w_{s1} + (u)_1 \frac{\partial H_1}{\partial x} + (v)_1 \frac{\partial H_1}{\partial y}, \quad (7.35)$$

$$(w)_2 = w_{s2} + (u)_2 \frac{\partial H_2}{\partial x} + (v)_2 \frac{\partial H_2}{\partial y}, \quad (7.36)$$

where the subscript s denotes the resultant velocity of the gas/liquid or gas/solid interface towards the gas film.

Integrating equations (7.13), (7.14) over z and applying the boundary conditions (7.31-7.34) gives the velocity in the gas layer:

$$u = u_{a1} + \left(\frac{C_1 \lambda}{\eta} H_1 + \frac{C_2 \lambda^2}{\eta} + \frac{1}{\eta} \int_{H_1}^z z' dz' \right) \frac{\partial p}{\partial x} + \left(\frac{u_{a2} - u_{a1}}{F} - \frac{F_1}{F_0} \frac{\partial p}{\partial x} \right) \left(\frac{\lambda}{\eta} + \frac{1}{\eta} \int_{H_1}^z dz' \right), \quad (7.37)$$

$$v = v_{a1} + \left(\frac{C_1 \lambda}{\eta} H_1 + \frac{C_2 \lambda^2}{\eta} + \frac{1}{\eta} \int_{H_1}^z z' dz' \right) \frac{\partial p}{\partial y} + \left(\frac{v_{a2} - v_{a1}}{F} - \frac{F_1}{F_0} \frac{\partial p}{\partial y} \right) \left(\frac{\lambda}{\eta} + \frac{1}{\eta} \int_{H_1}^z dz' \right), \quad (7.38)$$

with

$$F_0 = \frac{2C_1 \lambda}{\eta} + \frac{1}{\eta} (H_2 - H_1), \quad F_1 = \frac{C_1 \lambda}{\eta} (H_1 + H_2) + \frac{1}{\eta} \int_{H_1}^{H_2} z dz. \quad (7.39)$$

Integrating the equation of continuity with respect to z from $z = H_1$ to $z = H_2$ gives

$$\int_{H_1}^{H_2} \frac{\partial u}{\partial x} dz + \int_{H_1}^{H_2} \frac{\partial v}{\partial y} dz + [w]_{H_1}^{H_2} = 0. \quad (7.40)$$

Equation (7.40) is equivalent to

$$\frac{\partial}{\partial x} \int_{H_1}^{H_2} u dz + \frac{\partial}{\partial y} \int_{H_1}^{H_2} v dz - (u)_2 \frac{\partial H_2}{\partial x} - (v)_2 \frac{\partial H_2}{\partial y} + (u)_1 \frac{\partial H_1}{\partial x} + (v)_1 \frac{\partial H_1}{\partial y} + [w]_{H_1}^{H_2} = 0. \quad (7.41)$$

Inserting equations (7.37), (7.38) into (7.41) gives

$$\begin{aligned} \frac{\partial}{\partial x} (F_2 \frac{\partial p}{\partial x}) + \frac{\partial}{\partial y} (F_2 \frac{\partial p}{\partial y}) = & H_2 \left(\frac{\partial (u)_2}{\partial x} + \frac{\partial (v)_2}{\partial y} \right) - H_1 \left(\frac{\partial (u)_1}{\partial x} + \frac{\partial (v)_1}{\partial y} \right) - \\ & \frac{\partial}{\partial x} \left(\frac{(u_{a2} - u_{a1}) F_3}{F_0} \right) - \frac{\partial}{\partial y} \left(\frac{(v_{a2} - v_{a1}) F_3}{F_0} \right) + [w]_{H_1}^{H_2} \end{aligned} \quad (7.42)$$

with

$$F_2 = \frac{1}{\eta} \int_{H_1}^{H_2} z \left(z - \frac{F_1}{F_0} \right) dz, \quad F_3 = \frac{1}{\eta} \int_{H_1}^{H_2} z dz. \quad (7.43)$$

Specifically for the gas film having a symmetry plane xy , applying the boundary conditions (7.31-7.36) and $H_2 = -H_1 = h$, $w_{s2} = -w_{s1} = w_s$, $u_{a1} = u_{a2} = u_a$ and $v_{a1} = v_{a2} = v_a$ in equation (7.42) yields the lubrication equation accounting for the rarefied flow effect:

$$\begin{aligned} & \frac{\partial}{\partial x} (h^3 \frac{\partial p}{\partial x}) + \frac{\partial}{\partial y} (h^3 \frac{\partial p}{\partial y}) + \\ & 3C_1 \lambda \left(\frac{\partial}{\partial x} (h^2 \frac{\partial p}{\partial x}) + \frac{\partial}{\partial y} (h^2 \frac{\partial p}{\partial y}) \right) + \\ & 3C_2 \lambda^2 \left(\frac{\partial}{\partial x} (h \frac{\partial p}{\partial x}) + \frac{\partial}{\partial y} (h \frac{\partial p}{\partial y}) \right) \\ & = 3\eta \left(w_s + \frac{\partial (hu_a)}{\partial x} + \frac{\partial (hv_a)}{\partial y} \right). \end{aligned} \quad (7.44)$$

The characteristic length of the rarefied flow in the gas film is $2h$, yielding

$$\text{Kn} = \frac{\lambda}{2h}. \quad (7.45)$$

The rarefied lubrication equation can therefore be rewritten as

$$\begin{aligned} & \frac{\partial}{\partial x} (h^3 \frac{\partial p}{\partial x}) + \frac{\partial}{\partial y} (h^3 \frac{\partial p}{\partial y}) + \\ & 6C_1 \text{Kn} h \left(\frac{\partial}{\partial x} (h^2 \frac{\partial p}{\partial x}) + \frac{\partial}{\partial y} (h^2 \frac{\partial p}{\partial y}) \right) + \\ & 12C_2 \text{Kn}^2 h^2 \left(\frac{\partial}{\partial x} (h \frac{\partial p}{\partial x}) + \frac{\partial}{\partial y} (h \frac{\partial p}{\partial y}) \right) \\ & = 3\eta \left(w_s + \frac{\partial (hu_a)}{\partial x} + \frac{\partial (hv_a)}{\partial y} \right). \end{aligned} \quad (7.46)$$

When $\text{Kn} = 0$, the rarefied lubrication equation (7.46) is reduced to the lubrication equation (7.22) without rarefied flow effect. The unified form (7.46) is implemented in FS3D for solving the flow in the gas layer in numerical simulations.

7.1.3 Calibration of the slip coefficients

Based on the Boltzmann equation, allowing the description of the rarefied flow effect over the entire Knudsen number range, Zhang et al. [71] derived an analytical solution for the lubricant pressure between two parallel cylinder plates approaching each other, where the ‘dragging effect’ of the boundary is not present. The pressure in the gas layer is given as:

$$p = \frac{3\eta_G w_s}{4h^3} (r^2 - R^2) \Delta^{-1}(\text{Kn}). \quad (7.47)$$

Here, the function $\Delta(\text{Kn})$ accounts for the rarefied flow effect and its value can be given for $\text{Kn} \ll 1$ as

$$\Delta(\text{Kn}) = 1 + 6.0966 \text{Kn}, \quad \text{Kn} \ll 1, \quad (7.48)$$

and for $\text{Kn} \geq 1$ as

$$\Delta(\text{Kn}) = 8.7583 \text{Kn}^{1.1551}, \quad \text{Kn} \geq 1. \quad (7.49)$$

Since equation (7.48) is only exact for $\text{Kn} \ll 1$ and equation (7.49) is exact for $\text{Kn} \geq 1$, the function $\Delta(\text{Kn})$ from (7.48) is extended up to $\text{Kn} = 1$ by using the expression

$$\Delta(\text{Kn}) = 1 + 6.0966\text{Kn} + c_1\text{Kn}^2 + c_2\text{Kn}^3. \quad (7.50)$$

The values of c_1 and c_2 are chosen such that the values and first-order derivatives of $\Delta(\text{Kn})$ in equations (7.49) and (7.50) are continuous at $\text{Kn} = 1$, resulting in

$$\Delta(\text{Kn}) = \begin{cases} 1 + 6.0966\text{Kn} + 0.9650\text{Kn}^2 + 0.6967\text{Kn}^3 & (\text{Kn} < 1) \\ 8.7583\text{Kn}^{1.1551} & (\text{Kn} \geq 1) \end{cases} \quad (7.51)$$

The same formulation of equation (7.47) can be derived (see the derivation in appendix B.1) from the rarefied lubrication equation (7.46) with

$$\Delta(\text{Kn}) = 1 + 6C_1\text{Kn} + 12C_2\text{Kn}^2. \quad (7.52)$$

The value of C_1 is calibrated by adapting the coefficient of Kn in equation (7.48), resulting in $C_1 = 1.0161$. The value of C_2 is calibrated by ensuring the same value of $\Delta(\text{Kn})$ computed by equation (7.49) and equation (7.52) at $\text{Kn} = 10$, yielding $C_2 = 0.0527$. The comparison between $\Delta^{-1}(\text{Kn})$ computed by means of equation (7.51) and equation (7.52) with calibrated coefficients is displaced in Figure 7.4, which shows overall good agreement. Considering equation (7.47), the pressure in the gas layer between two approaching parallel cylindrical planes decreases with increasing rarefaction effect.

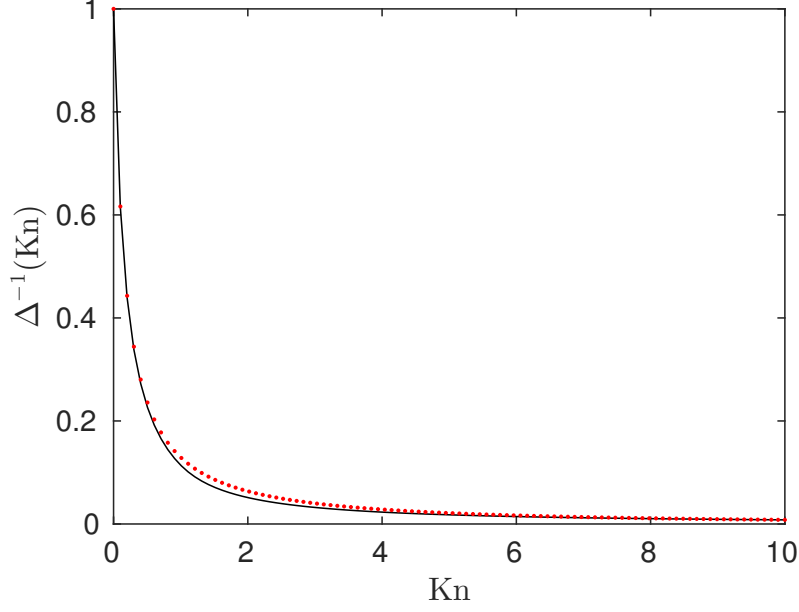


Figure 7.4.: $\Delta^{-1}(\text{Kn})$ computed by means of equation (7.51), represented by the black solid line and equation (7.52) with calibrated coefficients, represented by the red dotted line.

7.2 Implementation of the SGS model

7.2.1 Approximation of the quantities related to the interface

As the rarefied lubrication equation (7.46) is used to describe the flow in the gas film on the sub-grid scale, it is referred to as the sub-grid-scale (SGS) model in this thesis. In order to solve the SGS model numerically, the quantities h , u_a , v_a , w_s on the upper boundary of the gas layer are approximated based on the quantities obtained from the macroscopic simulation. It is easy to compute h through height functions, as it has been described in Chapter 3. The local interface height h with respect to the collision plane designates also where the interface velocities u_a and v_a are evaluated. The evaluations of u_a and v_a are conducted through a one-sided approximation:

$$u_a(i, j) = u_a^+ \frac{h - h^-}{h^+ - h^-} + u_a^- \frac{h^+ - h}{h^+ - h^-}, \quad (7.53)$$

$$v_a(i, j) = v_a^+ \frac{h - h^-}{h^+ - h^-} + v_a^- \frac{h^+ - h}{h^+ - h^-}, \quad (7.54)$$

where u_a^- and v_a^- are velocities evaluated at the center of the cell, where the interface designated by h is located. u_a^+ and v_a^+ are velocities of the neighboring cell centers on the side of the droplet. u_a^\pm and v_a^\pm are averaged from the velocities located on cell faces. h^\pm denotes the z -coordinate of the corresponding cell centers. A schematic illustration is shown in Figure 7.5.

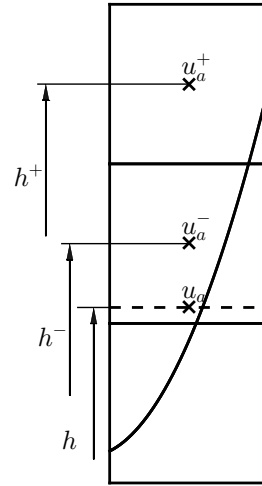


Figure 7.5.: Schematic illustration of the computation of the interface velocities in horizontal direction.

The resultant velocity w_s is computed by the variation rate of the local interface height within one time step Δt :

$$w_s = \frac{\partial h}{\partial t} \approx \frac{\Delta h}{\Delta t}. \quad (7.55)$$

The approximation of the interface velocity, especially u_a and v_a , is directly dependent on the velocity located at cell faces which are computed in macroscopic simulations. Therefore, the use of the SGS model is always combined with the employment of the balanced-CSF model to reduce the effect of the parasitic currents on the approximation accuracy of the interface velocity.

7.2.2 Equation system

The rarefied lubrication equation (7.46) is solved in a so-called lubrication region, which is defined as a region where the interface height h is smaller than or equal to a prescribed value h_{max} which is always a multiple of the equidistant cell width; see the schematic illustration in Figure 7.6. In the simulations in this thesis, if no further specification is given, the lubrication region is defined by prescribing $h_{max} = 1 \cdot \Delta x$. In this lubrication region, the rarefied lubrication equation (7.46) is discretized by means of the central differencing scheme (CDS). Outside the lubrication region, the pressure in the first cell-layer obtained from the DNS, i.e. from the macroscopic simulation, is used as a boundary condition. Accordingly, the boundary condition for the pressure is simply

$$p_b = p_{DNS}. \quad (7.56)$$

The equation system consisting of the rarefied lubrication equation (7.46) and the boundary condition (7.56) is built up for the whole collision plane, which is in rectangular form, and

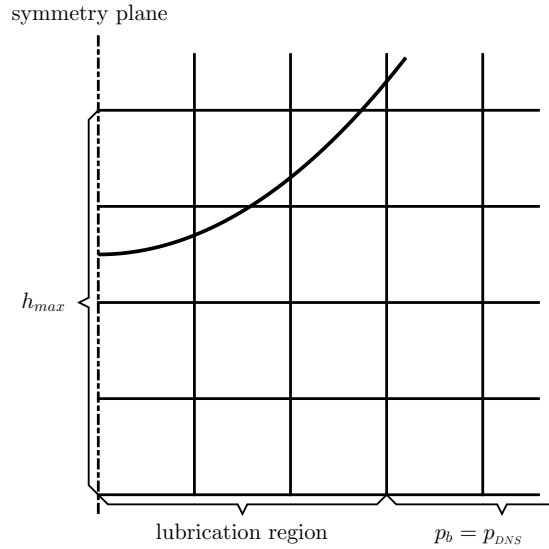


Figure 7.6.: Definition of the lubrication region.

solved by means of Gauss-Seidel iteration for each time step as long as the droplet enters the lubrication region. It should be noted that the lubrication region evolves due to the deformation of the colliding droplets.

7.3 Validation of the SGS model

The validity of the SGS model is assessed by means of two scenarios described below. The rarefaction effect is not considered, since proper analytical solutions and experimental measurements are absent. Nonetheless, when the gas layer thickness is constant, the lubrication equation with and without rarefaction effect differs only in the expression (7.52), the validity of which is assessed in Figure 7.4. The rigorous derivation of the rarefied lubrication equation gives us some confidence about its validity, as long as the SGS model without rarefaction is well validated.

7.3.1 Validation through the scenario of two approaching solid spheres

When two identical solid spheres move towards each other, a higher pressure compared to the surrounding is built up within the gas layer between the two solid spheres. Excluding the rarefied flow effect ($Kn = 0$), the lubricant pressure can be computed analytically and this is used to validate the SGS model. Considering the axis-symmetric nature of the scenario and the absent ‘dragging’ effect in the solid body motion, the lubrication equation is given in cylindrical coordinates as [71]

$$\frac{\partial}{\partial r} \left(h^3 \frac{\partial p}{\partial r} \right) + h^3 \frac{1}{r} \frac{\partial p}{\partial r} = 3\eta w_s. \quad (7.57)$$

For the gas film between the approaching spheres, h can be approximated [59] as $h = w_s t + h_0 + r^2/R$, where h_0 is the initial distance between the collision plane and the gas/solid interface at $r = 0$ and R is the radius of the spheres. Assuming zero ambient pressure, the pressure in the gas layer is given as

$$p = -\frac{3\eta R w_s}{4h^2}. \quad (7.58)$$

Specifically at $r = 0$, the pressure depending on time is given as

$$p(r = 0, t) = -\frac{3\eta R w_s}{4(w_s t + h_0)^2}. \quad (7.59)$$

In the numerical setup, a quarter of a sphere of $R = 0.1$ m moves with constant velocity $w_s = -1$ m/s towards the bottom wall, see Figure 7.7a. The initial minimal distance between the collision plane and the gas/solid interface is 0.01 m. The bottom and the top walls are set to zero pressure and homogeneous Neumann boundary condition for the velocity. The other four walls are set to slip boundary conditions. The gas, the viscosity of which is 10^{-3} Ns/m², moves with the same velocity of the solid sphere. The specific setup of the boundary conditions and zero relative motion between the sphere and the gas phase ensure that the sphere remains undeformed. In addition, the surface tension coefficient is set to zero to avoid the effect of parasitic currents. For the computation of the pressure field in the gas layer by means of the SGS model, this setup is equivalent to a solid sphere approaching its mirror image with constant velocity. The pressure depending on the evolution of h at $r = 0$ is computed numerically by means of the SGS model and compared with the corresponding analytical solution in Figure 7.7b. The computations show a very good agreement for all three used grid resolutions.

7.3.2 Validation through a virtual scenario based on a retracing ellipsoid

In order to account for the ‘dragging’ effect in the validation, a virtual scenario, illustrated in Figure 7.8, is considered. In the setup, an ellipsoid droplet is initialized described by

$$\frac{x^2}{(200\ \mu\text{m})^2} + \frac{y^2}{(200\ \mu\text{m})^2} + \frac{(z - 45\ \mu\text{m})^2}{(40\ \mu\text{m})^2} = 0. \quad (7.60)$$

Due to the surface tension force, the droplet retracts. Meanwhile, the interface drags the gas inwards due to the no-slip condition at the gas-liquid interface, which results in a pressure increase in the gas film between the droplet and the symmetry plane. The pressure field in the gas film in this case can be solved by means of a DNS. Since the solution of the SGS model is based on the quantities obtained from the DNS, the best possible result obtained from the SGS model is not supposed to be more accurate than the DNS result in the same simulation. Therefore, the DNS result with the finest grid resolution serves as a reference result for the validation of the SGS model.

The simulations are conducted in a $270 \times 270 \times 90\ \mu\text{m}^3$ box with three symmetry planes. The slip conditions are prescribed on the three symmetry planes. Zero pressure and homogeneous

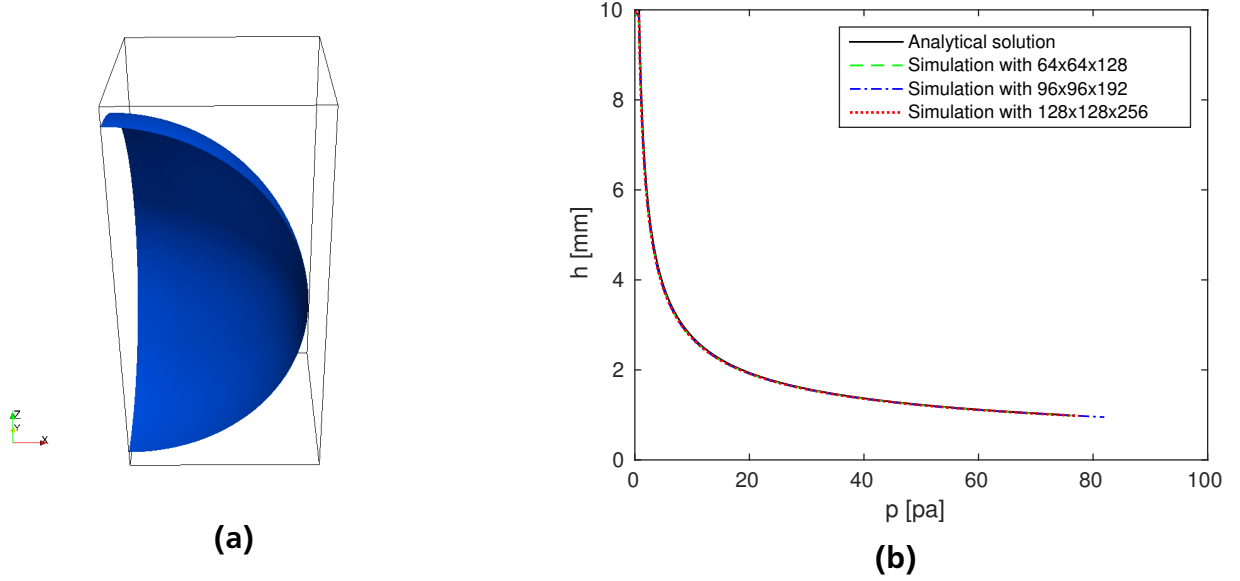


Figure 7.7.: (a) Setup of a solid sphere moving towards its mirror image. Domain size is $0.11 \text{ m} \times 0.11 \text{ m} \times 0.22 \text{ m}$. The lubrication region is prescribed by giving $h_{max} = 0.11 \text{ m}$. (b) Comparison between simulation results with three grid resolutions and the corresponding analytical solution.

Neumann boundary condition for the velocity are prescribed on all the other boundary planes. The material properties of the virtual system are: $\eta_L = 2.000 \times 10^{-3} \text{ Ns/m}^2$, $\rho_L = 1000 \text{ kg/m}^3$, $\eta_G = 1.000 \times 10^{-3} \text{ Ns/m}^2$, $\rho_G = 1.0 \text{ kg/m}^3$, $\sigma = 20.0 \times 10^{-3} \text{ N/m}$. The mean free path of the gas phase is set to zero so that the rarefied flow effect is also excluded in this case.

The pressure field is solved by means of the SGS model in a flat region of the gas layer, which guarantees the validity of the lubrication assumption. The maximum interface height of this lubrication region is set to $11.25 \mu\text{m}$. The pressure fields computed by the SGS model with three grid resolutions at $t = 0.25 \times 10^{-6} \text{ s}$ are plotted in Figure 7.9a, compared to the pressure field computed by means of the DNS with the finest resolution. One sees that as the grid is refined, the result approaches the ‘exact’ solution obtained from DNS. The mean absolute percentage error (MAPE) defined as

$$\text{MAPE} = \frac{100}{n} \sum_{i=1}^n \left| \frac{p_{SGS}(i) - p_{DNS}(i)}{p_{DNS}(i)} \right|, \quad (7.61)$$

is evaluated for the three used grid resolutions at five time instants, see Figure 7.9b. One sees that the results converge as the resolution is increased, however slower at later times. The slower convergence rate at later times is attributed to the accumulated parasitic currents, though the parasitic currents are relatively small while using the balanced-CSF model for the computation of the surface tension force.

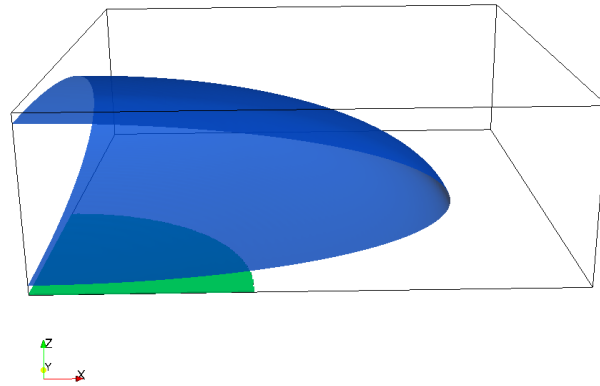


Figure 7.8.: Setup of a virtual scenario: retracting ellipsoid droplet over a symmetry plane. The SGS model is solved in the flat region represented by the green disc beneath the droplet (defined by giving $h_{max} = 11.25 \mu\text{m}$).

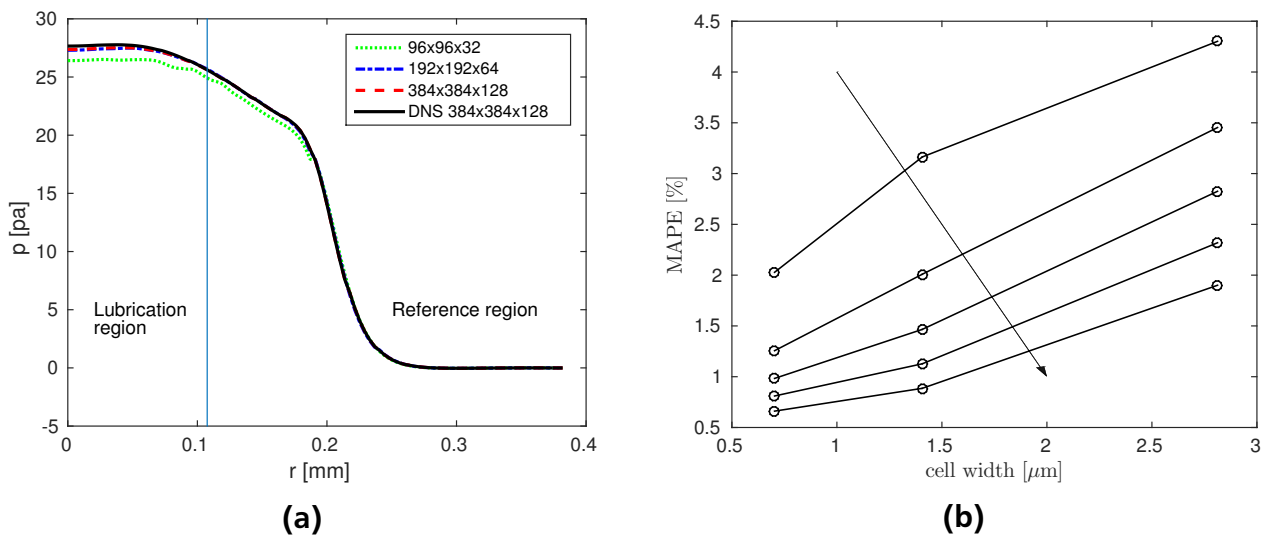


Figure 7.9.: (a) Comparison between the pressure fields computed by the SGS model and DNS with highest resolution at $t = 0.25 \times 10^{-6}$ s. (b) Mean absolute percentage error at five time instants. The arrow indicates the direction of the evolution. The time interval between the neighboring lines is $\Delta t = 0.05 \times 10^{-6}$ s. The lowest line corresponds to $t = 0.25 \times 10^{-6}$ s.

7.4 Integration of the SGS model into the main solver FS3D

The SGS model must be integrated into the main solver FS3D so that it can have an effect on the macroscopic simulation. The simulations conducted by means of the SGS model integrated into the main solver FS3D are called multi-scale simulations in this thesis. The integration of the SGS model is realized by applying the pressure field obtained from the SGS model as pressure boundary condition on the collision plane. In order to implement this coupling, the pressure in dummy cells within the lubrication region is modified to

$$p_{\text{dummy}} = 2p_{\text{SGS}} - p_1, \quad (7.62)$$

while solving the pressure Poisson equation. In equation (7.62), p_1 is the pressure in the cell-layer in the domain adjacent to the collision plane. In total, the pressure Poisson equation is solved two times within a time step. After the pressure Poisson equation is for the first time solved, the obtained pressure in the surrounding serves as a Dirichlet boundary condition for the SGS model. Applying the pressure in the gas layer obtained from the SGS model as boundary condition, the Poisson equation is solved again for obtaining the final pressure field.

In order to validate the integration, a test case of binary droplet collision with high gas viscosity and high gas density is considered. Due to the high viscosity and density, the gas layer is much thicker and is well resolved (i.e. by more than two cells) in the DNS with sufficiently high grid resolution in the very early stage of the collision, serving as a reference. The simulation by means of the SGS model is conducted with a lower resolution so that the flow in the gas layer can only be resolved by the SGS model. Detailed setups are listed in Table C.9 in appendix C. The pressure profile and the contour of the gas layer between the colliding droplets obtained from the multi-scale simulation are compared to the reference solution. As it is shown in Figure 7.10, the multi-scale simulation yields results that are in good agreement with the reference solution.

It was suggested by Mason et al. [33] that the integration of the pressure field obtained from a SGS model should be conducted by integrating the pressure field as a volumetric force in the domain as

$$\mathbf{f} = -p_{\text{SGS}}\mathbf{nA} \approx p_{\text{SGS}} \frac{\nabla f}{\|\nabla f\|} \|\nabla f\| = p_{\text{SGS}} \nabla f. \quad (7.63)$$

The equation (7.63) implies that the added volumetric force is the pressure force exerted from the gas film to the droplet. The motivation for this kind of integration seems to be that the pressure force exerted on the droplet should be added on the droplet surface because the pressure in the gas layer is not resolved by the macroscopic simulation. In fact, there is a contradiction in this kind of integration: if the pressure force exerted on the droplet should be added to the macroscopic simulation, then the reaction force, i.e. the pressure force exerted from the droplet to the gas layer should also be added. This is on one hand not done in the work of Mason et al. [33], on the other hand, if the reaction force is integrated by means of equation (7.63) with reversed sign on the right hand side, then there is no effect at all in the

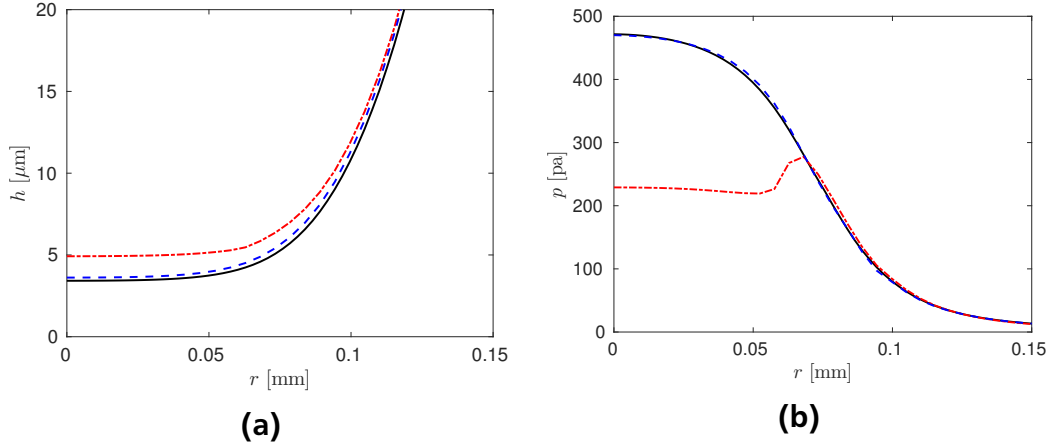


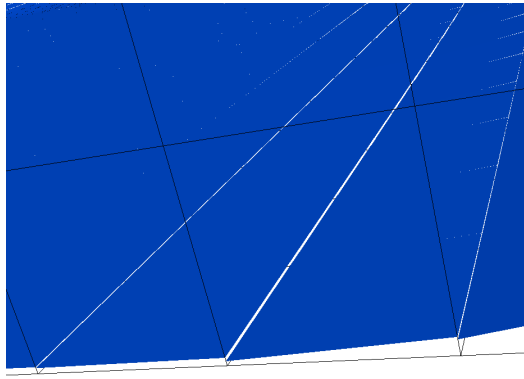
Figure 7.10.: Interface contours and pressure profiles at $t = 0.16$ ms. Solid black lines: reference solutions obtained from DNS conducted with a resolution of 128 cells per droplet diameter (cell width is $2.62 \mu\text{m}$). Blue dashed lines: solutions obtained from multi-scale simulation conducted with a resolution of 64 cells per droplet diameter (cell width is $5.24 \mu\text{m}$); the SGS model is integrated by modifying the pressure boundary condition. Red dash-dotted lines: solutions obtained from multi-scale simulation conducted with a resolution of 64 cells per droplet diameter (cell width is $5.24 \mu\text{m}$); the SGS model is integrated by adding a volumetric force. The simulations conducted do not account for the rarefaction effect.

macroscopic simulation. The key is that the volumetric force in interface cells cannot be added to a particular phase but can only be added to the field consisting a mixture of both phases due to the one-field formulation of the Navier-Stokes equations (2.18). Integrating the SGS model through adding the volumetric force, the same test case described in this section is computed. The disagreement between the obtained result and the reference solution shown in Figure 7.10 confirms that the integration of the SGS model in form of the volumetric force is not reasonable.

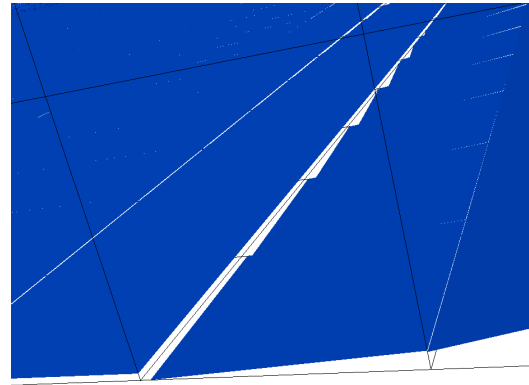
7.5 Prediction of the collision outcome in terms of coalescence versus bouncing

In order to facilitate a predictive simulation in terms of the prediction of coalescence versus bouncing, a coalescence criterion is needed. As it has been explained in the introduction, the competition between the resisting effect of the gas layer due to the high pressure built up and the intermolecular forces ultimately determines whether the droplets merge into a single droplet or bounce apart. It is therefore natural to account for the intermolecular force, i.e. Van der Waals force within this thesis, on the multi-scale computation aiming at a predictive simulation. According to Pan et al. [40], the effect of the Van der Waals force can be modeled as a negative pressure $p_{\text{vdW}} = -\frac{A_H}{6\pi(2h)^3}$, where A_H is the Hamaker constant, exerted on the surfaces of the droplets forming the boundary of the gas film. The negative pressure can be integrated in the momentum equation as a volumetric force given as

$$\mathbf{f}_{\text{vdW}} = -p_{\text{vdW}}\mathbf{nA} \approx p_{\text{vdW}} \frac{\nabla f}{\|\nabla f\|} \|\nabla f\| = p_{\text{vdW}} \nabla f = -\frac{A_H}{6\pi(2h)^3} \nabla f. \quad (7.64)$$



(a)



(b)

Figure 7.11.: (a) PLIC surfaces over collision plane; coalescence has not occurred yet. (b) Intersection of PLIC surfaces with the collision plane defining coalescence.

Having accounted for the Van der Waals force, the coalescence is activated in the simulation in case of two possible occurrences serving as coalescence criteria:

- The minimum thickness of the gas layer is smaller than the threshold for distinguishing liquid and gas (called zero gas film thickness in algorithm tolerance in the following): if $1 - f < 10^{-6}$ is identified in the cell-layer adjacent to the collision plane, the cell is considered containing only the liquid phase and coalescence can be perceived. Note that the minimum thickness of the gas layer before possible coalescence is determined by f in the first cell-layer, since the gas film thickness is thinner than one cell.
- A PLIC-surface intersects the collision plane, as suggested by Jiang and James [24]. The PLIC-surfaces suggesting ‘coalescence’ or ‘not coalescence’, respectively, are exemplarily shown in Figure 7.11.

Mason et al. [33] proposed that 40 nm can be defined as a critical value for coalescence. This critical value is abandoned in this thesis, since there is no convincing evidence for the existence of this general critical value in binary droplet collisions.

7.5.1 Preliminary results of predictions

The setups of the simulations aiming at the prediction of the collision outcomes are based on the experimental work of Pan et al. [40], who showed that the critical Weber number (We_b) between sector II and III in the collision diagram for head-on collision of tetradecane droplets (approximately same Ohnesorge number $Oh = 0.028$ is held) in air under standard conditions is between 9.33 and 13.63. The comparisons between the experiments and the simulation results with prescribed collision outcomes without using the SGS model are shown in Figure 4.8 and 4.9, yielding very good agreement. The simulations with the same setups (prescribed collision outcome) and in addition by means of the integrated SGS model yield indistinguishable collision

Mesh	We = 7.77	9.59	11.61	13.63	16.21	18.80
96 ³	C	C	C	C	C	C
128 ³	C	C	C	C	C	C
192 ³	B	C	C	C	C	C
256 ³	B	B	B	C	C	C

Table 7.1.: Prediction of the collision outcome in terms of coalescence (denoted as C) and bouncing (denoted as B).

processes compared to the results obtained without using the SGS model on the macroscopic scale. Therefore, the illustration of the collision processes computed by means of the integrated SGS model is omitted. The focus is the prediction of the critical Weber number We_b .

Around $We = 13.63$, the Weber number in the conducted simulations is successively changed by varying the collision velocity, while keeping the same Ohnesorge number ($Oh = 0.028$) and leaving all the other setups untouched. The numerical setups for the case of $We = 13.63$ are listed in Table C.10 in appendix C. The predicted collision outcomes in terms of bouncing/coalescence using the intersection of PLIC surfaces as coalescence criterion are summarized in Table 7.1. The results show that at relatively low grid resolutions, the collision outcome bouncing does not emerge even at lower Weber numbers. At higher grid resolutions, the collision outcome can be both bouncing or coalescence. However, the critical Weber number is strongly dependent on the grid resolution. Seemingly, the predicted Weber number increases with increasing grid resolution.

Using zero gas film thickness in algorithm tolerance as coalescence criterion, all the simulations mapped in Table 7.1 yield bouncing. The evolutions of the minimum thickness of the gas layer in the case of $We = 13.63$, the collision outcome of which is expected to be coalescence, are shown in Figure 7.12. The minimum thicknesses obtained with used resolutions are all so high that the Van der Waals forces are too small to cause coalescence. This issue is further addressed in the following section.

7.5.2 Modified f -transport

The transport of the f -field determines directly whether the coalescence occurs in combination with the criterion of zero gas film thickness in algorithm tolerance, since the film thickness in the simulations is calculated by means of the height function which is a function of f ; see Figure 7.13. It is shown in Chapter 6 that the velocity profile in the gas layer is parabolic and can be much larger than the velocity in the droplet near the interface. However, the thickness of the gas film is on the sub-grid scale and only averaged velocities are computed and stored at the center of the cell faces, which are used for solving the transport equation (3.3) determining the f -values, yielding inaccurate transport of the f -field. Based on this fact, further attempts have been conducted by means of modifying the velocity for the transport of the f -field in the

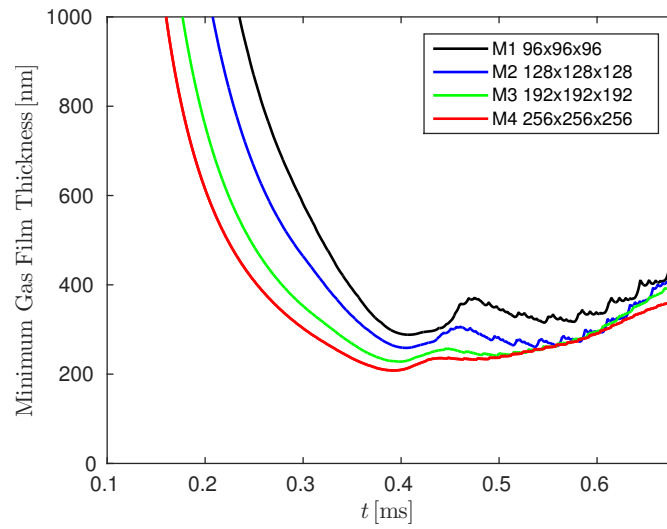


Figure 7.12.: Evolution of the minimum thickness of the gas layer in the case of $We = 13.63$.

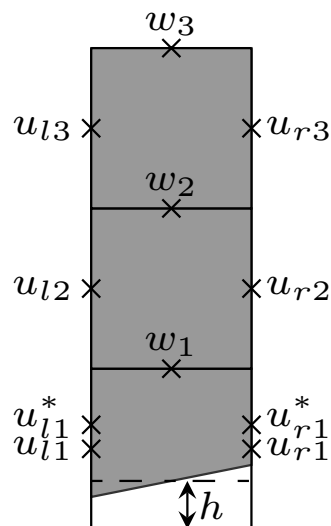


Figure 7.13.: Schematic illustration of the modification of the velocity field for the transport of the f -field. u_{l1}^* and u_{r1}^* are located at the position which is computed based on the averaged gas layer thickness at the cell faces.

first cell-layer, in order to facilitate coalescence in combination with the criterion of zero gas film thickness in algorithm tolerance.

The first attempt is based on the employment of the velocity field in the gas layer which can be obtained from the SGS model: Applying the pressure field obtained from the SGS model and integrating equation (7.37) and (7.38) over the thickness of the gas film yield numerical solution of the average velocity in the gas layer. Using this averaged velocity in the gas layer for transporting the gas phase (by reversing f) yields, however, only bouncing in all conducted simulations.

Further attempts are based on direct correction of the velocity field for the transport of the f -field. Instead of the averaged velocity located at the centers of the cell surfaces u_{l1} and u_{r1} , the averaged velocity of the liquid phase in the first cell-layer u_{l1}^* and u_{r1}^* is used for solving the transport equation (3.3); see Figure 7.13. The transport velocity in the vertical direction is also modified in certain cases (see Table 7.2). The corresponding modifications and the resulting collision outcomes are listed in Table 7.2. Comparing the four attempts and collision outcomes, all results change from bouncing to coalescence as long as the interpolated velocity w_1 , which is located in the liquid phase, is used for solving the transport equation (3.3), implying that the velocity in the vertical direction for the transport of f is the key to the collision outcome. The SGS model in this thesis has been able to describe the flow in the gas layer. In order to achieve predictive simulations in terms of the prediction of the collision outcome bouncing versus coalescence with satisfied accuracy, the flow in the droplet near the interface has to be understood in detail in future work.

7.6 Rarefaction effect

Qian and Law [45] showed in their experimental work that the area of the bouncing sector in the collision diagram expands with elevated gaseous pressure. Zhang and Law [71] argued that the gas possesses a higher density with elevated pressure which is then harder to be squeezed out, leading to higher pressure buildup in the gas layer and reduced possibility of coalescence. By the same token, the collision outcome tends to be coalescence at reduced ambient pressure.

The viscosity of the gas remains fairly constant in a large range of pressure variation [45]. As the pressure variation also affects the mean free path of the gas molecules, the rarefaction effect is examined based on the case of $We = 13.63$ described in section 7.5. The pressure field and gas layer thickness at $t = 0.368$ ms obtained from the simulation with enlarged mean free path $\lambda = 680$ nm are plotted in Figure 7.14, compared to the reference case where the mean free path is $\lambda = 68$ nm. In both simulations, the droplet diameter is resolved by 128 cells. One observes that the pressure in the gas layer with the enlarged mean free path is significantly smaller than in the reference case, leading to a smaller gas film thickness. This observation implies that the binary droplet collision in gas environment consisting of gas molecules having larger mean free path tends to yield coalescence easier.

attempts	collision outcome
<ul style="list-style-type: none"> • Extrapolating u_1^* with u_2 and u_3 • Transporting f with u_{l1}^*, u_{r1}^* and w_1 	all bouncing
<ul style="list-style-type: none"> • Interpolating u_1^* with u_1 and u_2 • Transporting f with u_{l1}^*, u_{r1}^* and w_1 	all bouncing
<ul style="list-style-type: none"> • Extrapolating w_1 with w_3 and w_2 • Extrapolating u_1^* with u_2 and u_3 • Transporting f with u_{l1}^*, u_{r1}^* and extrapolated w_1 	all coalescence
<ul style="list-style-type: none"> • Extrapolating w_1 with w_3 and w_2 • Interpolating u_1^* with u_1 and u_2 • Transporting f with u_{l1}^*, u_{r1}^* and extrapolated w_1 	all coalescence

Table 7.2.: Attempts on the predictive simulations based on the corrections of the velocity for solving the transport equation (3.3). The subscripts l and r are omitted in some notations for simplicity.

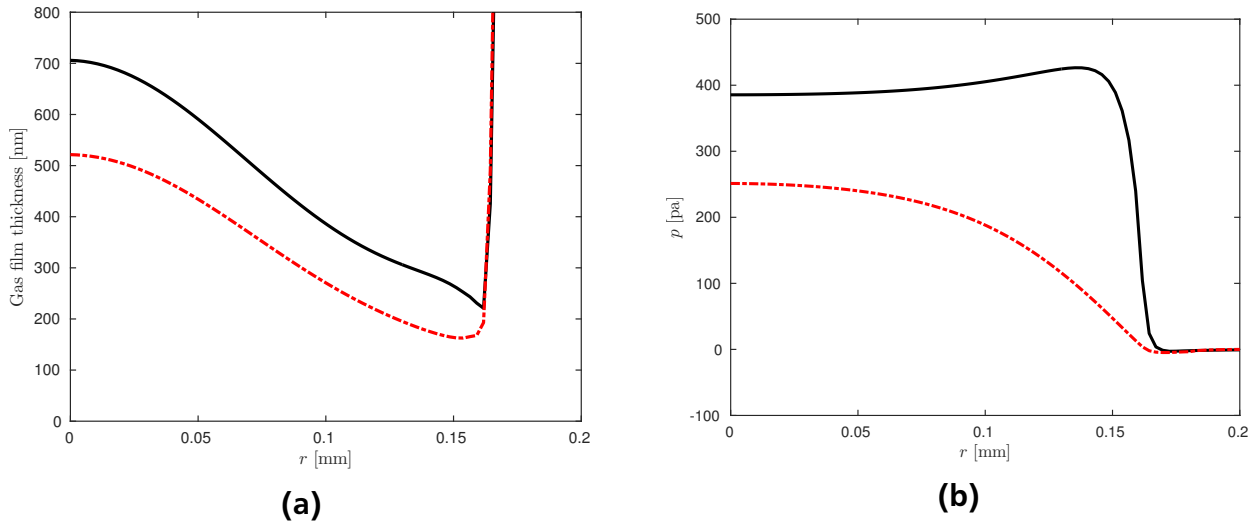


Figure 7.14.: Gas film thickness and pressure profile at $t = 0.368$ ms when coalescence is supposed to occur in the experiment [40]. Black solid lines: reference case with $\lambda = 68$ nm. Red dashed lines: results with increased mean free path of the gas molecules $\lambda = 680$ nm.

7.7 Role of the compressibility

The derivation of the SGS model solving the flow in the gas film is based on the assumption of incompressibility. If the pressure elevation in the gas layer is comparable to the ambient pressure, the gas flow should be considered as compressible [71]. In all the conducted numerical simulations, the pressure elevation in the gas layer does not exceed the order of 1000 pa (compared to zero pressure at the outer boundary of the computational domain) as it is exemplarily shown in Figure 7.14, which is significantly smaller than the pressure in standard ambient conditions (10^5 pa). Therefore, the incompressible flow assumption is valid in the gas film.

8 Summary and Outlook

8.1 Summary

This thesis has been driven by the realization of the prediction of the collision outcome in terms of bouncing versus coalescence and in terms of the onset of spatter as well as the prediction of the size spectrum of the secondary droplets resulting from the spatter phenomenon. An important task has been the deeper understanding of phenomena related to the mechanisms that decide the collision outcomes, especially the mechanism of the rim instability of a collision complex in high energetic collisions. Multi-scale simulations have been performed for the prediction of the transition between bouncing and coalescence. Based on further numerical investigations, it has been revealed that the Rayleigh-Plateau instability pattern dominates the rim instability over a long time span, which is very valuable for the establishment of analytical models used for predicting the onset of spatter and the spectrum of secondary droplets ejected from the unstable rim.

The thin liquid lamella emerging at high energetic collisions ruptures in the numerical simulations due to the artificial interaction while computing the surface tension force of both sides of the lamella, which results in unphysical collision processes. The lamella stabilization algorithm developed by Focke and Bothe [17], which prevents the lamella rupture by a correction of the computation of the surface tension force in the lamella region, has been improved in terms of a more accurate identification of the lamella region. The improved lamella stabilization algorithm has been validated by comparing the simulation results to experiments, which yields very good agreement. A domain adjustment technique, which adjusts the computational domain to the deformation of the collision complex successively, has been developed and employed in the simulations of spatter, in order to reduce the computational effort.

By means of a properly chosen white noise disturbance, the rim instability is triggered and excellent agreement between the simulation result and the experiment has been achieved for water droplet collision at $We = 442.3$. It has also been shown that white noise disturbances in different strength result in obviously different collision processes in the numerical simulations, which implies that the ubiquitous disturbances presented in the real world should also affect the collision outcome at high Weber numbers, though it has not been mentioned by experimenters. Although the agreement between simulations and experiments is less good at higher Weber numbers, the breakup mechanism of the rim at an extremely high Weber number ($We = 1520$) has been shown not to be as different as at relatively lower Weber numbers in terms of whether the rim is completely detached from the liquid film before the formation of secondary droplets, which is in disagreement with the conclusion of Kuan et al. [27].

Based on the quantifications of the simulation results of the case $We = 442.3$, which is in best agreement with the corresponding experiment, the mechanism of the rim instability is investi-

gated in depth. The development of the rim instability has been considered as the amplification of a signal through an amplification system that is subdivided into three sequential connected subsystems (initial phase, linear phase and non-linear phase), according to whether the collision complex rim and the neck of fingers can be identified by the algorithm. In the initial phase, the rim acceleration and rim oscillation have been identified for the first time. The analysis in the initial phase does not confirm that the RT instability pattern is dominant at the early stage of the rim instability as stated in [27], though the results approve that the rim deceleration provides a small boost to amplitude growth in regions of small modes as was stated in [1]. In the linear phase, strong evidence has been found for the statement that the PR instability pattern dominates the rim instability: the magnification of the amplitudes of instability modes can be well predicted by the PR-based theory over a long time span. In the non-linear phase, the evolution of the pressure field and the velocity field in the rim shows that the Rayleigh-like pattern is also present.

Also based on the case of $We = 442.3$, the viscosity effect is investigated numerically by varying solely the liquid viscosity with all other setups untouched. It has been shown that the viscosity has a significant effect on the rim instability only when it is high enough. The analysis has been able to reveal that the droplet viscosity influences the development of the rim instability mainly through varying the geometrical evolution of the rim. In addition, the PR instability pattern has been found to dominate the rim instability in the linear phase in a very large Reynolds number range.

The artificial interaction related to the computation of the surface tension force of a fluid lamella is also present in the simulation of possible coalescence, which makes a predictive simulation in terms of whether the collision outcome is ‘bouncing’ or ‘coalescence’ difficult. As a result of the interaction between the approaching droplet interfaces, the colliding droplets will always coalesce in standard VOF-simulations. Stabilizing the gas film between the colliding droplets by temporarily removing the symmetric counterpart of one droplet while computing the surface tension force, the bouncing phenomenon can also be reproduced, giving very good agreement with the experiment. In the simulation of coalescence, the coalescence is first suppressed by the stabilization technique. At the instant of possible coalescence, which is obtained from the experimental observation, this stabilization of the gas film is discarded so that coalescence then occurs. The collision process yielding coalescence has also been reproduced, which is in good agreement with experiments. However, the simulations have not been able to be predictive in the sense that the collision outcome has to be prescribed so far. In order to facilitate a predictive simulation, a concept for multi-scale simulations is designed, containing three elements: (1) a SGS model solving the flow in the gas layer which is on the sub-grid scale. (2) the coalescence is first suppressed. (3) the coalescence is imposed when a numerical coalescence criterion is fulfilled.

Based on the classical lubrication theory, the SGS model has been derived, which accounts for the rarefaction effect by introducing a slip between the gaseous molecules and the gas-liquid interface. The SGS model has been implemented in FS3D and validated by means of a series of setups. It has been found that the integration of the SGS model by adding a volumetric force active for interface cells suggested in [33] results in an inappropriate coupling. In contrast,

applying the pressure field obtained from the SGS model as a pressure boundary condition on the collision plane yields more reasonable results, and is therefore used to conduct the multi-scale simulations.

Employing the first intersection of the PLIC-surfaces with the collision plane as coalescence criterion, the simulation has been able to yield both coalescence and bouncing. However, the predicted critical Weber number is strongly dependent on the grid resolution, which restricts its application. Using the zero gas film thickness in algorithm tolerance as coalescence criterion, the simulation results are all bouncing. A 2D-simulation with high resolution shows that the drainage velocity in the gas film can be much higher than the velocity in the liquid phase near interface. Based on this observation, various corrections of the velocity for the transport of the f -values in the first cell-layer adjacent to the collision plane have been conducted, which yielded all coalescence or all bouncing.

The rarefaction effect has been qualitatively investigated by comparing the gas film thickness and the pressure field in the gas layer between the case with enlarged mean free path of the gaseous molecules and a reference case. The results imply that binary collision in gas environment consisting of gas molecules having larger mean free path tends to yield coalescence.

8.2 Outlook

The rim instability has been numerically investigated in three phases subdivided in terms of the geometrical characteristics of the unstable rim. It has been revealed that the rim instability in the linear phase can be predicted by the PR instability theory for a very large Reynolds number range.

The input signal of the linear unstable phase is the output signal of the initial phase. In fact, we do not know much about the instability mechanism in the initial stage due to absent images from the experiment and the relatively poor local grid resolution in the simulations for resolving the rim geometry in this early stage. It is supposed that the toroidal rim emerging at the end of this initial stage results from the retraction of the frontier of the expanding liquid film due to the surface tension force and that the ratio between the film thickness and the rim radius is relatively large in the initial phase. Therefore, the film thickness should play a more important role in the rim instability in this phase. Modeling the instability growth on a liquid cylinder combined by a liquid film, Roisman et al. [54] showed that the presence of the liquid film stabilizes the rim instability. Zhang et al. [70] stated that the transition from rim to film also slows the growth of the rim instability. Numerical simulations with much higher grid resolutions focusing on this initial stage are recommended to be conducted in the future. In addition, the rim instability in this initial phase can be numerically studied by means of a simplified geometry consisting of a rim connected to a liquid film. A preliminary simulation showing the rim instability in this simplified geometry is presented in Figure 8.1. Further studies are needed in the future.

In the linear phase, future work should be focused on the modeling of the evolution of the rim geometry without instability depending on the Reynolds number and Weber number, since the evolution of the rim geometry unambiguously decides the characteristics of the amplification system in the linear phase. It has been shown that varying the Reynolds number has a significant

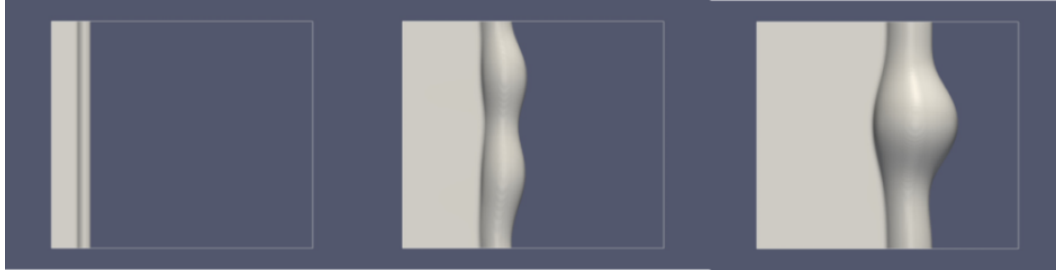


Figure 8.1.: Modeling the rim instability in the initial phase based on a cylindrical rim connected with a liquid film with inflow coming from the left wall.

effect on the evolution of the rim geometry at low Reynolds numbers and has negligible effect at high Reynolds numbers while holding the Weber number constant. The effect of the Weber number should also be investigated in detail in future work. The modeling of the evolution of the rim geometry, which is dependent on Reynolds number and Weber number, can be facilitated by axis-symmetric simulations, which reduce the computational efforts and enable simulations at much higher Weber numbers.

It is difficult to quantify the evolution of the rim instability in the nonlinear phase. However, modeling the evolution of rim geometry in the linear phase and its initial signal properly, applying the PR theory to the rim and setting a threshold for the output signal of the linear phase, the prediction of the collision outcome in terms of the size spectrum of the secondary droplets will be possible.

Considering the whole collision process as a signal amplification system, it is reasonable to perceive that the collision outcome should be able to be manipulated by controlling the input signal in form of oscillation of the colliding droplets or fluctuation in the environment or in the whole liquid/gas system. Due to the importance of the initial disturbance on the onset of the instability, the modeling of the boundary curve between IV-VI on the collision diagram should also include an appropriate quantification of the initial disturbance, which has not been considered in previous experimental works. Furthermore, the knowledge concerning the rim instability in the context of binary droplet collisions can be transmitted to the investigation of the rim instability in other contexts, i.e. the collision of a droplet onto a liquid film or onto a solid substrate.

In order to facilitate a predictive simulation in terms of the prediction of ‘bouncing’ versus ‘coalescence’, the f -transport has to be accurately computed. This can be achieved by means of mesh grading which significantly refines the grid resolution near the collision plane. The flow field in the droplet near the colliding interface should be investigated in detail which should be valuable to enhance the modeling on the sub-grid scale. Furthermore, it is recommended that the Volume-averaged VOF method [69], which accounts for the velocity difference of both phases in one cell, should be implemented to increase the accuracy of the f -transport. The velocity field obtained from the developed SGS model can be applied in principle in the Volume-averaged VOF method.

A Simulations of Spatter Conducted at ITLR of the University of Stuttgart

Head-on collisions of water droplets with $We = 805.2$ and $Re = 6370.0$ (same case as described in Chapter 5) have been simulated in ITLR of University Stuttgart by means of another version of FS3D integrated with the same lamella stabilization algorithm as described in Chapter 4, see the simulation results in Figure A.1. The domain adjustment technique is not employed. In the reference cases in Figure A.1, the relative grid resolution is the same as it is in Chapter 5.

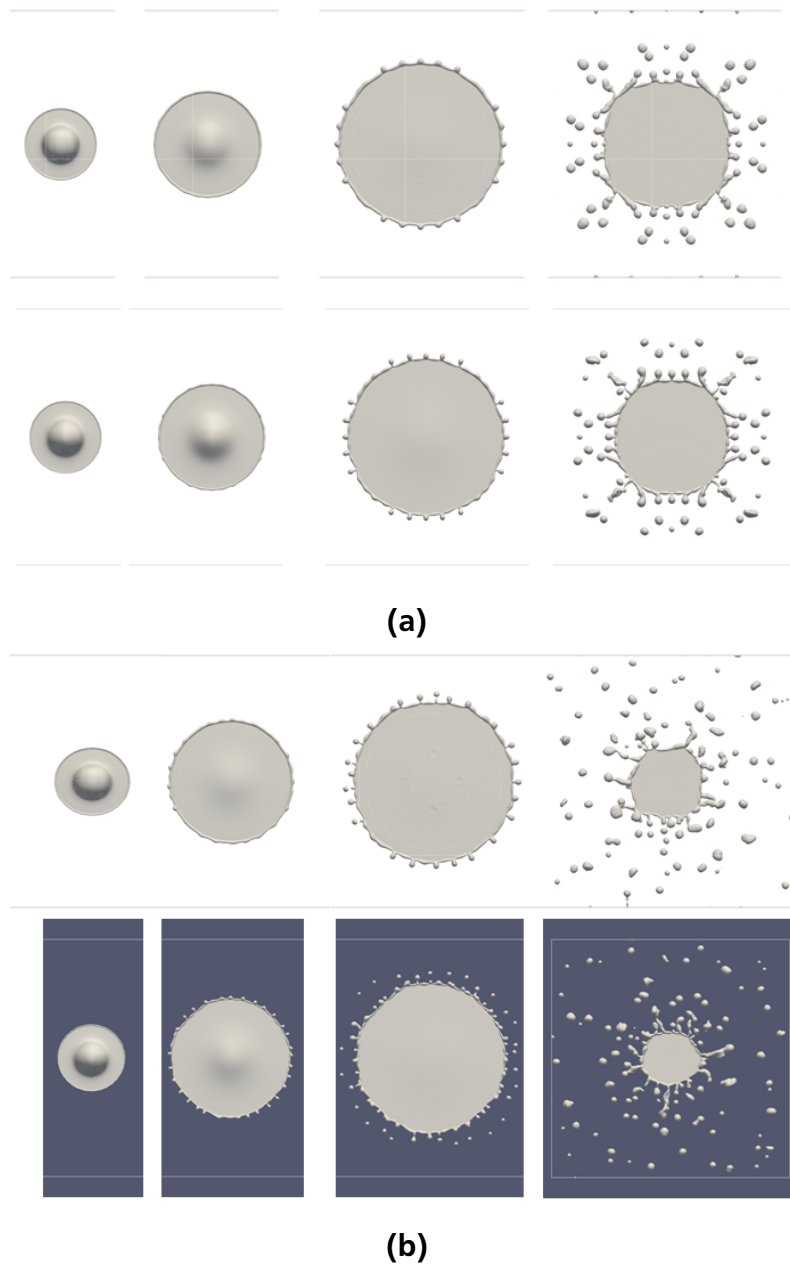


Figure A.1.: Evolutions of the collision complex shapes obtained from the numerical simulations conducted in ITLR of University Stuttgart within collaborate work [31]. Dimensionless time from the left to the right is 0.78, 2.34, 4.68, 7.8, 15.6. (a) simulation results without initial disturbance. (b) simulation results with an initial disturbance $\Delta U = 1\%$. The images in the upper row of both (a) and (b) correspond to the same relative grid resolution as used in Chapter 5. The images in the lower row of both (a) and (b) correspond to the doubled grid resolution.

B Lubrication Equation in Cylindrical Coordinates

B.1 Transformation between Cartesian coordinates and polar coordinates

The transformation from polar coordinates (r, α) to Cartesian coordinates (x, y) is simply

$$\begin{cases} x = r \cdot \cos\alpha \\ y = r \cdot \sin\alpha. \end{cases} \quad (\text{B.1})$$

Then the corresponding transformation for the derivatives is given as

$$\begin{pmatrix} \frac{\partial}{\partial x} \\ \frac{\partial}{\partial y} \end{pmatrix} = \begin{pmatrix} \cos\alpha & -\frac{\sin\alpha}{r} \\ \sin\alpha & \frac{\cos\alpha}{r} \end{pmatrix} \begin{pmatrix} \frac{\partial}{\partial r} \\ \frac{\partial}{\partial \alpha} \end{pmatrix}. \quad (\text{B.2})$$

B.2 Lubrication equation in cylindrical coordinates

Making use of the transformation equation (B.2), the separate terms of the lubrication equation without the rarefaction effect (7.22) are given as following:

$$\begin{aligned} \frac{\partial}{\partial x} \left(h^3 \frac{\partial p}{\partial x} \right) &= \frac{\partial}{\partial x} \left(h^3 \left(\cos\alpha \frac{\partial p}{\partial r} - \frac{\sin\alpha}{r} \frac{\partial p}{\partial \alpha} \right) \right) \\ &= 3h^2 \frac{\partial h}{\partial r} \left(\cos^2\alpha \frac{\partial p}{\partial r} - \frac{\sin\alpha \cos\alpha}{r} \frac{\partial p}{\partial \alpha} \right) + \\ &\quad h^3 \left(\cos^2\alpha \frac{\partial^2 p}{\partial r^2} + \frac{\sin\alpha \cos\alpha}{r^2} \frac{\partial p}{\partial \alpha} \right) - \frac{\sin\alpha \cos\alpha}{r} \frac{\partial^2 p}{\partial \alpha \partial r} + \\ &\quad 3h^2 \frac{\partial h}{\partial \alpha} \left(\frac{-\sin\alpha \cos\alpha}{r} \frac{\partial p}{\partial r} + \frac{\sin^2\alpha}{r^2} \frac{\partial p}{\partial \alpha} \right) + \\ &\quad h^3 \left(\frac{\sin^2\alpha}{r} \frac{\partial p}{\partial r} - \frac{\sin\alpha \cos\alpha}{r} \frac{\partial^2 p}{\partial \alpha \partial r} + \frac{\sin\alpha \cos\alpha}{r^2} \frac{\partial p}{\partial \alpha} + \frac{\sin^2\alpha}{r^2} \frac{\partial^2 p}{\partial \alpha^2} \right), \end{aligned} \quad (\text{B.3})$$

$$\begin{aligned} \frac{\partial}{\partial y} \left(h^3 \frac{\partial p}{\partial y} \right) &= \frac{\partial}{\partial x} \left(h^3 \left(\sin\alpha \frac{\partial p}{\partial r} + \frac{\cos\alpha}{r} \frac{\partial p}{\partial \alpha} \right) \right) \\ &= 3h^2 \frac{\partial h}{\partial r} \left(\sin^2\alpha \frac{\partial p}{\partial r} + \frac{\sin\alpha \cos\alpha}{r} \frac{\partial p}{\partial \alpha} \right) + \\ &\quad h^3 \left(\sin^2\alpha \frac{\partial^2 p}{\partial r^2} - \frac{\sin\alpha \cos\alpha}{r^2} \frac{\partial p}{\partial \alpha} + \frac{\sin\alpha \cos\alpha}{r} \frac{\partial^2 p}{\partial \alpha \partial r} \right) + \\ &\quad 3h^2 \frac{\partial h}{\partial \alpha} \left(\frac{\sin\alpha \cos\alpha}{r} \frac{\partial p}{\partial r} + \frac{\cos^2\alpha}{r^2} \frac{\partial p}{\partial \alpha} \right) + \\ &\quad h^3 \left(\frac{\cos^2\alpha}{r} \frac{\partial p}{\partial r} + \frac{\sin\alpha \cos\alpha}{r} \frac{\partial^2 p}{\partial \alpha \partial r} - \frac{\sin\alpha \cos\alpha}{r^2} \frac{\partial p}{\partial \alpha} + \frac{\cos^2\alpha}{r^2} \frac{\partial^2 p}{\partial \alpha^2} \right), \end{aligned} \quad (\text{B.4})$$

$$\begin{aligned}\frac{\partial hu_a}{\partial x} &= \cos\alpha \frac{\partial hu_a}{\partial r} - \frac{\sin\alpha}{r} \frac{\partial hu_a}{\partial \alpha} \\ &= \cos^2 \frac{\partial hu_{ra}}{\partial r} - \frac{\partial hu_{ra}}{\partial \alpha} \sin\alpha \cos\alpha,\end{aligned}\tag{B.5}$$

$$\begin{aligned}\frac{\partial hv_a}{\partial y} &= \sin\alpha \frac{\partial hv_a}{\partial r} + \frac{\cos\alpha}{r} \frac{\partial hv_a}{\partial \alpha} \\ &= \sin^2 \frac{\partial hu_{ra}}{\partial r} + \frac{\partial hu_{ra}}{\partial \alpha} \sin\alpha \cos\alpha.\end{aligned}\tag{B.6}$$

Inserting equations (B.3) (B.4) (B.5) (B.6) into the lubrication equation (7.22) gives the lubrication equation in cylindrical coordinates:

$$\frac{\partial}{\partial r} \left(h^3 \frac{\partial p}{\partial r} \right) + \frac{1}{r^2} \frac{\partial}{\partial \varphi} \left(h^3 \frac{\partial p}{\partial \varphi} \right) + h^3 \frac{1}{r} \frac{\partial p}{\partial r} = 3\eta \left(w_a + \frac{\partial hu_r}{\partial r} \right).\tag{B.7}$$

B.3 Pressure in the gas layer between two approaching parallel plates in cylindrical form

The derivatives in terms of φ in the lubrication equation in cylindrical coordinates (B.7) vanish in axis-symmetric problems. For the the gas flow between two approaching parallel plates in cylindrical form with zero surrounding pressure, applying the boundary conditions to equation (B.7) yields the pressure in the gas layer:

$$p(r) = \frac{3\eta_G w_s}{4h^3} (r^2 - R^2),\tag{B.8}$$

where R is the radius of the cylindrical plates, w_s is the velocity of one plate with respect to the symmetry plane and h is the distance between one plate and the symmetry plane.

In case of two parallel plates due to the parallelism, the only difference between the lubrication equations with (7.22) and without the rarefaction effect (7.46) lies on the reciprocal value of the coefficient

$$\Delta(\text{Kn}) = 1 + 6C_1 \text{Kn} + 12C_2 \text{Kn}^2.\tag{B.9}$$

Therefore, the pressure in the gas film between two parallel approaching cylindrical plates considering the rarefaction effect is given as

$$p(r) = \frac{3\eta_G w_s}{4h^3} (r^2 - R^2) \Delta^{-1}(\text{Kn}).\tag{B.10}$$

C Setups

Domain size:	$800 \times 800 \times 800 \mu\text{m}$
Grid:	$128 \times 128 \times 128$
Number of the employed symmetry planes:	3
Initial position of the droplet:	(0, 0, 0)
Droplet diameter:	$400 \mu\text{m}$
Initial velocity:	0.5 m/s
Disperse phase:	$\eta_l = 1.0 \cdot 10^{-3} \text{ Pa s}, \rho_f = 1000 \text{ kg/m}^3$
Continuous Phase:	$\eta_g = 0.0182 \cdot 10^{-3} \text{ Pa s}, \rho_g = 1.19 \text{ kg/m}^3$
Surface tension:	$50 \cdot 10^{-3} \text{ N/m}$

Table C.1.: Setup for the simulation of droplet oscillation with integral surface energy output; Chapter 3.6

Domain size:	$720 \times 720 \times 240 \mu\text{m}$
Grid:	$288 \times 288 \times 96$
Number of the employed symmetry planes:	3
Initial distance of droplet centers:	$231.6 \mu\text{m}$
Droplet diameter:	$231.6 \mu\text{m}$
Relative velocity:	5.6 m/s
Disperse phase:	$\eta_l = 2.39 \cdot 10^{-3} \text{ Pa s}, \rho_f = 784.5 \text{ kg/m}^3$
Continuous Phase:	$\eta_g = 0.0182 \cdot 10^{-3} \text{ Pa s}, \rho_g = 1.19 \text{ kg/m}^3$
Surface tension:	$21.4 \cdot 10^{-3} \text{ N/m}$

Table C.2.: Setup for the simulation of the case $We = 268$; Chapter 4.1.

Domain size:	$750 \times 750 \times 250 \mu\text{m}$
Grid M1:	$192 \times 192 \times 64$
M2:	$288 \times 288 \times 96$
M3:	$384 \times 384 \times 128$
Number of the employed symmetry planes:	3
Initial distance of droplet centers:	$235.9 \mu\text{m}$
Droplet diameter:	$235.9 \mu\text{m}$
Relative velocity:	7.74 m/s
Disperse phase:	$\eta_l = 2.39 \cdot 10^{-3} \text{ Pa s}, \rho_f = 784.5 \text{ kg/m}^3$
Continuous Phase:	$\eta_g = 0.0182 \cdot 10^{-3} \text{ Pa s}, \rho_g = 1.19 \text{ kg/m}^3$
Surface tension:	$21.4 \cdot 10^{-3} \text{ N/m}$

Table C.3.: Setups for the simulations of the case $We = 518$; Chapter 4.1.

Domain size:	$750 \times 750 \times 250 \mu\text{m}$
Grid:	$384 \times 384 \times 128$
Number of the employed symmetry planes:	3
Initial distance of droplet centers:	$235.9 \mu\text{m}$
Droplet diameter:	$235.9 \mu\text{m}$
Relative velocity:	7.2 m/s
Disperse phase:	$\eta_l = 2.39 \cdot 10^{-3} \text{ Pa s}, \rho_f = 784.5 \text{ kg/m}^3$
Continuous Phase:	$\eta_g = 0.0182 \cdot 10^{-3} \text{ Pa s}, \rho_g = 1.19 \text{ kg/m}^3$
Surface tension:	$21.4 \cdot 10^{-3} \text{ N/m}$

Table C.4.: Setup for the simulation of the case $We = 448$; Chapter 4.1.

Domain size:	$720 \times 720 \times 720 \mu\text{m}$
Grid:	$144 \times 144 \times 48$
Number of the employed symmetry planes:	3
Initial distance of droplet centers:	$231.6 \mu\text{m}$
Droplet diameter:	$231.6 \mu\text{m}$
Relative velocity:	7.0 m/s
Disperse phase:	$\eta_l = 2.39 \cdot 10^{-3} \text{ Pa s}, \rho_f = 784.5 \text{ kg/m}^3$
Continuous Phase:	$\eta_g = 0.0182 \cdot 10^{-3} \text{ Pa s}, \rho_g = 1.19 \text{ kg/m}^3$
Surface tension:	$21.4 \cdot 10^{-3} \text{ N/m}$

Table C.5.: Setup for the simulation of a droplet collision process for illustrating the correction of the surface energy computation; Chapter 4.1.

Domain size:	$670.4 \times 670.4 \times 670.4 \mu\text{m}$
Grid M1:	$64 \times 64 \times 64$
M2:	$128 \times 128 \times 128$
M3:	$256 \times 256 \times 256$
Number of the employed symmetry planes:	3
Initial distance of droplet centers:	$789.162 \mu\text{m}$
Droplet diameter:	$335.2 \mu\text{m}$
Relative velocity:	0.992 m/s
Disperse phase:	$\eta_l = 2.2 \cdot 10^{-3} \text{ Pa s}, \rho_f = 730 \text{ kg/m}^3$
Continuous Phase:	$\eta_g = 0.0198 \cdot 10^{-3} \text{ Pa s}, \rho_g = 1 \text{ kg/m}^3$
Surface tension:	$27 \cdot 10^{-3} \text{ N/m}$

Table C.6.: Setups for the simulations of bouncing; Chapter 4.2.

Domain size:	$678.8 \times 678.8 \times 678.8 \mu\text{m}$
Grid M1:	$64 \times 64 \times 64$
M2:	$128 \times 128 \times 128$
M3:	$256 \times 256 \times 256$
Number of the employed symmetry planes:	3
Initial distance of droplet centers:	$471.072.581 \mu\text{m}$
Droplet diameter:	$339.4 \mu\text{m}$
Relative velocity:	1.192 m/s
Coalescence instant:	0.368 ms
Disperse phase:	$\eta_l = 2.2 \cdot 10^{-3} \text{ Pa s}, \rho_f = 730 \text{ kg/m}^3$
Continuous Phase:	$\eta_g = 0.0198 \cdot 10^{-3} \text{ Pa s}, \rho_g = 1 \text{ kg/m}^3$
Surface tension:	$27 \cdot 10^{-3} \text{ N/m}$

Table C.7.: Setups for the simulations of coalescence; Chapter 4.2.

Domain size:	$500 \times 500 \mu\text{m}$
Grid :	2048×2048
Number of the employed symmetry planes:	2
Initial distance of droplet centers:	$300 \mu\text{m}$
Droplet diameter:	$300 \mu\text{m}$
Relative velocity:	1.0 m/s
Disperse phase:	$\eta_l = 2.2 \cdot 10^{-3} \text{ Pa s}, \rho_f = 730 \text{ kg/m}^3$
Continuous Phase:	$\eta_g = 0.22 \cdot 10^{-3} \text{ Pa s}, \rho_g = 73 \text{ kg/m}^3$
Surface tension:	$27 \cdot 10^{-3} \text{ N/m}$

Table C.8.: Setup for the 2D simulation; Chapter 6.

Domain size:	$670.4 \times 670.4 \times 670.4 \mu\text{m}$
Grid M1:	$128 \times 128 \times 128$
M2:	$256 \times 256 \times 256$
Number of the employed symmetry planes:	3
Initial distance of droplet centers:	$400 \mu\text{m}$
Droplet diameter:	$335.2 \mu\text{m}$
Relative velocity:	0.992 m/s
Disperse phase:	$\eta_l = 2.2 \cdot 10^{-3} \text{ Pa s}, \rho_f = 730 \text{ kg/m}^3$
Continuous Phase:	$\eta_g = 1.98 \cdot 10^{-3} \text{ Pa s}, \rho_g = 100 \text{ kg/m}^3$
Surface tension:	$27 \cdot 10^{-3} \text{ N/m}$

Table C.9.: Setups for the validation of the integration of the SGS model with the main solver FS3D; Chapter 7.4.

Domain size:	$678.8 \times 678.8 \times 678.8 \mu\text{m}$
Grid M1:	$96 \times 96 \times 96$
M2:	$128 \times 128 \times 128$
M3:	$192 \times 192 \times 192$
M4:	$256 \times 256 \times 256$
Number of the employed symmetry planes:	3
Initial distance of droplet centers:	$471.072.581 \mu\text{m}$
Droplet diameter:	$339.4 \mu\text{m}$
Relative velocity:	$0.9, 1.0, 1.1, 1.192, 1.3, 1.4 \text{ m/s}$
Disperse phase:	$\eta_l = 2.3 \cdot 10^{-3} \text{ Pa s}, \rho_f = 763 \text{ kg/m}^3$
Continuous Phase:	$\eta_g = 0.0198 \cdot 10^{-3} \text{ Pa s}, \rho_g = 1 \text{ kg/m}^3$
Surface tension:	$27 \cdot 10^{-3} \text{ N/m}$
Mean free path:	68 nm

Table C.10.: Setups for the simulations aiming at the prediction of the collision outcomes; Chapter 7.5.

Bibliography

- [1] AGBAGLAH, G. and R. D. DEEGAN: *Growth and instability of the liquid rim in the crown splash regime*. Journal of Fluid Mechanics, 752:485–496, 2014.
- [2] ALBERT, C.: *On stability of falling films: numerical and analytical investigations*. PhD thesis, Technische Universität Darmstadt, 2013.
- [3] ALLEN, R. F.: *The role of surface tension in splashing*. Journal of Colloid and Interface Science, 51(2):350–351, 1975.
- [4] ASHGRIZ, N.: *Handbook of Atomization and Sprays: Theory and Applications*. Springer, New York et al., 2011.
- [5] ASHGRIZ, N. and J. Y. POO: *Coalescence and separation in binary collisions of liquid drops*. Journal of Fluid Mechanics, 221:183–204, 1990.
- [6] BELLMAN, R. and R. H. PENNINGTON: *Effects of surface tension and viscosity on Taylor instability*. Quarterly of Applied Mathematics, 12:151–162, 1954.
- [7] BLAZEK, J.: *Computational Fluid Dynamics: Principles and Applications*. Elsevier Science, Oxford, 2005.
- [8] BOGER, M., J. SCHLOTTKE, C.-D. MUNZ and B. WEIGAND: *Reduction of parasitic currents in the DNS VOF code FS3D*. In *12th Workshop on Two-Phase Flow Predictions*, Halle (Saale), Germany, 2010.
- [9] BOTHE, D.: *Mathematische Modellierung ein- und mehrphasiger Strömungen*. Lecture notes. Technische Universität Darmstadt, 2009.
- [10] BRACKBILL, J. U., D. KOTHE and C. ZEMACH: *A continuum method for modeling surface tension*. Journal of Computational Physics, 100(2):335–354, 1992.
- [11] BRENN, G. and A. FROHN: *Collision and coalescence of droplets of various liquids*. Journal of Aerosol Science, 20(8):1027–1030, 1989.
- [12] CHANDRASEKHAR, S.: *Hydrodynamic and Hydromagnetic Stability*. Dover Publications, Oxford, 1961.
- [13] COSSALI, G. E., A. COGHE and M. MARENGO: *The impact of a single drop on a wetted solid surface*. Experiments in Fluids, 22(6):463–472, 1997.
- [14] DONGARI, N., A. AGRAWAL and A. AGRAWAL: *Analytical solution of gaseous slip flow in long microchannels*. International Journal of Heat and Mass Transfer, 50(17):3411–3421, 2007.

-
- [15] ESTRADE, J. P., H. CARENTZ, G. LAVERGNE and Y. BISCOS: *Experimental investigation of dynamic binary collision of ethanol droplets—a model for droplet coalescence and bouncing*. International Journal of Heat and Fluid Flow, 20(5):486–491, 1999.
- [16] FOCKE, C.: *Direkte numerische Simulation binärer Kollisionen newtonscher und nichtnewtonscher Tropfen*. PhD thesis, Technische Universität Darmstadt, 2013.
- [17] FOCKE, C. and D. BOTHE: *Computational analysis of binary collisions of shear-thinning droplets*. Journal of Non-Newtonian Fluid Mechanics, 166(14):799–810, 2011.
- [18] FOCKE, C. and D. BOTHE: *Direct numerical simulation of binary off-center collisions of shear thinning droplets at high Weber numbers*. Physics of Fluids, 24(7):073105, 2012.
- [19] FOCKE, C., M. KUSCHEL, M. SOMMERFELD and D. BOTHE: *Collision between high and low viscosity droplets: Direct Numerical Simulations and experiments*. International Journal of Multiphase Flow, 56:81–92, 2013.
- [20] FRANCOIS, M. M., S. J. CUMMINS, E. D. DENDY, D. B. KOTHE, J. M. SICILIAN and M. W. WILLIAMS: *A balanced-force algorithm for continuous and sharp interfacial surface tension models within a volume tracking framework*. Journal of Computational Physics, 213(1):141–173, 2006.
- [21] GUNN, R.: *Collision characteristics of freely falling water drops*. Science, 150(3697):695–701, 1965.
- [22] HAMROCK, B. J., S. R. SCHMID and B. O. JACOBSON: *Fundamentals of Fluid Film Lubrication*. Marcel Dekker, Inc., New York, 2004.
- [23] HIRT, C. W. and B. D. NICHOLS: *Volume of fluid (VOF) method for the dynamics of free boundaries*. Journal of Computational Physics, 39(1):201–225, 1981.
- [24] JIANG, X. and A. J. JAMES: *Numerical simulation of the head-on collision of two equal-sized drops with van der Waals forces*. Journal of Engineering Mathematics, 59(1):99–121, 2007.
- [25] JIANG, Y. J., A. UMEMURA and C. K. LAW: *An experimental investigation on the collision behaviour of hydrocarbon droplets*. Journal of Fluid Mechanics, 234:171–190, 1992.
- [26] KIM, H.-Y., Z. C. FENG and J.-H. CHUN: *Instability of a liquid jet emerging from a droplet upon collision with a solid surface*. Physics of Fluids, 12(3):531–541, 2000.
- [27] KUAN, C. K., K. L. PAN and W. SHYY: *Study on high-Weber-number droplet collision by a parallel, adaptive interface-tracking method*. Journal of Fluid Mechanics, 759:104–133, 2014.
- [28] LAFAURIE, B., C. NARDONE, R. SCARDOVELLI, S. ZALESKI and G. ZANETTI: *Modelling merging and fragmentation in multiphase flows with SURFER*. Journal of Computational Physics, 113(1):134–147, 1994.

-
- [29] LEVIN, Z. and P. V. HOBBS: *Splashing of water drops on solid and wetted surfaces: hydrodynamics and charge separation*. Philosophical Transactions for the Royal Society of London. Series A, Mathematical and Physical Sciences, 269:555–585, 1971.
- [30] LIU, M. and D. BOTHE: *Numerical study of head-on droplet collisions at high Weber numbers*. Journal of Fluid Mechanics, 789:785–805, 2016.
- [31] LIU, M., M. REITZLE, G. KARCH, S. BOBLEST, B. WEIGAND, K. SCHULTE and D. BOTHE: *High resolution computation of head-on droplet collisions at high Weber numbers*. Preparing for publication.
- [32] MACKAY, G. D. M. and S. G. MASON: *The gravity approach and coalescence of fluid drops at liquid interfaces*. The Canadian Journal of Chemical Engineering, 41(5):203–212, 1963.
- [33] MASON, L. R., G. W. STEVENS and D. J. E. HARVIE: *Multiscale volume of fluid modelling of droplet coalescence*. In *Ninth International Conference on Computational Fluid Dynamics in the Minerals and Process Industries*, Melbourne, Australia, 2012.
- [34] MEHDIZADEH, N. Z., S. CHANDRA and J. MOSTAGHIMI: *Formation of fingers around the edges of a drop hitting a metal plate with high velocity*. Journal of Fluid Mechanics, 510:353–373, 2004.
- [35] MURAD, S. and C. K. LAW: *Molecular simulation of droplet collision in the presence of ambient gas*. Molecular Physics, 96(1):81–85, 1999.
- [36] NIKOLOPOULOS, N., K. S. NIKAS and G. BERGELES: *A numerical investigation of central binary collision of droplets*. Computers & Fluids, 38(6):1191–1202, 2009.
- [37] NIKOLOPOULOS, N., A. THEODORAKAKOS and G. BERGELES: *Off-centre binary collision of droplets: A numerical investigation*. International Journal of Heat and Mass Transfer, 52(19):4160–4174, 2009.
- [38] NOBARI, M. R. H. and G. TRYGGVASON: *Numerical simulations of three-dimensional drop collisions*. AIAA Journal, 34(4):750–755, 1996.
- [39] PAN, K. L., P. C. CHOU and Y. J. TSENG: *Binary droplet collision at high Weber number*. Physical Review E, 80(3):036301, 2009.
- [40] PAN, K. L., C. K. LAW and B. ZHOU: *Experimental and mechanistic description of merging and bouncing in head-on binary droplet collision*. Journal of Applied Physics, 103(6):064901, 2008.
- [41] PAN, Y. and K. SUGA: *Numerical simulation of binary liquid droplet collision*. Physics of Fluids, 17(8):082105, 2005.
- [42] PLANCHETTE, C., H. HINTERBICHLER, M. LIU, D. BOTHE and G. BRENN: *Colliding drops as coalescing and fragmenting liquid springs*. Journal of Fluid Mechanics, 814:277–300, 2017.

-
- [43] POPINET, S.: *An accurate adaptive solver for surface-tension-driven interfacial flows*. Journal of Computational Physics, 228(16):5838–5866, 2009.
- [44] PROSPERETTI, A. and G. TRYGGVASON: *Computational Methods for Multiphase Flow*. Cambridge university press, New York, 2009.
- [45] QIAN, J. and C. K. LAW: *Regimes of coalescence and separation in droplet collision*. Journal of Fluid Mechanics, 331:59–80, 1997.
- [46] RAYLEIGH, LORD: *On the instability of jets*. Proceedings of the London Mathematical Society, 10:4–13, 1878.
- [47] RAYLEIGH, LORD: *On the Capillary Phenomena of Jets*. Proceedings of the Royal Society of London, 29:71–97, 1879.
- [48] RAYLEIGH, LORD: *The Theory of Sound*, volume 2. Macmillan and CO., London, 1896.
- [49] RENARDY, Y. and M. RENARDY: *PROST: a parabolic reconstruction of surface tension for the volume-of-fluid method*. Journal of Computational Physics, 183(2):400–421, 2002.
- [50] RIDER, W. J. and D. B. KOTHE: *Reconstructing volume tracking*. Journal of Computational Physics, 141(2):112–152, 1998.
- [51] RIEBER, M.: *Numerische Modellierung der Dynamik freier Grenzflächen in Zweiphasenströmungen*. PhD thesis, University of Stuttgart, 2004.
- [52] RIEBER, M. and A. FROHN: *Navier-Stokes simulation of droplet collision dynamics*. In *Proc. 7th Int. Symp. On Comp. Fluid Dynamics*, pages 520–525, Beijing, China, 1997.
- [53] RIEBER, M. and A. FROHN: *A numerical study on the mechanism of splashing*. International Journal of Heat and Fluid Flow, 20(5):455–461, 1999.
- [54] ROISMAN, I. V., K. HORVAT and C. TROPEA: *Spray impact: rim transverse instability initiating fingering and splash, and description of a secondary spray*. Physics of Fluids, 18(10):102104, 2006.
- [55] ROTH, N., C. MERCADÉ, H. GOMAA, C. FOCKE, D. BOTHE, I. V. ROISMAN and B. WEIGAND: *Collision of droplets: experimental, analytical and numerical approach*. In *25th European Conference on Liquid Atomization and Spray Systems*, Chania, Crete, 2013.
- [56] ROTH, N., M. RIEBER and A. FROHN: *High energy head-on collision of droplets*. In *15th Annual Conference on Liquid Atomization and Spray Systems*, Toulouse, France, 1999.
- [57] SAROKA, M. D., N. ASHGRIZ and M. MOVASSAT: *Numerical investigation of head-on binary drop collisions in a dynamically inert environment*. Journal of Applied Fluid Mechanics, 5(1):23–37, 2012.
- [58] SCHÄFER, M.: *Computational Engineering: Introduction to Numerical Methods*. Springer, Berlin et al., 2006.

-
- [59] SCHONBERG, R. H. DAVIS and J. A. and J. M. RALLISON: *The lubrication force between two viscous drops*. *Physics of Fluids A*, 1(1), 1989.
- [60] SHEN, C.: *Rarefied Gas Dynamics: Fundamentals, Simulations and Micro Flows*. Springer, Berlin et al., 2005.
- [61] SHUKLA, J. B., S. KUMAR and P. CHANDRA: *Generalized Reynolds equation with slip at bearing surfaces: multiple-layer lubrication theory*. *Wear*, 60(2):253–268, 1980.
- [62] SOMMERFELD, M. and M. KUSCHEL: *Modelling droplet collision outcomes for different substances and viscosities*. *Experiments in Fluids*, 57(12):187, 2016.
- [63] TAYLOR, G.: *The instability of liquid surfaces when accelerated in a direction perpendicular to their planes. I*. *Proceedings of the Royal Society of London. Series A. Mathematical and Physical Sciences*, 201(1065):192–196, 1950.
- [64] THORODDSEN, S. T. and J. SAKAKIBARA: *Evolution of the fingering pattern of an impacting drop*. *Physics of Fluids*, 10(6):1359–1374, 1998.
- [65] TSIEN, H. S.: *Superaerodynamics, mechanics of rarefied gases*. *Journal of Aerosol Science*, 13:653–664, 1946.
- [66] VASSALLO, P. and N. ASHGRIZ: *Satellite formation and merging in liquid jet breakup*. *Proceedings of the Royal Society of London A: Mathematical, Physical and Engineering Sciences*, 433(1888):269–286, 1991.
- [67] WANG, X. G., Z. H. HUANG, O. A. KUTI, W. ZHANG and K. NISHIDA: *Experimental and analytical study on biodiesel and diesel spray characteristics under ultra-high injection pressure*. *International Journal of Heat and Fluid Flow*, 31(4):659–666, 2010.
- [68] WEBER, C.: *On the breakdown of a fluid jet, Zum Zerfall eines Flüssigkeitsstrahles*. *Zeitschrift für angewandte Mathematik und Physik*, 48:136–154, 1931.
- [69] WÖRNER, M., W. SABISCH, G. GRÖTZBACH and D. G. CACUCI: *Volume-averaged conservation equations for volume-of-fluid interface tracking*. In *Proceedings of the 4th International Conference on Multiphase Flow*, New Orleans, Louisiana, USA, 2001.
- [70] ZHANG, L. V., P. BRUNET, J. EGGERS and R. D. DEEGAN: *Wavelength selection in the crown splash*. *Physics of Fluids*, 22(12):122105, 2010.
- [71] ZHANG, P. and C. K. LAW: *An analysis of head-on droplet collision with large deformation in gaseous medium*. *Physics of Fluids*, 23(4):042102, 2011.

Curriculum Vitae

Personal information

Name	Muyuan Liu
Date of Birth	09. Aug. 1984
Place of Birth	Hebei, China

Education

Mar. 2014 - Oct. 2017	Doctoral study at Chair of Mathematical Modeling and Analysis. Technische Universität Darmstadt, Germany.
Oct. 2009 - Jun 2013	Master of Science. Mechanical and Process Engineering. Technische Universität Darmstadt, Germany.
Sept. 2004 - July 2008	Bachelor of Engineering. Automobile Engineering. University of Jilin, China.

Employment

July 2013 - Dec. 2017	Research assistant at institute of Mathematical Modeling and Analysis. Technische Universität Darmstadt, Germany
-----------------------	---
